T.R.
GEBZE TECHNICAL UNIVERSITY
GRADUATE SCHOOL

WINDAGE HEATING IN A SHROUDED ROTOR-STATOR CAVITIES

ONUR GARİP

A THESIS OF MASTER OF SCIENCE
DEPARTMENT OF ENERGY TECHNOLOGIES
IN APPLIED PROPULSION SYSTEM DESIGN & ENGINEERING
FOR AEROSPACE TECHNOLOGIES PROGRAM

ADVISOR: DR. ERİNÇ ERDEM

MARCH 2024

T.R.
GEBZE TECHNICAL UNIVERSITY
GRADUATE SCHOOL

WINDAGE HEATING IN A SHROUDED ROTOR-STATOR CAVITIES

ONUR GARİP

A THESIS OF MASTER OF SCIENCE
DEPARTMENT OF ENERGY TECHNOLOGIES
IN APPLIED PROPULSION SYSTEM DESIGN &
ENGINEERING FOR AEROSPACE
TECHNOLOGIES PROGRAM

ADVISOR: DR. ERİNÇ ERDEM

MARCH 2024

T.C.
GEBZE TEKNİK ÜNİVERSİTESİ
LİSANSÜSTÜ EĞİTİM ENSTİTÜSÜ

DÖNEN VE DÖNMEYEN YÜZEYE SAHİP ÖRTÜLÜ BOŞLUKLARDA AKIŞKANIN RÜZGÂR ETKİSİ İLE ISINMASI

ONUR GARİP

YÜKSEK LİSANS TEZİ
ENERJİ TEKNOLOJİLERİ ANABİLİM DALI
HAVACILIK VE UZAY TEKNOLOJİLERİNDE UYGULAMALI İTKİ SİSTEMİ TASARIM MÜHENDİSLİĞİ PROGRAMI

DANIŞMAN: DR. ERİNÇ ERDEM

MART 2024

MASTER of SCIENCE JURY APPROVAL FORM

A thesis submitted by Onur GARIP, defended on 05/03/2024 before the jury formed with the 12/02/2024 date and 2024/13 numbered decision of the GTU Graduate Administration Board, has been accepted as a MASTER of SCIENCE thesis in the Department of Energy Technologies, Applied Propulsion System Design Engineering for Aerospace Technologies Program.

JURY

MEMBER
(THESIS ADVISOR) : Dr. Erinç ERDEM

MEMBER : Prof. Dr. Yahya DOĞU

MEMBER : Prof. Dr. İlyas KANDEMİR

APPROVAL

Gebze Technical University Graduate Administration Board
/ / date and / numbered decision.

SIGNATURE/SEAL

ABSTRACT

Windage heating is a phenomenon normally associated with all systems rotating in a fluid medium but in the case of gas turbine, it can be found in the side cavities between rotating and the stationary parts in nearly all kinds of compressor and turbines. The flow conditions and the surface roughness of the disks have an impact on the windage loss, which in turn affects the cooling effectiveness of the air and eventually the overall efficiency of the engine. In order to better understand the windage heating in a rotor-stator cavities, theoretical, numerical and experimental studies are performed in this thesis.

In chapter 1, the functions of secondary air systems (SAS) and the responsibilities of SAS designers are first introduced for the interested reader and as a broader description of the specific area of interest addressed in this thesis. Then, the importance of windage heating in gas turbines and the significance of this thesis are briefly explained.

Chapter 2 summarizes the theoretical knowledge gathered as a result of long and detailed research, without overwhelming the reader with too many derivations but rather aiming to explain the logic and the basis of the theory together with the results that have been accepted by many authorities and the accuracy of which has been evaluated by many tests. While covering the topics from the basis of rotating flows such as “free disk” and boundary layer to complex cavity flows, I have generated equations and results that are absent in the literature. In addition, all the theory learned in this chapter applied to our test rig case and necessary calculations repeated and given accordingly in the related parts.

In chapter 3, 1D cavity solver “SOCS design tool” developed using C-sharp and Microsoft Visual Studio was introduced. This tool solving swirl and windage distributions throughout the cavity in seconds and it’s accuracy has been questioned throughout the following parts but in this part one test case example was made for the accuracy of the approach itself.

In chapter 4, the setup of the numerical simulation is illustrated. In order to minimize the error, the selection of a turbulence model and the generation of the mesh are accomplished by benchmark and mesh independence studies respectively. The simulation results are validated by more than one test data representing both high and low windage levels, indicating that the set-up is reasonable. More importantly, comparison studies between simulations and 1D cavity solver reveals how advantageous “SOCS design tool” in terms of accuracy and computational cost. Moreover, roughness studies also performed within CFD using Schlichting model which generating reasonable results when comparing with those from the literature.

In chapter 5, the design of the test rig is presented together with its instrumentation and hardware selection for both the windage and disk pumping tests. The uncertainties of the experimental parameters are also estimated and briefly discussed.

All provide a comprehensive knowledge not only about windage heating but also from the basis of the flow around rotating disks to complex cavity flows in a shrouded rotor-stator cavities.

Keywords: Windage Heating, Windage Loss, Computational Fluid Dynamics (CFD), Rotor-Stator Cavity, Test Rig Design, Secondary Air Systems

ÖZET

Rüzgarlama etkisi (windage) ile ısınma, normalde akışkan bir ortamda dönen (disk, şaft) tüm sistemlerle ilişkili bir olgudur; ancak gaz türbini söz konusu olduğunda, neredeyse her tür kompresör ve türbinde dönen ve sabit parçalar arasındaki yan boşluklarda karşılaşılan bir fenomendir. Akış koşulları ve disklerin yüzey pürüzlülüğü bu kayıp üzerinde bir etkiye sahiptir ve bu da havanın soğutma etkinliğini ve nihayetinde motorun genel verimliliğini etkiler. Bu tezde, dönen ve dönmeyen yüzeylere sahip boşluklarda havanın rüzgarlama etkisi ile ısınmasını daha iyi anlamak için teorik, sayısal ve deneysel çalışmalar yapılmıştır.

Bölüm 1'de, ilk olarak ikincil hava sistemlerinin (SAS) işlevleri ve SAS tasarımcılarının sorumlulukları, ilgili okuyucular için ve bu tezde ele alınan özel ilgi alanının daha geniş bir açıklaması olarak tanıtılmaktadır. Ardından, gaz türbinlerinde rüzgarlama etkisinin önemi ve bu tezin önemi kısaca açıklanmıştır.

Bölüm 2'de, uzun ve detaylı araştırmalar sonucunda elde edilen teorik bilgiler, denklemlerin türetilmesinden ziyade teorinin mantığını ve temelini, birçok otorite tarafından kabul edilmiş ve doğruluğu birçok testle değerlendirilmiş sonuçlarıyla birlikte açıklamayı amaçlayarak özetlenmiştir. "Serbest disk" ve sınır tabaka gibi dönen akışların temelinden boşluklarda görülen karmaşık akışlara kadar konuları ele alırken literatürde olmayan denklemler ve sonuçlar ortaya koyulmuştur. Ayrıca, bu bölümde öğrenilen tüm teori test düzeneğinde sahip olduğumuz sistem için de uygulanmış ve gerekli hesaplamalar ilgili bölümlerde tekrarlanarak verilmiştir.

Bölüm 3'te, C-sharp ve Microsoft Visual Studio kullanılarak geliştirilen 1 Boyutlu boşluk çözücü "SOCS tasarım aracı" tanıtılmıştır. Boşluk boyunca görülen girdap oranı ve kayıp dağılımlarını saniyeler içinde çözen bu aracın doğruluğu ilerleyen bölümlerde sorgulanmıştır ancak bu bölümde yaklaşımda yapılan varsayımın doğruluğu için bir test vakası örneği yapılmıştır.

Bölüm 4'te sayısal simülasyonun kurulumu gösterilmektedir. Hatayı en aza indirmek için türbülans modelinin seçimi ve ağın oluşturulması sırasıyla kıyaslama ve ağ bağımsızlığı çalışmaları ile gerçekleştirilmiştir. Simülasyon sonuçları, hem yüksek hem de düşük rüzgar seviyelerini temsil eden birden fazla test verisi ile doğrulanmıştır ve bu da kurulumun makul olduğunu göstermektedir. Daha da önemlisi, simülasyonlar ve 1 Boyutlu boşluk çözücü arasındaki karşılaştırma çalışmaları, "SOCS tasarım aracının" doğruluk ve hesaplama maliyeti açısından ne kadar avantajlı olduğunu ortaya koymaktadır. Ayrıca, pürüzlülük çalışmaları da literatüre kıyasla makul sonuçlar üreten Schlichting modeli kullanılarak CFD içinde gerçekleştirilmiştir.

Bölüm 5'te, test teçhizatının tasarımı, enstrümantasyon ve donanım seçimi ile birlikte hem rüzgarlama hem de diskin sürüklediği hava miktarı testleri için sunulmuştur. Deneysel parametrelerin belirsizlikleri de tahmin edilmiş ve kısaca tartışılmıştır.

Tüm bunlar sadece rüzgarlama etkisi ile ısınma hakkında değil, aynı zamanda dönen disklerin etrafındaki akış temelinden örtülü rotor-stator boşluklarındaki karmaşık boşluk akışlarına kadar kapsamlı bir bilgi sağlamaktadır.

Anahtar Kelimeler: Rüzgarlama Etkisi ile Isınma, Rüzgarlama Etkisi Kaybı, Hesaplamalı Akışkanlar Dinamiği (HAD), Dönen ve Dönmeyen Yüzeyli Boşluklar, Test Donanımı Tasarımı, İkincil Hava Sistemleri

ACKNOWLEDGEMENTS

This dissertation and Master’s degree has been the most challenging but also the most rewarding part of my career. A contribution of this magnitude would not have been possible without the perpetual love and support of my family and loved ones to whom I shall forever remain indebted.

Among all my teaching fellows through program and my distinguished colleagues at TEI, three individuals stand out: Mr. Erinç Erdem, Mr. Orçun Kor and Mr. Sefa Yılmaz. They are my true professional heroes.

My sincere gratitude goes first to my supervisor Mr. Erinç Erdem for his inspiring discussions, constant guidance and encouragement throughout this work. I would also like to thank him for his mentoring and trainings not only through this thesis but also throughout my career in TEI.

I would also like to thank to Mr. Orçun Kor for his profound belief in my work and in me. I would also like to express my gratitude for his contributions to my personal and professional growth over many years by now. Without his leadership, none of the test campaign of this study would have been possible.

I owe many thanks to my friend and my former colleague Mr. Sefa Yılmaz for helping me on developing cavity solver tool explained in chapter 3.

Last but not least, my gratitude also extends to my company TEI who provides the funds to built-up the test rig and experimental facilities.

TABLE OF CONTENTS

LIST OF SYMBOLS AND ABBREVIATIONS

Ra_{adm} : Admissible average roughness height
$k_{s,adm}$: Admissible equivalent roughness height
θ : Angle in cylindrical coordinates
ω : Angular velocity of the disk
A : Area
R_a : Arithmetic average roughness height
$\bar{\rho}$: Average density
z : Axial coordinate
s : Axial gap of the cavity
Re_l : Axial Reynolds number
V_z : Axial velocity
f_θ : Body forces per unit mass in the tangential direction
$\vec{f}$: Body forces per unit mass vector
C : Constant for equivalent roughness height
C_s : Constant for viscous sublayer thickness
$C(n)$: Constants for n-th power velocity law
S_{f_0} : Core rotation swirl with zero throughflow
ζ : Correction factor to “free disk” case
ρ : Density
Δ : Difference operator
$\dot{m}_0$: Disk pumping mass flow rate
μ : Dynamic viscosity
k_s : Equivalent roughness height
α : Fluid slip angle reference to tangential direction
F : Force
F_θ : Force per unit volume in the tangential direction
u^* : Friction velocity
G : Gap ratio
γ : Heat capacity ratio
$\vec{q}$: Heat flux vector
ds : Infinitesimal change in arc length
dr : Infinitesimal change in radial direction
ν : Kinematic viscosity
C_{qr} : Local flow rate coefficient
Re_h : Local horizontal Reynolds number
$Re_{\theta_{local}}$: Local rotational Reynolds number
$\dot{m}$: Mass flow rate
Re'_θ : Modified rotational Reynolds number
C_m : Moment Coefficient
C_{m_1} : Moment coefficient for regime I
C_{m_2} : Moment coefficient for regime II
C_{m_3} : Moment coefficient for regime III
C_{m_4} : Moment coefficient for regime IV
ξ : Non-dimensional axial distance from the disk
x : Non-dimensional radial coordinate ($x = r/R$)

C_w : Non-dimensional superposed flow rate
u^+ : Non-dimensional velocity
y^+ : Non-dimensional wall distance
∇ : Operator Nabla
R : Outer radius of the disk
R_i, r_i : Partial radius of the disk
γ : Power law coefficients
ε_m : Power law coefficients
ε_M : Power law coefficients
r : Radial coordinate
V_r : Radial velocity
r_c : Radius at which core rotation starts for radial inlet
Φ : Rate of viscous dissipation per unit volume
$\overrightarrow{W}$: Relative velocity vector
R_{rms},R_q : RMS roughness height
Re_θ : Rotational Reynolds number
$\overleftrightarrow{\tau}$: Shear stress tensor
C_f : Skin friction coefficient
h_0 : Specific stagnation enthalpy
p, P, P_s : Static Pressure
l : Streamwise coordinate
S_f : Swirl ratio or swirl factor
τ_θ : Tangential component of the shear stress
V_θ : Tangential velocity
R_z : Ten-point roughness height
δ : Thickness of the boundary later
C_{adm} : Threshold constant for admissible roughness
M : Torque or moment
Γ : Torque or moment
Γ'_θ : Torque per unit volume in the tangential direction
T_t : Total temperature
λ_t : Turbulent flow parameter
U_∞ : Velocity of free stream
Q : Volumetric through-flow rate
τ_w : Wall shear stress
$\dot{W}_{windage}$: Windage power
CFD : Computational fluid dynamics
LDA : Laser Doppler Anemometer
OEM : Original Equipment Manufacturer
OPR : Overall Pressure Ratio
rpm : Revolution per minute
RSM : Reynolds Stress Model
SAS : Secondary Air Systems
SR-4 : Simmons Ruge-4
TEI : TUSAŞ Engine Industries, Inc.

LIST OF FIGURES

LIST OF TABLES

1. INTRODUCTION

Since the development of gas turbine engines at beginning of 40's, they have advanced significantly and have become the most compact power sources available today. During this progress, turbine-inlet temperatures have risen from around 1000 K to over 2000 K on engineering race to create the most efficient engine which industry demands in order to produce more power at lower cost. Since this temperature levels are over the melting point of any structural material in contact, most of the increase has been made possible by cooling technologies while some has occurred through the development of materials and metallurgy. As the turbine inlet temperatures have increased, so have the compression ratios; which resulted in elevated temperatures of the air used for cooling. In fact, the temperature of air leaving the compressor of modern engine is higher than the turbine-inlet temperatures of the earliest engines during Whittle era!

Today especially modern commercial turbofan engines pushing further their limits in terms of thermal efficiencies to make smaller cores, which meaning higher by-pass ratio engines with higher propulsive, so that overall, efficiencies. Since high thermal efficiencies requires not only high OPR and turbine inlet temperatures but also high component efficiencies and low secondary system losses, today, sealing and cooling technologies in demand as never before.

1.1. Secondary Air Systems in Gas Turbine Engines

In gas turbine engines, to increase cycle efficiency it is of paramount importance to increase compressor pressure ratio and turbine inlet temperature. Higher increase pressure ratios require efficient compression technologies whereas higher turbine inlet temperatures demand better cooling technologies coupled with advanced materials. Modern gas turbine engines work at elevated temperatures that are above the material limits; hence, the cooling of turbine components is vital.

Another pertinent aspect is the leakage of main flow path gases into the cavities formed by static and rotating components, which consequently reduced module efficiencies leading to diminished cycle efficiencies. To provide necessary sealing to various engine components sealing airflow is metered via dynamic sealing elements and routed to those cavities. In addition cooling of bearings and the chambers around them is accomplished with spraying/feeding oil onto relevant surfaces. Pressurization air is utilized to seal the bearing chambers preventing oil leakage that might lead to oil fire.

The axial load of a gas turbine engine is the resultant of the aerodynamics loads coupled with pressure loads occurring rotor-stator and rotor-rotor cavities, exerted on rotating surfaces. Ball bearings situated inside bearing chambers carry axial load, and the resultant load naturally needs to lie below the capacity of the bearings. Excessive loading of ball bearings would result in overheating leading to reduction in service life. Therefore, control and the management of axial loads is crucial for reliable operation.

In essence, the functions of Secondary Air Systems (SAS) can be summarized as follow:

- Cooling of turbine components
- Sealing of cavities and bearing chambers
- Management of axial loads
- Providing bleed airs to assist compressor stability, for customer needs and anti-icing systems.

In order to accomplish these functions, SAS flows are taken out from compressor offtakes and routed to relevant components via restrictive elements. These airflows essentially bypass the combustion chamber and consequently partially contribute to the power/thrust generation detrimental to engine performance. Therefore, minimization of SAS flows is key.

SAS is responsible for all the flows outside the main gas path and inherently interacting significantly with the parts that are securing and fixing the aerodynamic components. Thus, SAS designers work closely with mechanical and thermal designers. Throughout the design process, boundary conditions taken from aerodynamic designers and then the flows are calculated using regulative and metering elements such as holes, tubes, orifices, cavities (rotor-stator and/or rotor-rotor), etc. While routing the required airflows to respective components, associated pressure drop and temperature rise owing to either heat transfer or windage heating are taken into account. After the completion of functions, SAS flows are either injected back into main gas path or discharged overboard.

While carrying out its functions, SAS needs to incorporate robust design philosophy, which assures insensitivity of airflows to the changes happening throughout the operating envelope, leading to reliable operation. These changes imply the alterations in gaps and clearances between parts alter and variations of main gas path pressures and temperatures. Moreover, manufacturing tolerances impose variations to the geometries of critical restrictive elements. Generally, these alterations results in changes to airflow rates proportional to engine air flow rate. Another important aspect is the capability of SAS to respond to increase thrust/power levels, as known as growth potential. To achieve this potential overdesigning of restrictive elements and/or having the ability to apply small modifications to critical components with ease are required.

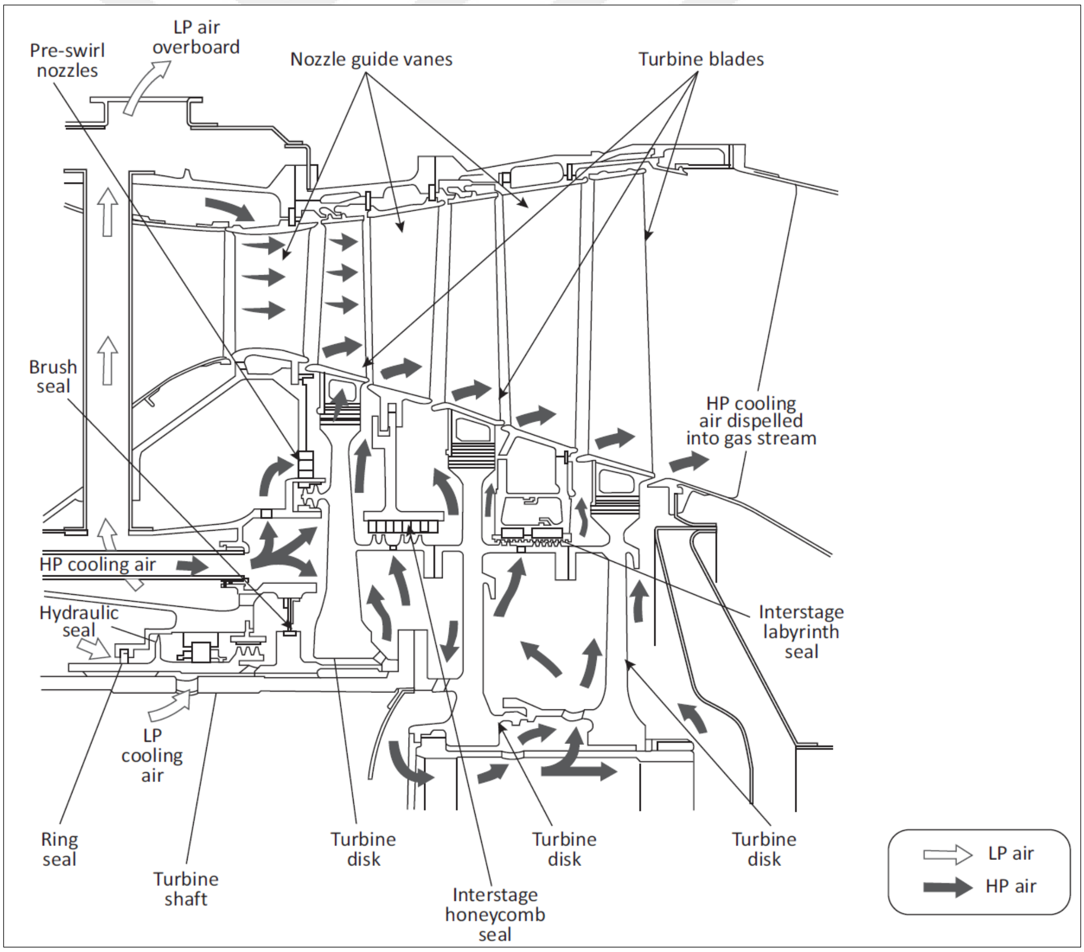

Figure 1.1: Generic turbine SAS network **[1]**.

SAS network from a generic turbine module is shown in **Figure 1.1**. In a gas turbine, first stage nozzle guide vanes (NGVs) are cooled by compressor discharge air, routed inside the vanes from below and above. For the first stage rotor blades, again, compressor discharge air is passed through the inducers and transferred into rotating cavity before pumped into blade cooling slots. Inducers swirl the incoming flow in the direction of rotation causing a reduction in relative total temperature that is essential for cooling and optimizing SAS airflow usage. Second stage NGVs and second stage rotor blades are cooled by an earlier stage compressor offtake air; provided that the supply pressure is adequate. Obviously, the vanes are cooled from above and the blades are cooled from below. Similar routing design is employed for other turbine stages. For the cooling of turbine cases and shrouds either compressor discharge air or mid compressor air are utilized depending on supply pressures and temperatures.

On the other hand, as disks are bulky metal parts supporting rotary structures and suffer from low temperature limits compared to vanes and blades; preventing hot gas ingestion into disk cavities by providing relatively colder sealing airflows is vital. Sealing flows also sweep over disk surfaces and cool them. While carrying out the functions mentioned above, certain precautions need to be taken to limit temperature gradients through transient maneuvers such as accelerations, decelerations, etc. in order to meet life requirements of disks. Overcooling the disks results in higher temperature gradients and excess air use with relatively smaller windage temperature rise. Whereas undercooling causes lower temperature gradients and less air use with relatively higher windage temperature rise; therefore the optimization of sealing airflows plays a significant role is SAS design.

To seal the bearing chambers, pressurization air taken from earlier stages usually, is routed via SAS elements and transferred to chambers. On the way to the chambers, sealing air experiences pressure drop and heating owing to heat transfer from surroundings and windage. Preferably, the biggest pressure drop is observed on critical sealing elements (see **Figure 1.2**) and metering is accomplished via these elements. To avert oil coking inside the chambers, temperature rise of the pressurization air needs to be controlled. To achieve this, clever designs need to be incorporated to reduce heat transfer and windage to the sealing air, which ensures safe and sound operation of bearings within temperature limits devoid of coking inside the oil system components.

Just as the external power of strong athletes depends on the health of their internal flows of blood, water, and air so is true for a gas turbine whose operational life depends heavily on the robust design of its internal cooling and sealing flows **[1]**. A gas turbine engine with dysfunctional SAS design is certainly an unreliable inefficient engine.

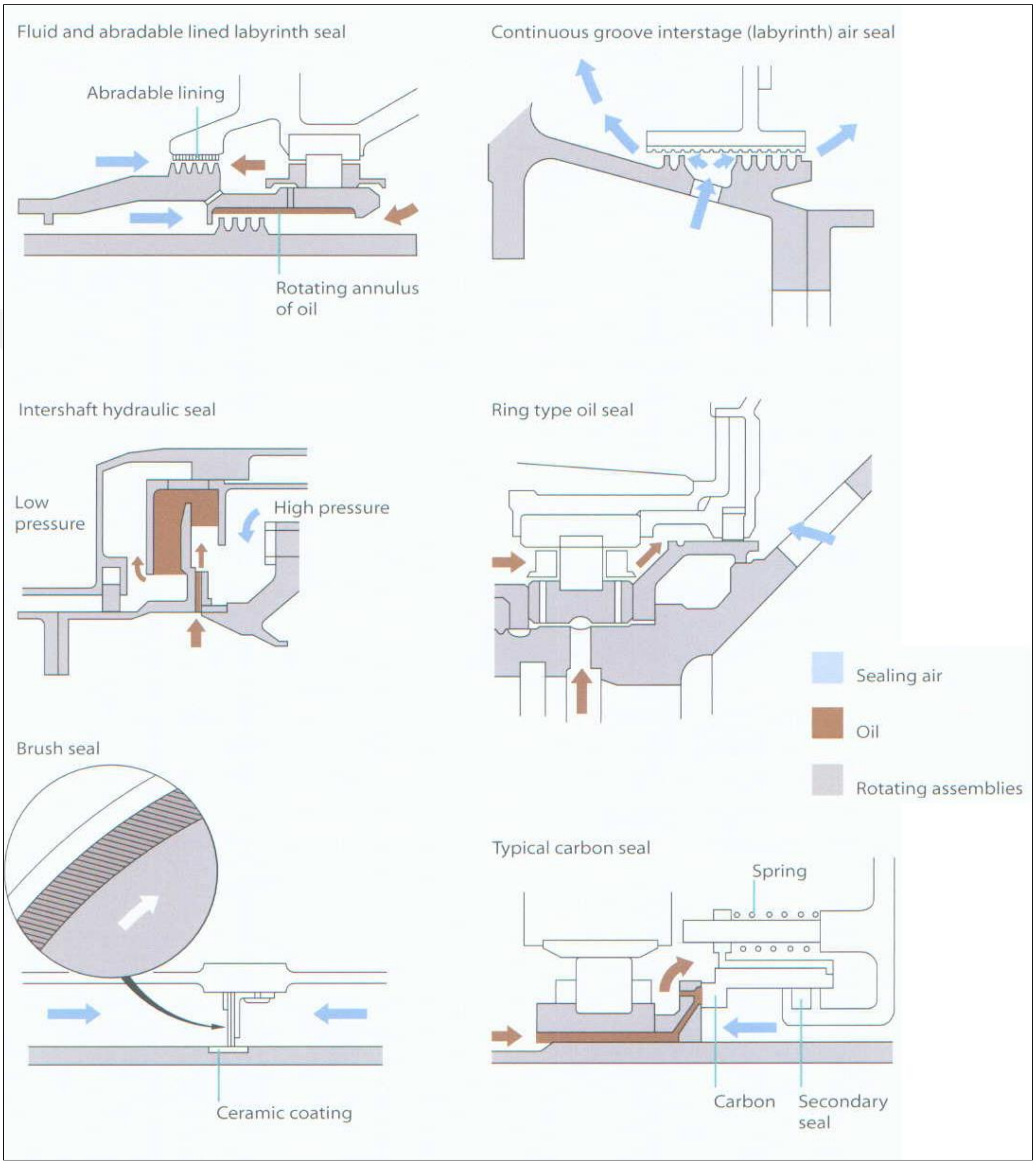

Figure 1.2: Dynamic sealing elements **[2]**.

1.2. Significance of Windage Heating in Gas Turbines

Figure 1.1 shows a typical internal air system design on the turbine side of the engine. The figure illustrates how engineers controlling metal temperatures by using some of the compressed main flow and routing it to critically hot parts, particularly nozzle guide vanes, turbine blades and discs for cooling. Otherwise, these temperatures would cause accelerated degradation of the metal components, shortening fatigue and creep life, eventually reducing the service life of the components.

Cooling air is subject to heating through viscous friction related work transfer from rotor surfaces (what we call windage heating) and heat transfer from the stator and rotor surfaces. Continuously absorbing heat, reducing its own cooling effectiveness demanding more mainstream air usage which however meaning a penalty on performance overall. Therefore, designing for optimum as well as robust cooling presents a significant challenge whilst the ability of more accurately quantifying windage heating is one of the important part of this challenge.

1.3. Significance of This Thesis

Nature of gas turbines possess rotor-stator cavities, which are closely associated with many design constraints such as axial load management, frictional losses, hot gas ingestion, excessive windage loss or flow induced vibration problems. Understanding the flow physics in these cavities, therefore, becomes one of the major concern to improve the component life and the efficiency further in gas turbines.

The rotation of the disk induces a tangential fluid motion and secondary flows, leading to complex flow structures known as three-dimensional boundary layer flow in the literature. This kind of boundary layer displays different characteristics than what we have used to from flat plates. Superposed flow further complicates the situation inside the cavity for example by adding an additional momentum. The flow can be either radially inward, such as leakage flow at the rear side of impellers or radially outward, such as superposed purge flows introduced by designers in the turbine as we saw in **Figure 1.1**. These two example of rotor-stator cavity has been the subject of many studies in the literature due to many constraints mentioned above.

The situation becomes even more complex when considering the surface roughness and the pre-swirl. Because both windage heating and the torques taken from rotating and stationary disks changes with the surface roughness of the disks and swirl of the flow inside the cavity. To investigate the knowledge gaps, this study aim to qualify windage heating in shrouded rotor-stator cavities with superposed radial outflow and how the flow effects, also being affected by windage sources considering pre-swirl of the flow and surface roughness of the disk.

More importantly, as a step towards TEI’s mission to become a leading OEM, a test rig was designed within the scope of this study to measure windage directly from the enthalpy rise of the air in a cavity insulated with epoxy woven glass fabric through rotating disk and stationary casing. Although the rig is still in the installation phase, I believe that these test campaigns will increase TEI’s knowledge and contribute to TEI’s vision of developing globally competitive indigenous power systems. This belief has been the main driver and motivation of this work, which also implies once again the importance of this thesis.

2. THEORETICAL BACKGROUND

In the following, a general review about the physical aspects of the flow in rotor-stator cavities will be given. Due to the extensive number of publications on the topic, only a brief summary can be provided here. A more complete and detailed review up to the year 1989 can be found in Owen and Rogers **[3]**.

2.1. Free Disk and Boundary Layer

Free disk represents a disk rotating in an initially stagnant fluid as a medium. Due to the viscosity, as the disk starts to rotate, the layer of fluid directly in touch with the surface rotates with same angular velocity as the disk because of the no-slip condition, forming a boundary layer in the rotational direction and experiences the same centripetal acceleration. Fluid just above the surface also beginning to rotate but cannot retain same acceleration as the surface and acquires a radial secondary outward flow. In other words, centrifugal forces produced by the rotating disk result in a radial outflow of fluid within the boundary layer. At the distance beyond the boundary layer flow, the fluid is not rotating and no mechanism is available to maintain radial flow. This is compensated by the fluid particles, which are expected to flow in the axial direction onto the disk for reasons of continuity. New fluid particles are then continuously drawn onto the disk and then ejected centrifugally again. Therefore, this is a three-dimensional flow that acts like a pump and this radial outflow is referred to as the pumped flow (pumping flow) or entrainment in the literature where in the case of a free disc known as the “free-disk pumping”.

The principal flows and associated boundary layer for this free disk case are shown in **Figure 2.1**. Although a free rotating disk is not seen in a gas turbine, it represents the base for all rotating-disk systems and indicates the upper limit for the disc pumping flow rate. Therefore, it is very important and can be seen as a first step to understand flow physics inside more complicated cavities.

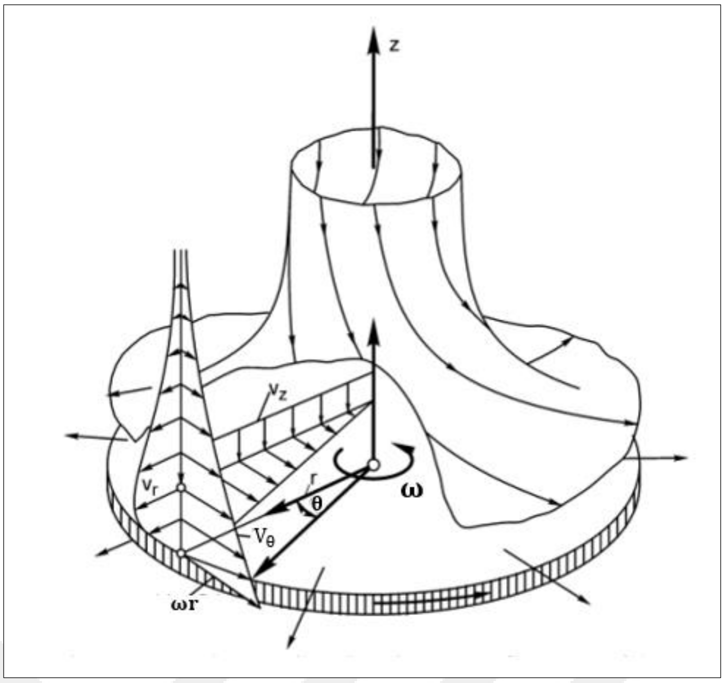

Figure 2.1: Flow structure on the free disk **[4]**.

It is important to emphasize that a boundary layer will form on each side of the disk through which the tangential velocity of the fluid V_θ, is sheared from the disk speed ωr by satisfying the no-slip condition, to zero in the “free-stream” outside of the boundary layer. Because of the symmetry, some analysis and test results are given for both side of disk in the literature, and attention should be taken when using those if interested on one side of the disk only. Also in this thesis, values will be given for only the <u>one side of the disk</u> since in gas turbines each cavities examined separately with different design intents and concerns so that other side of the disk will be another cavity with another concerns.

Within the disk boundary layer, the flow can be laminar or turbulent. Its characteristics are defined by the local rotational Reynolds number, which is governed by the relative magnitude of inertia to viscous effects as defined in equation **(**2.1**)**.

$$Re_{\theta,local} = \frac{\rho \omega r^2}{\mu} \tag{2.1}$$

Where ρ and μ are the density and the dynamic viscosity of the air respectively, ω is the angular speed of the disk and r is the local radius of the disk. If we define it accordingly to the ratio of local radius, r to the disk outer radius, R, with full disk

Reynolds number, it can also be expressed as in equation **(**2.2**)** which will be used often in the analysis of cavities.

$$Re_{\theta,local} = x^2 Re_\theta = \left(\frac{r}{R}\right)^2 \frac{\rho\omega R^2}{\mu} = \frac{\rho\omega r^2}{\mu} \tag{2.2}$$

Where x is the ratio of local radius, r to the disk outer radius, R.

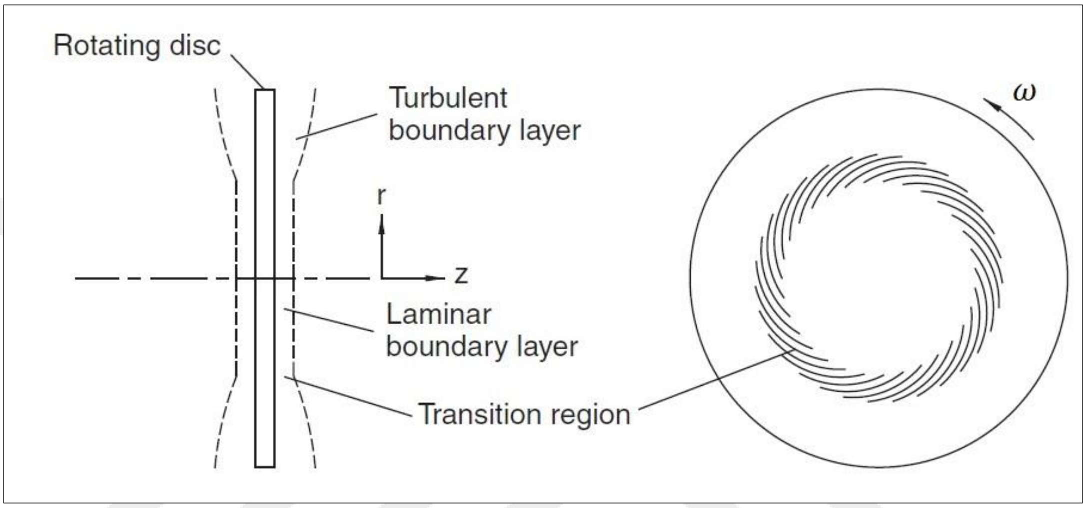

Figure 2.2: Schematic of boundary layers on a rotating disk **[5]**.

For low values of the local rotational Reynolds number, the flow will be laminar over a rotating disk. As the rotational Reynolds number increases from the center of the disk to its periphery, the flow will become unstable and turbulent. The earliest measurements date back to 1940’s. Theodorsen and Regier **[6]** revolving disks in air and also in Freon 12 (refrigerator fluid) to extend Reynolds Numbers as well as Mach numbers range. They found that the laminar flow starts to become unstable for a local rotational Reynolds numbers of about 3.1×10^5 for a highly polished smooth disk. They also achieved to decrease transition number to around 2.2×10^5 for roughened disk with an application of coarse sand glued to the surface of the disk. Later on, experimental findings by Gregory, Stuart, and Walker **[7]** for a rotating perspex disk agrees on that the flow onset instability at local rotational Reynolds numbers between 1.8×10^5 and 2.1×10^5 and transition to turbulence occurs around between 2.7×10^5 and 3×10^5. They using stethoscope to listen at one end of a short tube, the other end of which held very close to rotating disk to detect critical Reynolds number and transition from laminar to turbulent by sound, coming from “silence” in the laminar region, a “regular note” in the transition and a “roar” in the turbulent region.

$$Re_{\theta,local,critical} = x^2 Re_\theta = \frac{\rho\omega r^2}{\mu} \approx 2 \times 10^5 \tag{2.3}$$

$Re_{\theta,critical}$, represents the value of the local rotational Reynolds number at the flow conditions become “critical” with breakdown of laminar flow and start of transitional flow.

$$Re_{\theta,local,turbulent} \approx \frac{\rho\omega r^2}{\mu} \geq 3 \times 10^5 \tag{2.4}$$

Where $Re_{\theta,turbulent}$, represents the value of the local rotational Reynolds number at the boundary layer flow become “turbulent”.

Although these values verified by test results as quoted above the actual value will depend on surface roughness of the disk and specific condition of the flow. For example, some impingement of air jet flow to the disk can trigger turbulence or disk surface can be too rough, in such scenarios; critical value can be lower.

2.1.1. Laminar Flow over the Free Disk

Von Karman **[8]** was the one first pointed out a simple solution of Navier-Stokes equations of motion with incompressible, rotationally symmetric, steady flow and constant viscosity assumptions for a free disk of infinite radius. Obviously, these assumptions are not exactly true for the real situation, but solutions giving valid results for flows that remain laminar. The analysis approach is to reduce the Navier-Stokes equations by transforming them into a set of ordinary differential equations that can be solved numerically. Here we will present only the results and where they coming from? Whole Navier-Stokes Equations in cylindrical polar coordinates can be found in many source (see Childs pp.85-90 **[5]**).

A simple force balance between radial component of the shearing stress, τ_w and centrifugal force of the disk for a volume area dr.ds and height δ, as the boundary layer thickness giving, (see Schlichting pp.103-104 **[4]**).

$$\tau_w sin\alpha \, dr \, ds = \; \rho\omega^2 r \, \delta \, dr \, ds$$

Where α is the angle between the direction in which fluid is slipping and the circumferential velocity of it. On the other hand, assuming that the circumferential of the shear stress must be proportional to the velocity gradient of the circumferential velocity at the wall.

$$\tau_w cos\alpha \sim \; \mu \, \omega r / \, \delta$$

Eliminating τ_w from these two gives,

$$\delta^2 \; \sim \frac{\nu}{\omega} \, tan\alpha$$

Here it is relevant to note that the growth of boundary layer flow over a free disk is proportional to $\sqrt{\nu/\omega}$ and clearly independent from radius, r, resulting in the case of an infinite disk, a finite boundary layer thickness. Unlike a boundary layer flow over a flat plate which giving an infinite boundary layer thickness for an infinite plate as proportional to $\sqrt{\nu x/U_x}$.

In order to integrate the system of equations, Von Karman **[8]** introducing a new variable, a dimensionless distance from the disk, $\xi \sim z/\delta$

$$\xi = z\sqrt{\frac{\omega}{\nu}} \tag{2.5}$$

Then, assuming radially similar profiles for the velocity components and pressure to reduce Navier-Stokes equations to a coupled system of non-linear ordinary differential equations. The full equations of Von Karman were first solved by Cochran **[9]** by using power series expansion near the disk vicinity combined with an asymptotic approach away from it. More accurate results later on given by Owen and Rogers **[3]**.

According to Owen and Rogers **[3]**, the thickness of the boundary layer, δ is defined as the axial distance from the disc at which the tangential velocity of the fluid is equal to 1 percent of the disk speed ωr, then, for laminar flow

$$\delta \approx 5.5\sqrt{\frac{\nu}{\omega}} \tag{2.6}$$

Experimental results by Theodorsen and Regier **[6]** given below also validating this number quite perfectly. Although they compare their laminar results with wrong constant, 2.58 , which was firstly found by Von Karman and highlighted as “Von Karman Laminar δ” in **Figure 2.3**, actual constant corresponding to around 5 from their test results as one can simply measure from the figure by referencing the highlighted boundary layer thickness (2.58). Moreover, it can be seen from the figure that boundary layer thicknesses are constant throughout the laminar region.

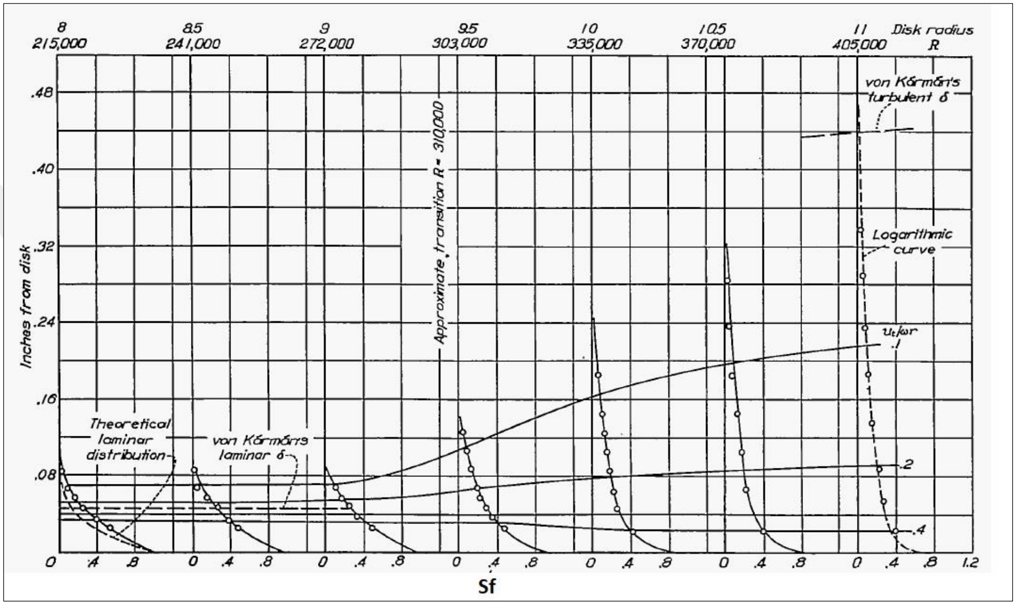

Figure 2.3: Observed tangential velocity profiles ($S_f = V_\theta/\omega r$) and transition from laminar to turbulent on rotating disk **[6]**.

The pumping flow rate, $\dot{m}_0$, for the laminar boundary layer of free disc is given as,

$$\dot{m}_0 = 2.779\,\mu r\left(\frac{\rho\omega r^2}{\mu}\right)^{0.5} \tag{2.7}$$

Or in a non-dimensional form,

$$\frac{\dot{m}_0}{\mu r} = 2.779\,(x^2 Re_\theta)^{0.5} = 2.779\left(\frac{\rho\omega r^2}{\mu}\right)^{0.5} \tag{2.8}$$

Note that for a laminar boundary layer the disk pumping flow rate varies with r^2; since the disk area also varies with r^2, the axial velocity of entrainment remains uniform over whole disk from its center to outer periphery. Now it is necessary to introduce dimensionless moment coefficient of the disk,C_m, for the one side of the disk as,

$$C_m = \frac{M}{\frac{1}{2}\rho\omega^2 R^5} \qquad (2.9)$$

Which is given for laminar flow by,

$$C_m = \ 1.935\ Re_\theta^{-0.5} = 1.935\ \left(\frac{\rho\omega R^2}{\mu}\right)^{-0.5} \qquad (2.10)$$

2.1.2. Turbulent Flow over the Free Disk

The flow in the rotating disk vicinity becomes turbulent at local rotational Reynolds Number larger than, $\rho\omega r^2/\mu\ \geq 3 \times 10^5$ in the same way as the flow about a flat plate. The difference is that instead of free stream velocity U_∞, one need to define the boundary layer according to tangential velocity of the disk, ωr, to zero tangential velocity of the fluid in the free stream in case of a “free disk”. Making same estimation of the balance of viscous and centrifugal forces for the turbulent case giving the radial component of shearing stress relation as,

$$\tau_w sin\alpha\ dr\ ds = \ \ \rho\omega^2 r\ \delta\ dr\ ds$$

On the other hand, for the tangential component of shearing stress, using resistance formula that is developed for pipe flow, replacing U_∞ by the tangential velocity, ωr. (See. Schlichting pp. 648-649 **[4]**).

$$\frac{\tau_w}{\rho(\omega r)^2} = 0.0225\ \left(\frac{\nu}{\omega r\delta}\right)^{\frac{1}{4}} \qquad (2.11)$$

Which follows,

$$\tau_w cos\alpha \sim \rho(\omega r)^{7/4}\ (\nu/\delta)^{1/4}$$

Equating shear stress τ_w, results in,

$$\delta \sim r^{3/5} (\nu/\omega)^{1/5}$$

Which shows us that in the turbulent case, the boundary layer thickness increases in proportion to $r^{3/5}$, and does not remain constant as in the laminar case.

These numbers coming from pipe experiments. The n-th power velocity distribution law are related to Blasius's law of friction and actually, 1/7-th power velocity distribution law can be deduced from Blasius's resistance formula. (See Schlichting pp. 596-602 **[4]**). This relation was firstly found by L. Prandtl **[10]** and J. Nikuradse **[11]**, allowing them to extend the range of Reynolds number by using smaller exponents into Blasius's equation which meaning that the exponent $n = 7$ in the power law should have to be replaced by 8, 9 etc. to have an agreement with their measured data for higher Reynolds Numbers. Suitable power law exponents given in **Table 2.1** below as a function of Reynolds numbers by Schlichting **[4]** between ranges of $10^4 < Re_\theta < 10^6$. Later studies showed that these values also valid for boundary layers on flat plates as well as for rotating disk modifying U_∞ by the tangential velocity, ωr over a certain range of Reynolds Number.

Table 2.1: Exponent n and associated $C(n)$ as a function of Reynolds number **[4]**.

$\boldsymbol{n}$	**1/7**	**1/8**	**1/9**	**1/10**
$\boldsymbol{C(n)}$	8.74	9.71	10.6	11.5
$\boldsymbol{Re_\theta}$	$< 0.6 \times 10^5$	3×10^5	7×10^5	1.7×10^6

This discovery have a great importance in the fundamental theory of turbulent flow and eventually developing to Universal velocity-distribution law or what we known as Universal law of the wall today. In Computational Fluid Dynamics (CFD), this law still in use with normalized axes as u+ and y+, to find out velocity distribution near the wall and correct wall shear stress accordingly.

Von Karman **[8]** was the one first investigated the turbulent boundary layer on a rotating disk, assuming the variation of the tangential velocity component through the boundary layer obeys 1/7-th power law, and solving turbulent momentum integral equations for the "free disk". According to Owen and Rogers **[3]**, the solution of the integral equations for the thickness of the boundary layer, pumping flow rate and moment coefficients were, respectively:

$$\frac{\delta}{r} = 0.5261\left(\frac{\rho\omega r^2}{\mu}\right)^{-0.2} \tag{2.12}$$

$$\frac{\dot{m}_0}{\mu r} = 0.2186\left(\frac{\rho\omega r^2}{\mu}\right)^{0.8} \tag{2.13}$$

$$C_m = 0.0729\, Re_\theta^{-0.2} \tag{2.14}$$

It is important to emphasize that these values are derived for 1/7-th power profile that is often in use for turbulent case. On the other hand, Dorfman **[12]** using logarithmic profiles for boundary layer, then solving the equations explicitly for each range and combining his solution for $10^4 < Re_\theta < 10^9$ to give the equation,

$$C_m = 0.491\big(log_{10}(Re_\theta)\big)^{-2.58} \tag{2.15}$$

Later on Bayley and Owen **[13]** rotating 762 mm diameter disk in air up to the range of $Re_\theta \sim 4 \times 10^6$ and correlating the moment coefficients by

$$C_m = 0.0655\, Re_\theta^{-0.186} \tag{2.16}$$

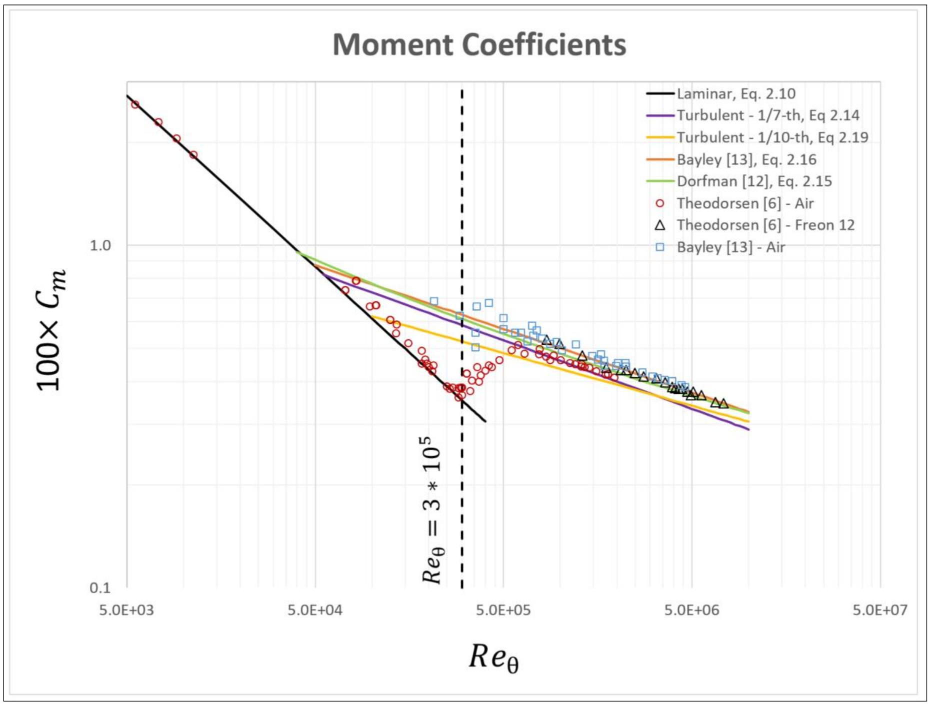

Figure 2.4: Variation of moment coefficients with Reynolds numbers (Theory vs Experiment).

All experimental results and theoretical curves compared in **Figure 2.4**. According to figure, 1/7-th power law underestimates measured C_m values at higher Reynolds numbers of $Re_\theta > 10^6$.At this point, although, using higher exponent for power law profile could give better agreements for moment coefficient at Reynolds Numbers higher than $Re_\theta > 10^6$, using logarithmic profile seems more appropriate.

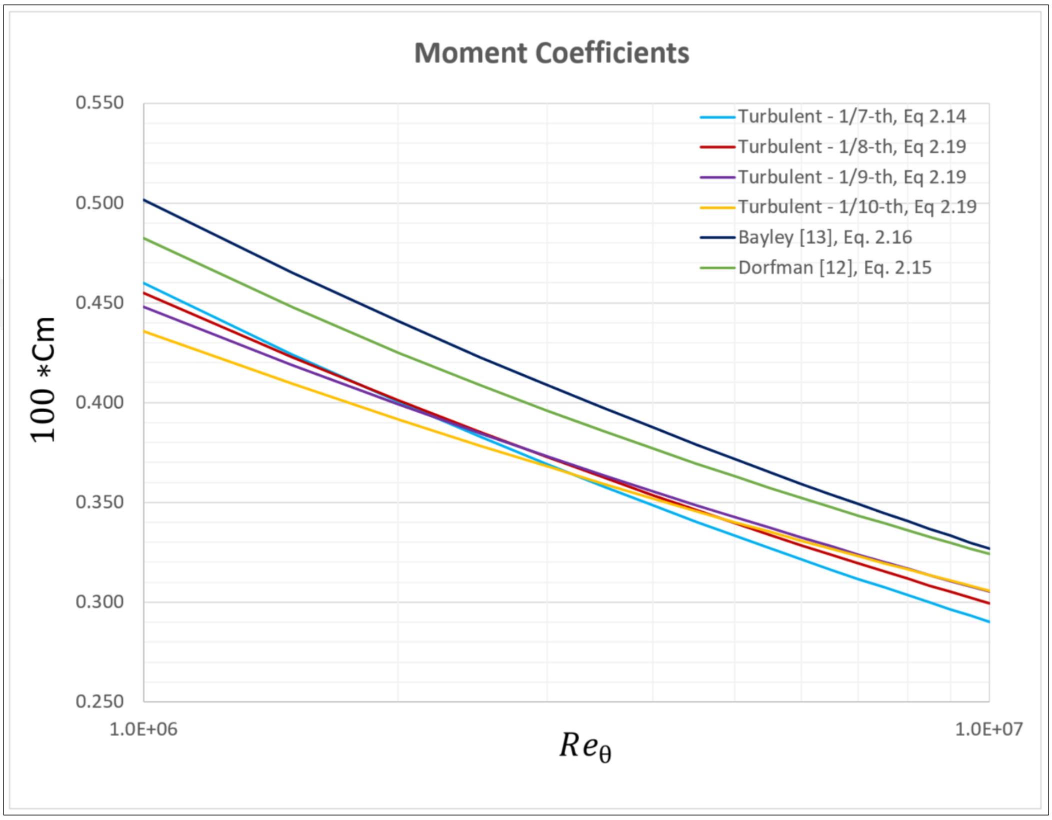

Figure 2.5: Comparison of moment coefficients correlations.

However, over the range of $10^6 < Re_\theta < 10^7$, they only differs 10 percent between 1/7-th power profile and Dorfman's logarithmic profile as one can see from the **Figure 2.5**. Beyond the range of $Re_\theta \geq 10^7$, this difference getting higher between 1/7-th power and logarithmic profile to around 20 percent but getting closer with 1/10-th power profile to around 5 percent but neither of them supported by any measurements. Thus, considering the whole range of turbulent case, $10^5 < Re_\theta < 10^7$, we can say that 1/7-th power law holds fairly well predictions for the moment coefficients overall.

Same deduction, however, cannot be made for disk pumping flow rate. Childs **[5]** (see pp. 104-121) giving whole solution of equations with a general n-th power law, for the thickness of the boundary layer, disk pumping flow rate and moment coefficients were, respectively:

$$\frac{\delta}{r} = \gamma \left(\frac{\rho\omega r^2}{\mu}\right)^{\left(-\frac{2}{n+3}\right)} \tag{2.17}$$

$$\frac{\dot{m}_0}{\mu r} = \varepsilon_m \left(\frac{\rho\omega r^2}{\mu}\right)^{\frac{n+1}{n+3}} \tag{2.18}$$

$$C_m = \varepsilon_M \, Re_\theta^{\left(-\frac{2}{n+3}\right)} \tag{2.19}$$

Where the corresponding coefficients given as in **Table 2.2**,

Table 2.2: Power law coefficients **[5]**.

$\boldsymbol{n}$	7	8	9	10
$\boldsymbol{\gamma}$	0.5263	0.4973	0.4791	0.4633
$\boldsymbol{\varepsilon_m}$	0.2187	0.1869	0.1643	0.1460
$\boldsymbol{\varepsilon_M}$	0.0729	0.0561	0.0448	0.0365

Dorfman **[12]** using logarithmic profiles, obtains solution for disk pumping rate which as,

$$\frac{\dot{m}_0}{\mu r} = 0.0705 \left(\frac{\rho\omega r^2}{\mu}\right)^{0.8774} \tag{2.20}$$

Results giving in the **Figure 2.6**, in the non-dimensional form $\dot{m}_0/\pi\rho\omega R^3$ to compare with the available test results in the literature. Power law approximations resulting in more than 20 to 35 percent difference in the range of $10^5 < Re_\theta < 10^7$ and there is no measurement for higher Reynolds numbers to clarify the situation.

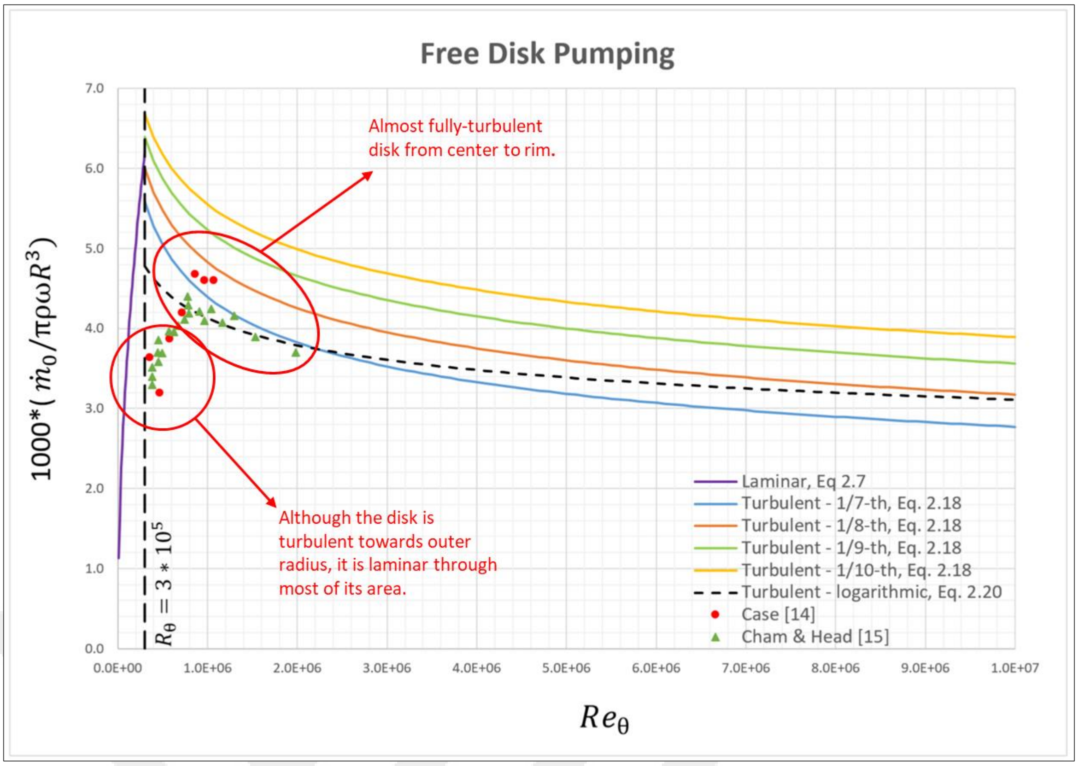

Figure 2.6: Dimensionless disk pumping mass flow rate as a function of Reynolds number (Theory vs Experiment: Case **[14]**, Cham & Head **[15]**).

Note that these equations for the n-th power law velocity profiles, assuming turbulent boundary layer right from to $r = 0$, to outer radius, R and calculating flow rates accordingly. Moreover, rotational Reynolds numbers are written for full disk as well as the measured data from experiments. Thus, we are actually looking at rpm as Reynold Numbers on the x-axis. At transition Reynolds numbers around, $Re_\theta \approx 3 \times 10^5$, the disk will be laminar over most of its area while we are calculating disk pumping rates for fully turbulent disk. In Head **[15]**'s case, half of the disk area was laminar at low Reynolds number, $Re_\theta \approx 4 \times 10^5$; and when they increased to $Re_\theta \approx 10^6$,where the disk turbulent over about % 80 of its area, measured data closing to 1/7-th power profile curve and Dorfman's logarithmic profile; and as it goes to higher Reynolds numbers have an almost perfect match with both. This phenomenon clearer when we add laminar disk pumping curve to figure, with same assumption that laminar boundary layer right from to $r = 0$, to outer radius R. Measured data is showing the transition from laminar to turbulent ones for pumping flow rates. However, the data available only up to $Re_\theta \approx 2 \times 10^6$.

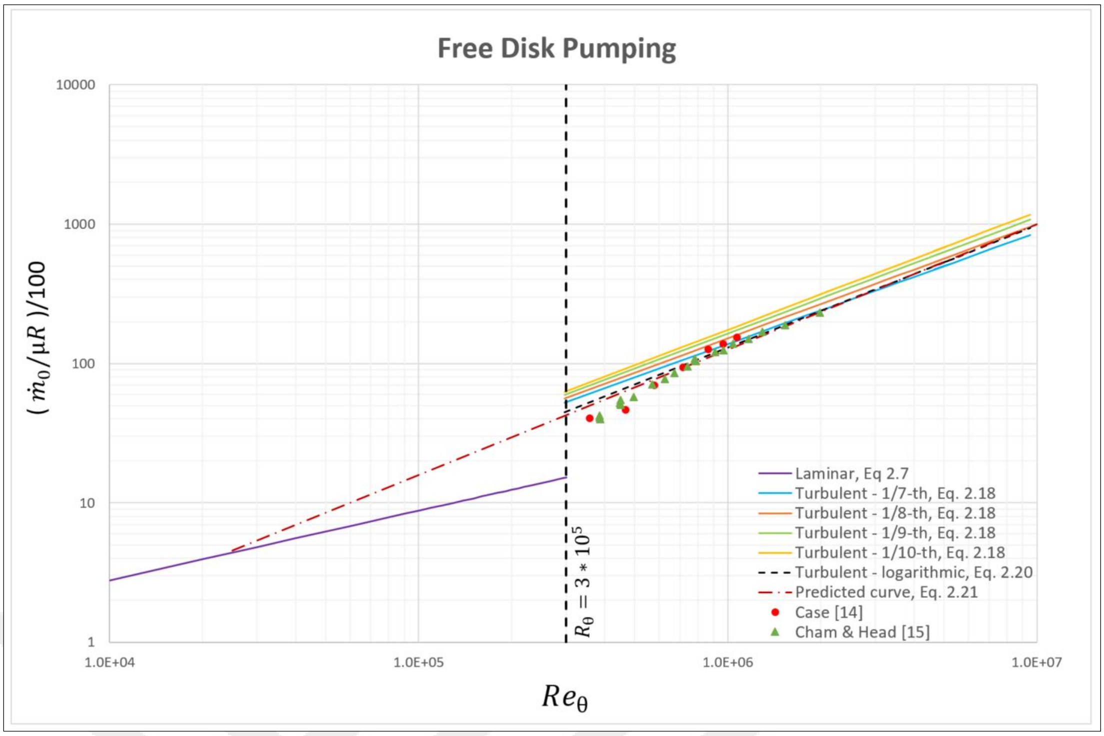

Figure 2.7: Non-dimensional disk pumping mass flow rate as a function of Reynolds number (Theory vs Experiment: Case **[14]**, Head **[15]**).

If we draw the same graph on logarithmic scale for a non-dimensional form, $\dot{m}_0/\mu R$, given in **Figure 2.7**, one can see theoretical curves like a linear lines. At transition, same phenomenon appears and measured flow rates coming between laminar and turbulent curves. It was possible to estimate an exponential curve below equation **(**2.21**)** to compare with our "free disk pumping" test results. Predicted curve's slope fitted to measured data at high Reynolds, $Re_\theta \geq 10^6$, but converging to higher exponent of power law profile similar to logarithmic curve up to maximum Reynolds number of $Re_\theta < 10^7$.

$$\frac{\dot{m}_0}{\mu r} = 0.05\left(\frac{\rho\omega r^2}{\mu}\right)^{0.9} \tag{2.21}$$

Although these equations have many assumptions and using the data that is developed from pipe experiments, they giving reasonable answers about "free disk" and showing the basic dynamics behind the rotational flow. In gas turbines, fluid is not stationary, in no case, near rotating disks but also itself rotating at some portion of the rotor angular velocity, what we call swirl ratio.

2.2. Flow on a Rotating Disk beneath a Forced Vortex

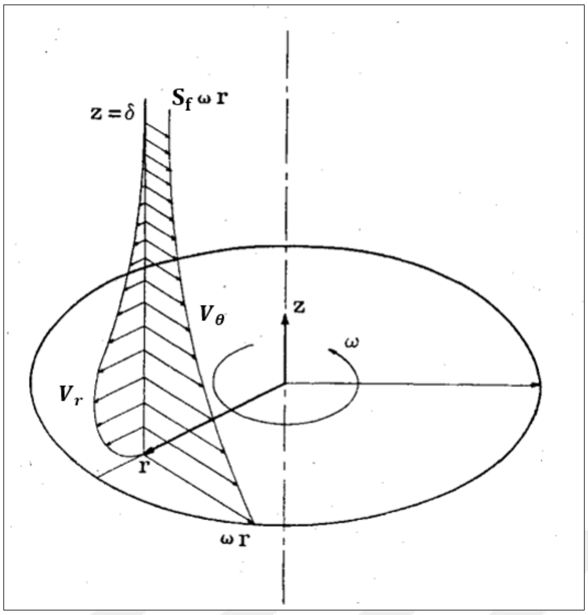

Figure 2.8: Flow structure beneath a forced vortex (Newman **[16]**).

Figure 2.8 showing the boundary layer on a rotating disk where outside the boundary layer the fluid itself rotates as a forced vortex at a portion of the disk angular velocity. The ratio of the fluid angular velocity to the disk angular velocity is defined by the swirl factor S_f.

$$S_f = \frac{\omega_{fluid}}{\omega_{rotor}} = \frac{V_{\theta_{fluid}}}{\omega_{rotor} r} \tag{2.22}$$

For the "free disk" , $S_f = 0$, the variation of the tangential component of velocity, which gives rise to the radial pumping flow, varies from 0 to ωr, however, beneath a forced vortex, the equivalent variation through the boundary layer from $S_f \omega r$ to ωr. If, $S_f = 1$, meaning the fluid is getting into solid-body rotation with the disk so that there will be no boundary layer formation between. It is very important to understand that without the boundary layer formation, no shear related work transfer such us windage would occur to the fluid, neither the disk pumping flow. More interestingly, if $S_f > 1$, firstly discussed by Batchelor **[17]**, the flow will pump radially inward and work transfer will take place from fluid to disk not the other way. Therefore, swirl is the real key to understand complex flow structures inside cavities.

In gas turbines, swirl factor generally somewhere between zero and unity, $0 < S_f < 1$ in the rotor-stator cavities. For those cases, Newman **[16]** extends the momentum integral method of Von Karman to where the outer flow is not stationary but rotating at some constant fraction of the rotor angular velocity. Assuming boundary layers turbulent right from to $r = 0$, to outer radius, R, Sultanian **[1]** giving the formula with a correction to free disk pumping mass flow rates for the one-seventh power law profile as,

$$\left(\frac{\dot{m}_0}{\mu r}\right)_{n=7} = 0.219\left(\frac{\rho\omega r^2}{\mu}\right)^{0.8}\zeta \qquad (2.23)$$

Where the correction factor given as

$$\zeta = \left(1 - 0.51S_f\right)\left(1 - S_f\right)^{1.6} \qquad (2.24)$$

ζ, correction factor plotted in the **Figure 2.9** yielding maximum pumping flow rate in a “free disk” case and no pumping flow in a “solid-body rotation” case as discussed above.

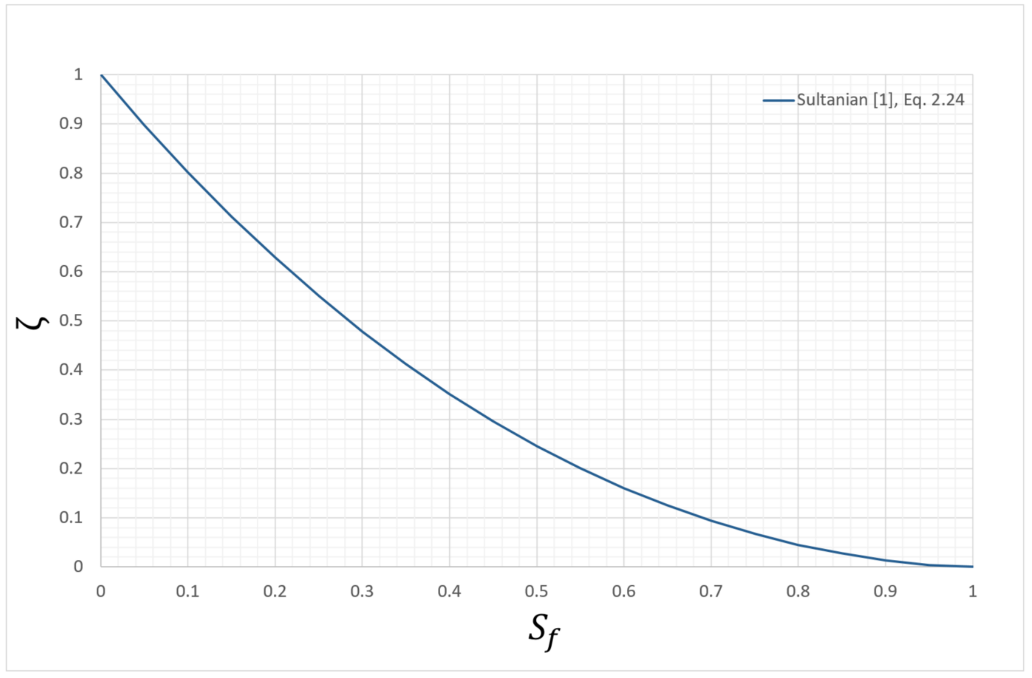

Figure 2.9: Fraction to “free disk” pumping mass flow rate vs swirl factor **[1]**.

Since the disk pumping flow rates are strongly depended on swirl factor, it seems reasonable that not only pumping flow but also transition values, $Re_{\theta,critical}$, would reduce as S_f increase, however, according to test results of Daily and Nece **[18]** in an enclosed cavity where S_f was around 0.4, instability starting at $Re_\theta \approx 1.8 \times 10^5$, and transition to turbulent around $Re_\theta \approx 3 \times 10^5$.

To find out the difference between n-th power law profiles at high Reynolds numbers, it was possible to generate them from Newman **[16]** as a correction factor to “free disk” pumping like Sultanian **[1]** did, which resulting in, for n = 8, 9, and 10 respectively as follows,

$$\left(\frac{\dot{m}_0}{\mu r}\right)_{n=8} = 0.1869\left(\frac{\rho\omega r^2}{\mu}\right)^{0.818}\left(1 - 0.4948S_f^3 + 1.8313S_f^2 - 2.3376S_f\right) \tag{2.25}$$

$$\left(\frac{\dot{m}_0}{\mu r}\right)_{n=9} = 0.1643\left(\frac{\rho\omega r^2}{\mu}\right)^{0.833}\left(1 - 0.709S_f^3 + 2.2349S_f^2 - 2.5262S_f\right) \tag{2.26}$$

$$\left(\frac{\dot{m}_0}{\mu r}\right)_{n=10} = 0.1460\left(\frac{\rho\omega r^2}{\mu}\right)^{0.846}\left(1 - 0.9107S_f^3 + 2.6064S_f^2 - 2.6952S_f\right) \tag{2.27}$$

Figure 2.10 plotted for the maximum Reynolds number, $Re_\theta \approx 5.4 \times 10^6$ (more than 90 percent of the disk area is turbulent) that will be reached in our “rotor-stator cavity tests”. At $S_f = 0.4$, pumping flow rates differ less than 10 percent between 1/7-th and 1/10-th power profile and for higher swirl factors, lines are merging so that exponent of the n-th law approximations do not matter anymore. However, in terms of “free disk” case there is a significant difference that more than 35 percent between 1/7-th and 1/10-th power profile, and even more than 10 percent between n=7 and n=8.

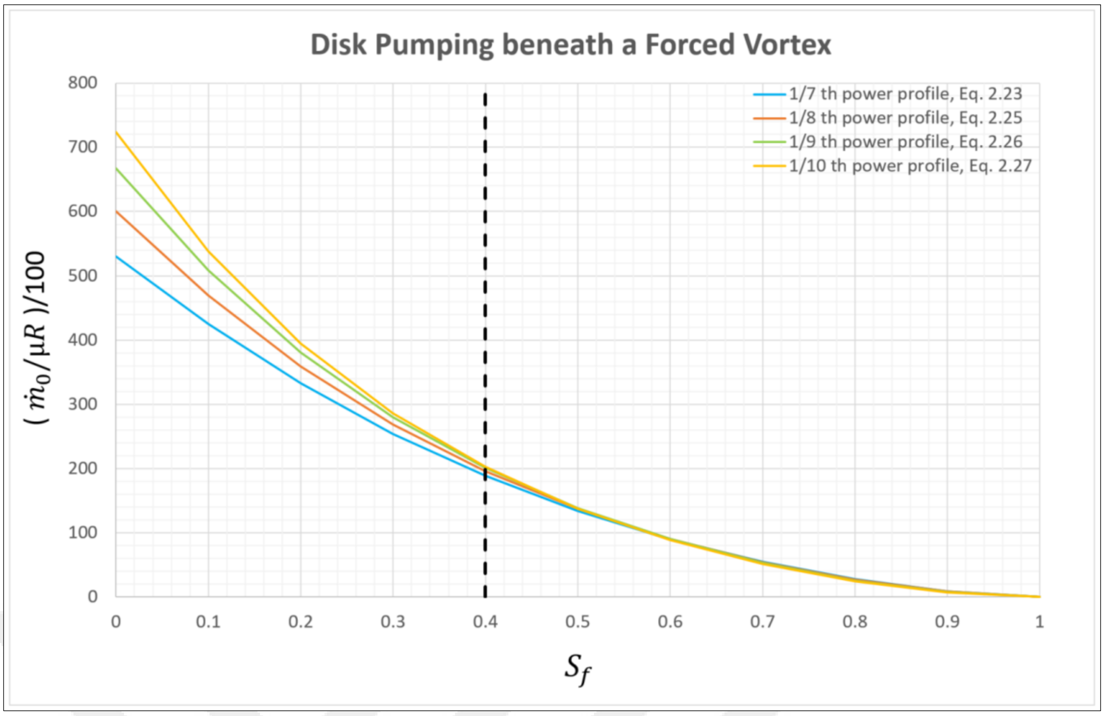

Figure 2.10: Variation of dimensionless disk pumping mass flow rates with swirl factor.

For our test campaigns, the superposed flow will be introduced into the cavity from the center of the stationary disk without swirl. Thus, swirls inside the cavity are expected to be lower than 0.4. Although, we will only measure the disk pumping flow rates for "free disk" cases in tests, it is important to estimate pumping flow for non-zero S_f values. Because this phenomenon, actually, affecting the amount of air rotating inside the cavity, which can effect windage distribution through ingestion phenomenon when the superposed flow rates not satisfying the disk pumping need.

The associated prediction of boundary layer thickness also presented by Newman **[16]** as a function of S_f and plotted for $n = 7$ and 8 in **Figure 2.11**. One can see how non-dimensional boundary layer thickness varying from its max value at "free disk" ($S_f = 0$) case to zero thickness when $S_f = 1$ which representing the solid body rotation meaning no formation of boundary layer.

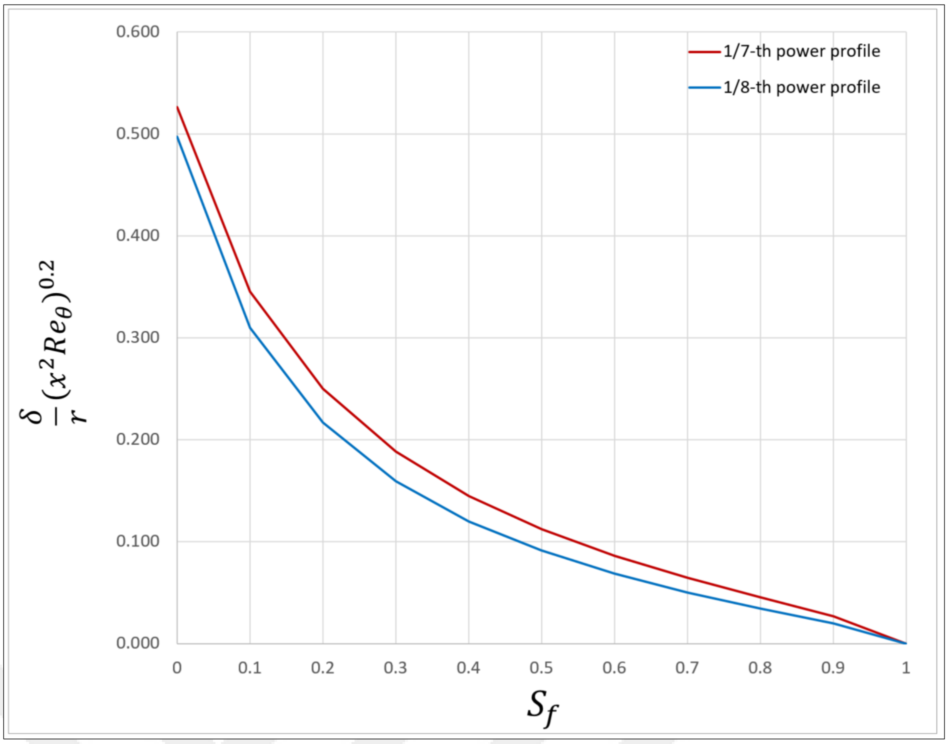

Figure 2.11: Variation of non-dimensional boundary layer thickness with swirl factor (re-plotted from Newman **[16]**).

2.3. Cavity Flows

The rotor-stator and rotor-rotor cavities are the most dominant and common features encountered in the secondary flow systems of gas turbines. Assuming a turbulent cooling and sealing flows in these systems, the interaction of the flow on a rotor surface, a stator surface, and the mass flow rate associated with radially outward or inward flow is responsible for a variety of flow structures found in these cavities. A good understanding of these flow features, therefore, is key to their one-dimensional modelling for the flow network of these secondary flow systems. In the scope of this study, only rotor-stator cavities with no through-flow and with superposed radial outflow will be examined.

2.3.1. Enclosed Rotor-Stator Cavity with No Through-flow

As we enclose the rotor disk with a stationary disk, shroud, casing etc., flow inside the cavity also starting to rotate at some swirl, what we called “core rotation”. In other words, now disk rotates under some forced vortex not in a stationary state anymore as was in the “free disk” case.

Batchelor **[17]**, generalized Karman's solution of the Navier-Stokes equations that describe the steady viscous flow in the vicinity of a rotating disk, and obtained differential equations that can be used to predict the flow near a rotating disk when the fluid at infinity is rotating about the same axis, and also for the flow between two rotating coaxial disks. He does not obtain any explicit solutions but uses physical arguments and general properties of the ordinary differential equations to predict the general nature of the flow. He defined rotor-stator flow structures as an extreme case to co-rotating cavity with one disk rotating slower than the other disk at some distance away and for the slower one’s angular velocity limiting to zero.

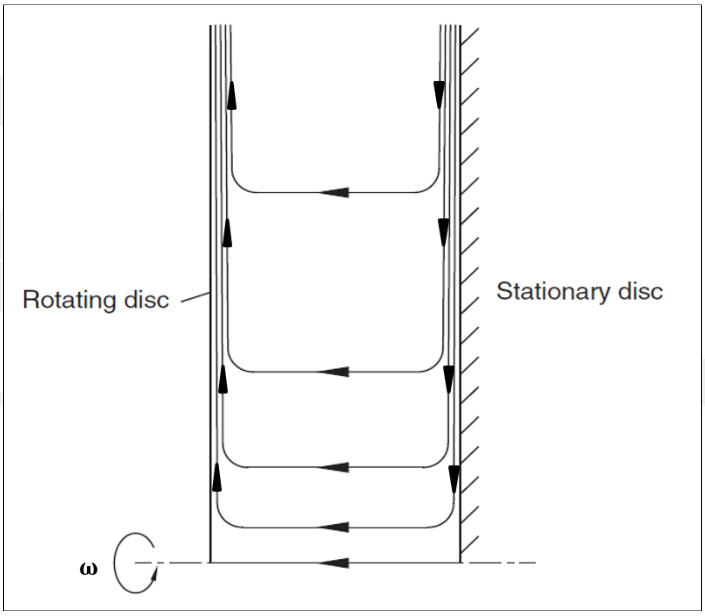

Figure 2.12: Batchelor type of flow structure **[5]**.

Figure 2.12 showing type of flow structures, which normally best describes the flow we encounter in rotor-stator cavities; known as Batchelor flow model in the literature. Batchelor predicting these flow behaviors by looking at swirl factors, S_f which is giving rise to radial pumping flow at the rotor that is rotating faster than the fluid, and at the stationary casing side resulting in radially inward flow where the fluid is rotating outside the boundary layer, as mentioned before like $S_f > 1$ case. Because the disk demanding flow to pump and demanding more from center to its radially outward, it is continuously being fed from the radially inward flow along the stator and axially from the stator boundary to the rotor boundary layer.

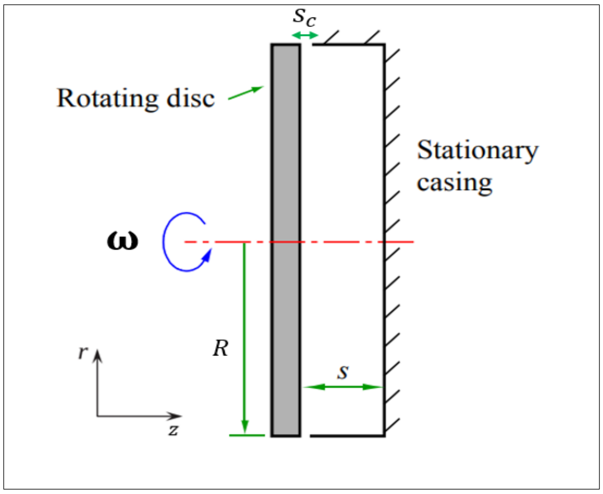

Figure 2.13: Idealised enclosed rotor-stator cavity.

It is now relevant to define the gap ratio, which is the ratio of the axial distance, s between rotor and stator to radius of the disk as given in equation ((2.28**)**. When written according to the axial clearance s_c, it is called as clearance ratio G_c.

$$G = \frac{s}{R} \left(G_c = \frac{s_c}{R} \right) \tag{2.28}$$

Gap ratio is very important in terms of flow structures we see inside the cavity therefore defined here and will be examined soon.

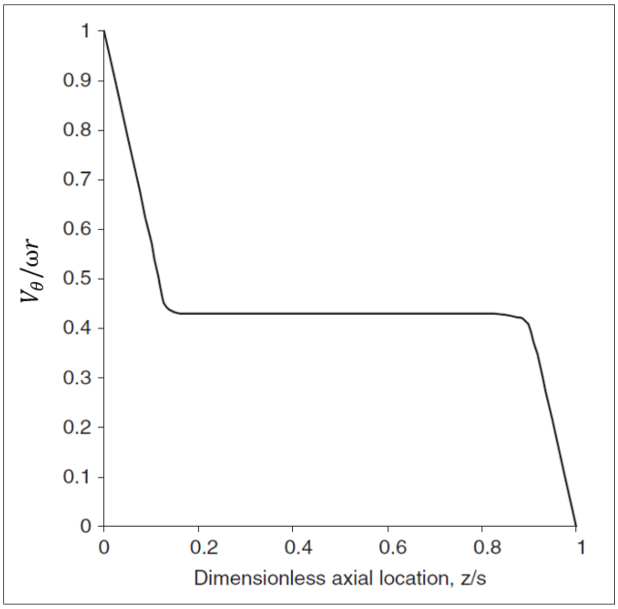

Figure 2.14: Variation of swirl factor with axial location across a rotor-stator cavity (Batchelor type of flow structure) **[5]**.

Figure 2.14 shows typical variation of the tangential velocity of the fluid between the rotor and stator discs in Batchelor type flow. The gap ratio is large enough; allowing two separate boundary layers, with the tangential velocity of the fluid v_θ, sheared from the disk speed, ωr, at the rotor boundary layer, to some constant swirl in the core region and then reducing to zero in the stator boundary layer through no slip condition. This constant swirl core region also known as core rotation as we mentioned before.

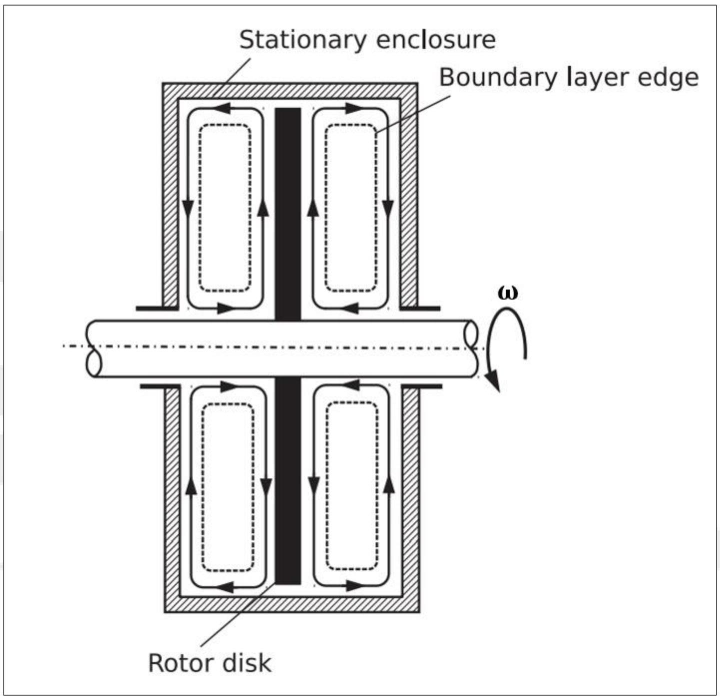

Figure 2.15: Rotating disk in an enclosed cavity **[1]**.

For an enclosed rotor-stator disc system where no throughflow supplied or extracted as shown in **Figure 2.15**, between the rotor and stator boundary layers, there is an inviscid core of fluid that rotates at some portion of the rotor angular velocity; and is likely to be expected to rotate at less than half of the disk angular velocity, $S_f < 0.5$. As the gap ratio decrease, core swirl ratio tends to rotate closer to, $S_f \approx 0.5$ as reported by Daily **[19]**. Although the torque on the stator is not doing any work, there is continuous work transfer into the fluid from the rotor disk with windage. Hence, the fluid temperature within a perfectly insulated enclosure will rise continuously.

If the gap ratio decreases to some degree or there is superposed radial outflow to suppress core rotation or both conditions exists; there can be no more separate but merged boundary layer from rotor tangential velocity to zero velocity in the stator boundary layer which known as Stewartson flow model that shown in **Figure 2.16**. Today, we know that depending on flow conditions both models are valid and can be seen in rotor-stator cavities.

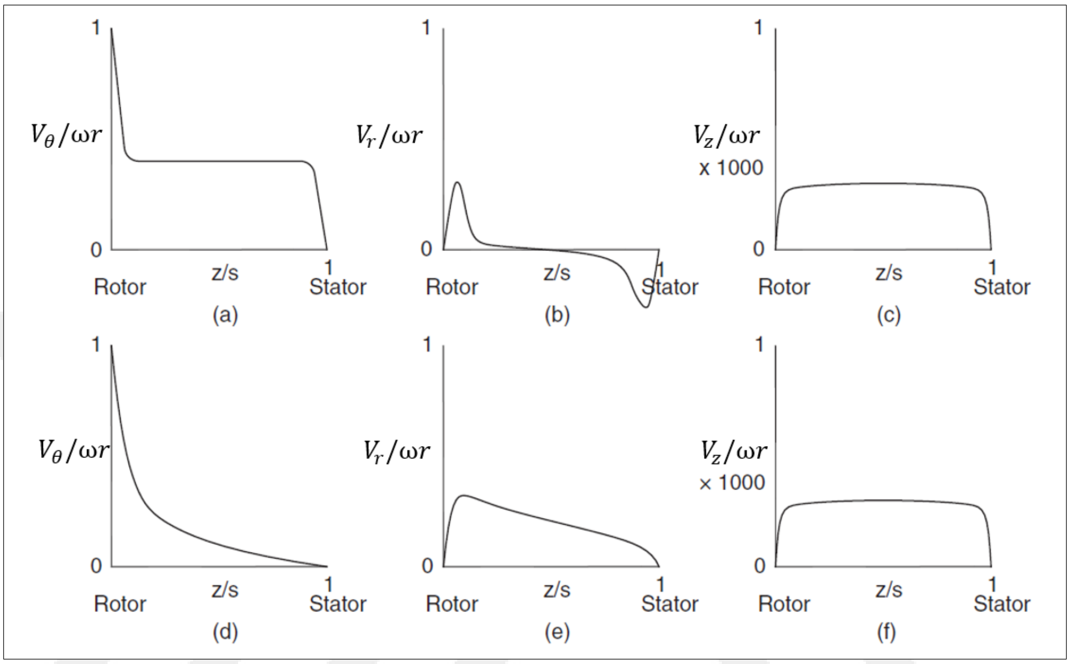

Figure 2.16: Characteristic velocity profiles in a rotor-stator cavity (a) to (c) Batchelor type of flow structure; (d) to (f) Stewartson type of flow structure **[5]**.

Daily and Nece **[19]** carried out an extensive experimental and theoretical studies for the flow in an enclosed rotating disk. Their tests representing the fundamental fluid mechanics associated with this type of flow. In the experiments, velocity, pressure and torque measurements are conducted for varying the disk speed and gap ratios. The torque data were obtained over a range of rotational Reynolds numbers from $Re_\theta = 10^3$ to $Re_\theta = 10^7$ for gap ratios from $G = 0.0127$ to $G = 0.217$ for a constant tip clearance while also pressure and velocity measurements taken for both laminar and turbulent flows. As a result, they were able to identify four basic flow regimes for each that can occur depending on the rotational Reynolds number and the gap ratio as shown in **Figure 2.17**.

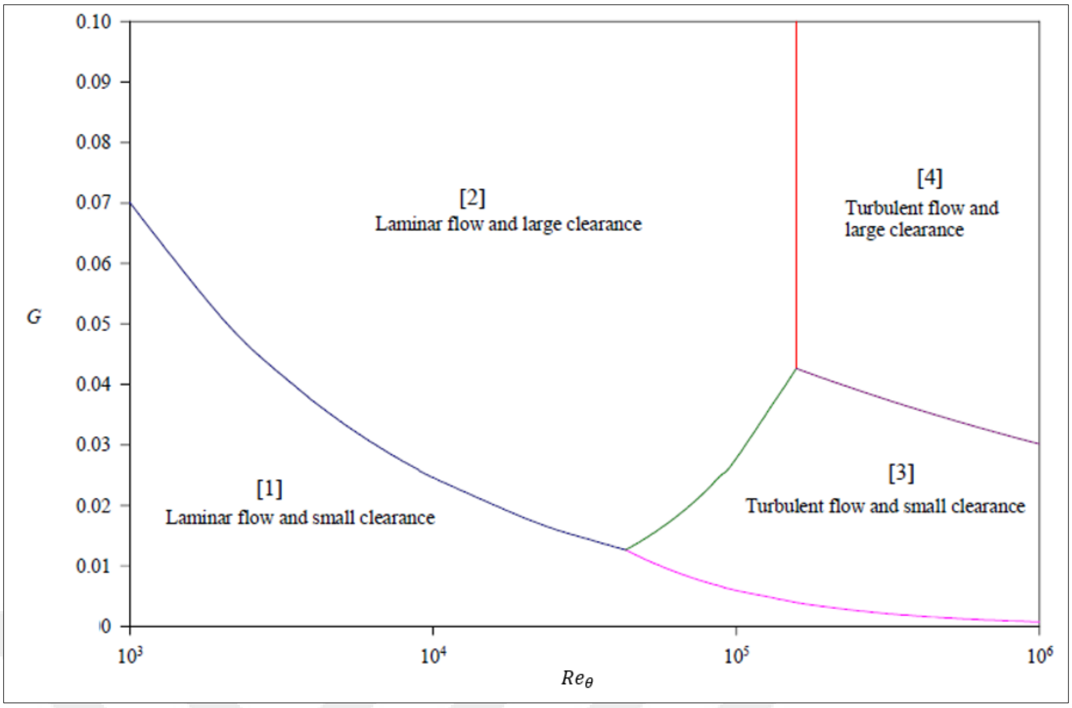

Figure 2.17: Regimes of flow for an enclosed rotor-stator cavity **[19]**.

In their experiments the test fluids was water and oils and data were obtained over a wide range of rotational Reynolds Numbers and gap ratios. The schematic of the test rig is shown in **Figure 2.18**. During the experiments, there is no superposed flow is provided, despite a closed recirculation system through pipes with a heat exchanger to keep constant density and viscosity of the test fluids. Torques are measured with SR-4 water-proofed bonded strain gages that were placed at angles of 45 degree from the shaft center line, to have a bridge circuit measuring torsional stresses only. Voltage differences from the circuit are taken off through slip rings mounted on the shaft. A DC galvanometer serves as the indicating device. As the strain-gage was located on the fluid side of the shaft seal, only measured the torques coming from fluid resistance so that no deductions being needed for bearing and sealing friction. To express the resistance of the disk surfaces only they even calculated the torques coming from the tip of the disk by using disks with different thicknesses and making corrections to measured data. Their test results often in use in the literature, therefore, explained in detail. Later on, authors upgrading same test rig to take measurements for rough disks and casings as well as for throughflow cases which will be explained in detail later on.

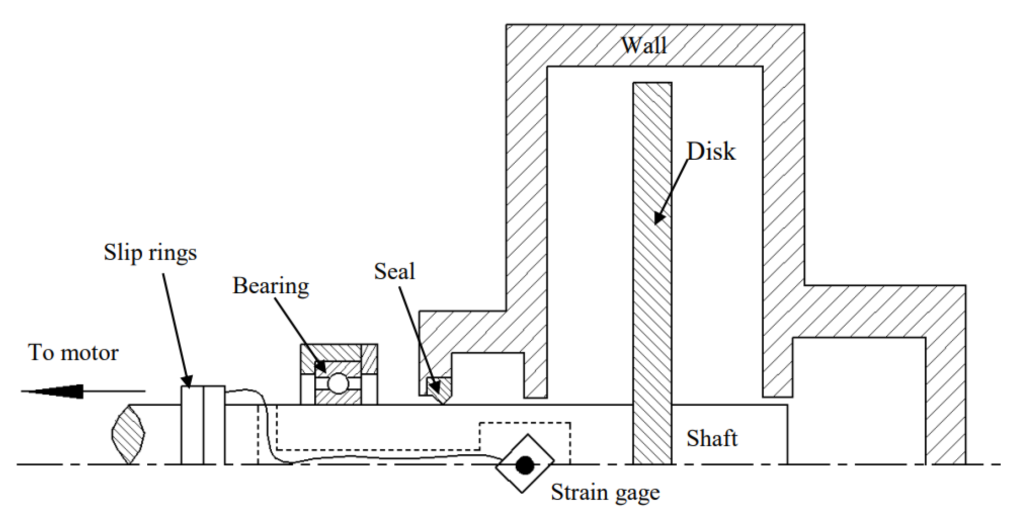

Figure 2.18: Test rig structure of Daily and Nece **[19]** (Taken from Bo Hu **[20]**).

Determined relationships for the moment coefficient for each of these regimes, for the one side of the wetted disk in the range of rotational Reynolds numbers, $10^3 < Re_\theta < 10^7$ and gap ratios, $0.0127 < G < 0.217$ are given below,

- Regime I : Laminar flow, small gap ratio, merged boundary layers,

$$C_{m_1} = \frac{\pi}{G \cdot Re_\theta} \tag{2.29}$$

- Regime II : Laminar flow, large gap ratio, separate boundary layers,

$$C_{m_2} = 1.85 \cdot G^{0.1} Re_\theta^{-0.5} \tag{2.30}$$

- Regime III : Turbulent flow, small gap ratio, merged boundary layers,

$$C_{m_3} = 0.04 \cdot G^{-0.167} Re_\theta^{-0.25} \tag{2.31}$$

- Regime IV : Turbulent flow, large gap ratio, separate boundary layers,

$$C_{m_4} = 0.051 \cdot G^{0.1} Re_\theta^{-0.2} \tag{2.32}$$

In gas turbines high Reynolds numbers achieved throughout the most critical cycles so that flow generally turbulent, also gaps between rotating disk and stationary parts are large enough that the regime IV becoming the most likely to occur in design applications. The small gap ratio cases (regime I and regime III) essentially presents a Stewartson-type of flow while the other two regimes corresponding to Batchelor-flow characterized by a separate boundary layer with an inviscid core region rotating between. For merged boundary layers (Regime I and III), the frictional resistance decreases with increasing gap ratio as a result of the reduced velocity gradients. In contrast, the frictional resistance increases with raising gap width in case of separated boundary layers (Regime II and IV) due to braking influence of enclosed cavity and closing to case of a "free disk" which represents the maximum resistance as we discussed before.

For the boundary layer growth, Daily and others **[18]** taking direct measurements at three radial location (x= 0.469, 0.648, 0.828) for the case of $G = 0.0665$ and $Re_\theta = 6.9 \times 10^5$ by sending different superposed flow rates so that changing core rotation swirls and giving the relation as a function of core rotation swirl as,

$$\frac{\delta}{r} = 0.4\left(1 - S_f\right)^2 \left(\frac{\rho\omega r^2}{\mu}\right)^{-0.2} \tag{2.33}$$

In **Figure 2.19**, Equation **(**2.33**)** plotted with those theoretically extended by Newman for turbulent 1/7th and 1/8th power law assumption which giving similar results to empirical correlation derived from tests.

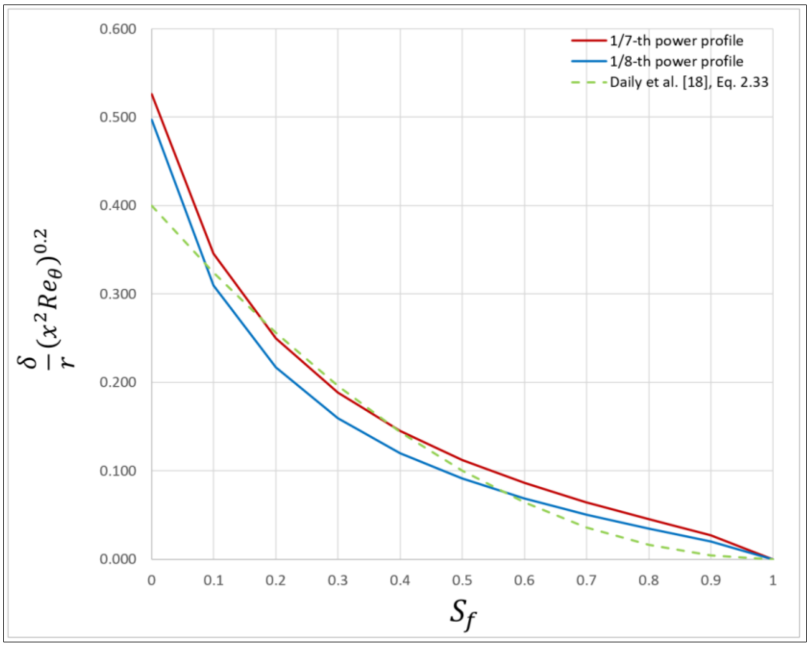

Figure 2.19: Variation of non-dimensional boundary layer thickness with swirl factor.

2.3.2. Shrouded Rotor-Stator Cavity with Superposed Radial Outflow

Superposed radial outflow rotor-stator cavities commonly encountered in the turbine side of the engine; first investigations, therefore, starts with hot gas ingestion related issues which often seen problem in gas turbines that could have catastrophic consequences for the engine. Questions arise on necessary superposed flow rates coupled with better rim seal designs to prevent ingestion into these critical cavities.

For a low superposed flow rates that are not fully meeting the demand of disk pumping flow, external fluid can be ingest and flow radially inward from the edge of the shroud into the cavity. This phenomenon often known as “rotationally-induced ingress”. Later researches with the development of test rigs and measurement techniques, however, shows “externally-induced ingress” is the dominant mechanism for hot gas ingestion in gas turbines, which happens due to the unsteady non-axisymmetric variation of pressure in the annulus created by the presence of guide vanes and rotor blades. **[21]**

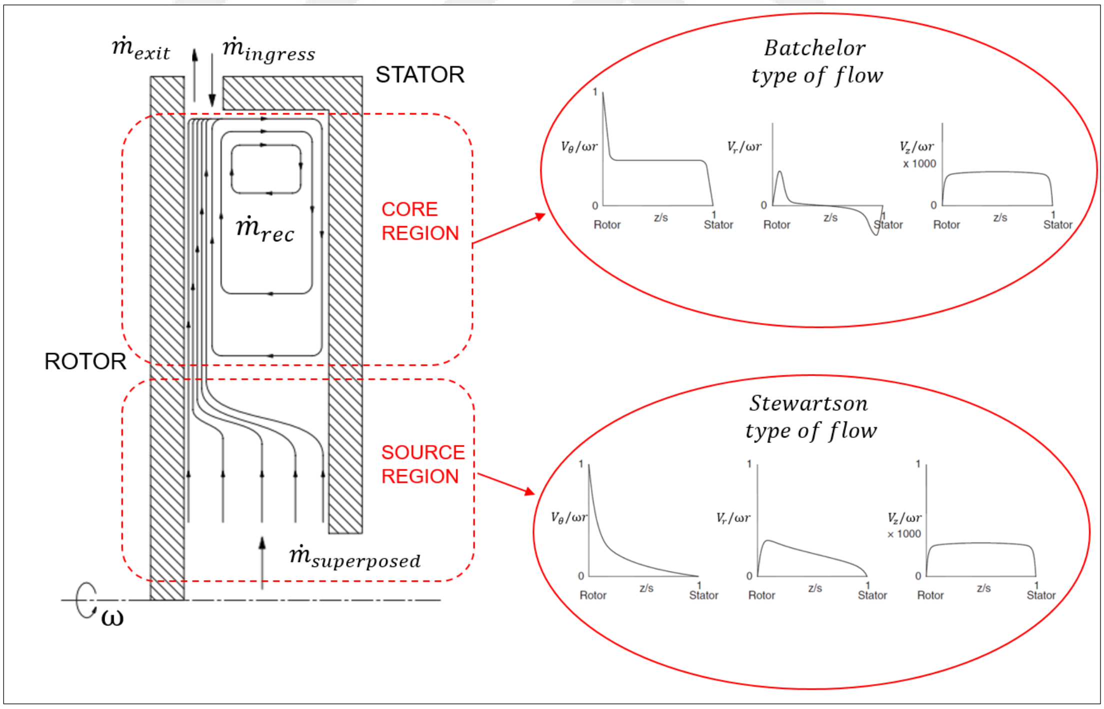

Figure 2.20: Batchelor and Stewartson type of flow structures in rotor-stator cavity with superposed radial outflow.

Owen **[22]** solving the linear Ekman-layer equations for the case a rotor-stator system with superposed radial outflow. For laminar flow, the predicted core rotation swirl agrees well with Daily's **[18]** experimental measurements when the superimposed flow rate is zero, but underestimating the core rotation when the flow rate is non-zero. For turbulent flow, the linear theory underestimates the core rotation under all conditions. More importantly, reporting that Stewartson type flow forms in the lower inlet area of the cavity (named source region) while, as the radius increases, the mass flow is increasingly entrained into the rotor boundary layer and Batchelor type flow dominates from there to periphery of the cavity as shown in **Figure 2.20**. Today, many researches shows that it is indeed the case for radial inlet while also similar for the axial inlet with a few exceptions.

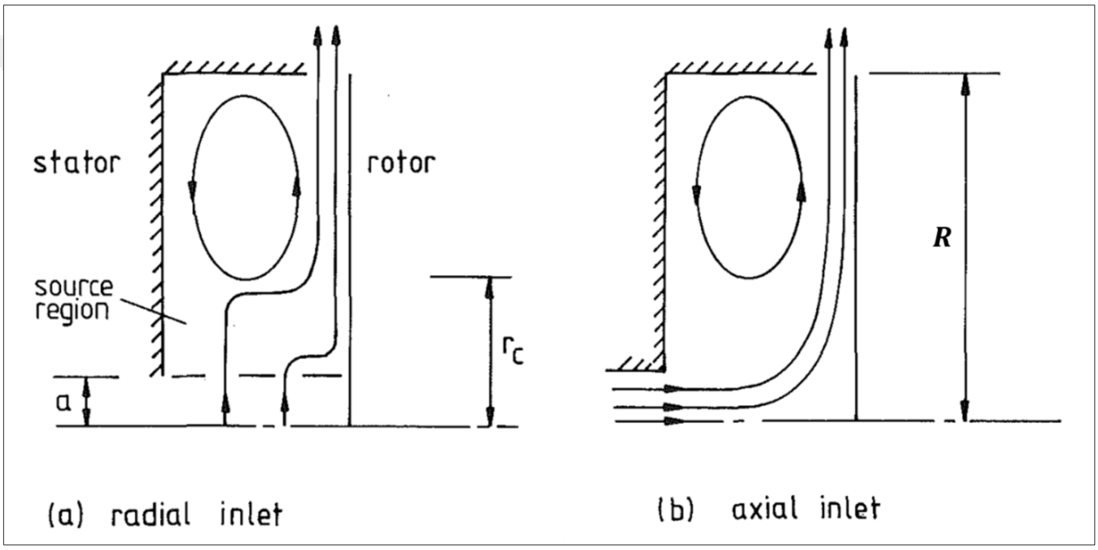

Figure 2.21: Simplified flow structure in a rotor-stator cavity with superposed outflow of fluid **[22]**.

In general, the core rotation decreases with a radial outflow and flow structures that can initially be characterized by the Batchelor model can tend toward that of the Stewartson model with no or very little core rotation as the radial outflow increases. The turbulent flow inside rotor-stator cavity with superimposed through-flow is quite complex and cannot be explained with two basic flow model all the time. One thing for sure, radial outflow will suppress the core rotation, results in lower swirl factors throughout the cavity; and even completely make an end of the core rotation if gap ratio is low enough.

Non-dimensional flow rate coefficient for superposed flows defined as,

$$C_w = \frac{\dot{m}_{superposed}}{\mu R} \tag{2.34}$$

One should not be confused by the fact that some papers referring $C_w = 0$ as “free disk” when comparing their results with and without superposed flow but they actually referring to no throughflow case as “free disk”. Since if there is a stationary casing that allowing the core rotation took place, it will not be a rotating disk in a stationary fluid anymore as in its defined condition of “free disk”. In contrast, it will be the minimum resistance case with maximum core rotation comparing to superposed flow ones.

Daily et al. **[18]**, correlating their test results with superposed flow by a direct relation between swirl ratio and turbulent parameter which is defined as

$$\lambda_t = C_w \, Re_\theta^{-0.8} \tag{2.35}$$

Or according to volumetric flow rates as Daily defined

$$\lambda_t = \frac{Q}{\omega R^3} \, Re_\theta^{0.2} = C_w \, Re_\theta^{-0.8} \tag{2.36}$$

They giving core rotation swirl vs turbulent parameter equation as,

$$\frac{S_f}{S_{f_0}} = \frac{1}{C_0 \lambda_t x^{-\frac{13}{5}} + 1} \tag{2.37}$$

Where S_{f_0} representing the core rotation swirl factor without superposed flow and C_0 some constant they use to fit the curve according to their measured data. Measured values of S_{f_0} for different gap ratios are given by Daily et al. **[18]** in **Table 2.3**, which is decreasing with increasing gap ratios as we expect.

Table 2.3: Measured core swirl factors with zero throughflow rates for different gap ratios by Daily et al. **[18]**.

G	S_{f_0}
0.027	0.475
0.069	0.450
0.124	0.420

Authors based their correlation on velocity measurements at $x = 0.469, 0.648, 0.828$ for the gap ratios $G = 0.055, 0.060$ at $Re_\theta = 6.9 \times 10^5$ as given in **Figure 2.22**, and choose $S_{f_0} = 0.5$ and $C_0 = 12.74$ which are given acceptable approximations at all three radius. As it can be seen from measurements, swirl ratios reducing with increasing superposed flow rates throughout the cavity and Daily et al. **[18]** giving correlation as,

$$\frac{S_f}{S_{f_0}} = \left(12.74\,\lambda_t x^{-\frac{13}{5}} + 1\right)^{-1} \tag{2.38}$$

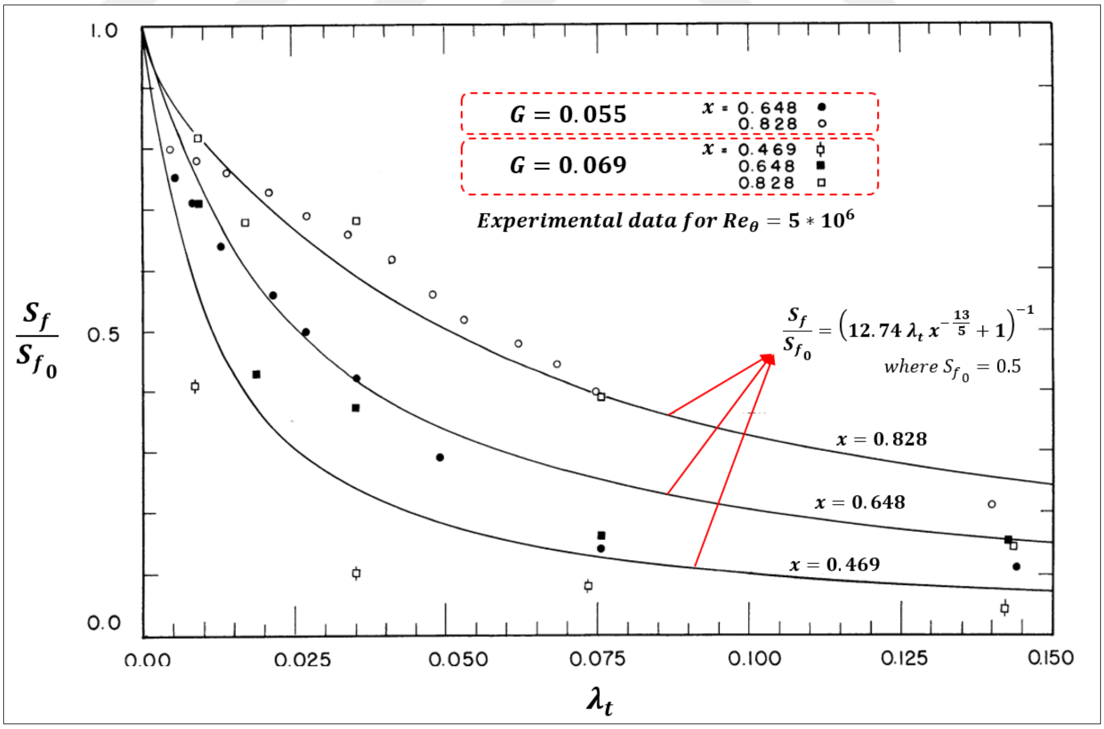

Figure 2.22: Comparison of measured and calculated core rotation swirl factors by Daily et al. **[18]**.

Owen **[22]** using radius ratio, $x = r/R$, which was firstly introduced by Daily et al. **[18]**, to correct flow parameters to local values

- Local Reynolds number: $Re_{\theta}\, x^2 = \frac{\rho \omega r^2}{\mu}$ (2.39)

- Local through-flow rate: $C_w x^{-1} = \frac{\dot{m}_{superposed}}{\mu r}$ (2.40)

- Local turbulent parameter: $\lambda_t x^{-\frac{13}{5}} = \frac{\dot{m}_{superposed}}{\mu r} \left(\frac{\rho \omega r^2}{\mu}\right)^{-0.8}$ (2.41)

Owen **[22]** using this approach to find out the where the disk pumping flow rate exceeds the superposed flow ones so that suggesting the point will be the radius at which the “source region” ends and core rotation begins. Moreover, giving a direct relation between the core rotation swirl and the local turbulent parameter by solving the boundary layer equations with an assumption that core rotation will be completely suppressed when superposed flow rates equal to “free disk pumping” value. However, one should be aware of that core rotation not only depends on superposed flow rates but also on the gap ratio of the cavity. For this reason, this approach will not be true for all the time. Owen **[22]** also stating that this approximation underestimating the flow rate necessary to suppress the core rotation by comparing it with test results.

However, Owen’s approach is being adopted by many authors and Da Soghe et al. **[23]** suggesting a new empirical correlation using a more extended database obtained from numerical simulations (CFD) with $\lambda_t x^{-\frac{13}{5}}$ up to 0.4 as,

$$\frac{S_f}{S_{f_0}} = \frac{1}{1 + 7.55\lambda_t x^{-\frac{13}{5}} + \left(13.52\lambda_t x^{-\frac{13}{5}}\right)^2 + \left(188.56\lambda_t x^{-\frac{13}{5}}\right)^3} \tag{2.42}$$

Extensive measurements performed by Poncet **[24]** using a two-component laser-Doppler anemometer technique. This method is based on the accurate measurement of the Doppler shift of laser light scattered by small particles carried along with the fluid.

They compared their test results for three values of the Reynolds number, two gap ratios of the cavity, and four flow rates, with second order RSM model; and found an almost perfect match except for the small gap ratio. (They took measurements at gap ratios as low as $G = 0.012$ which corresponding to 3 mm space between rotor and stator and the main defect was due to the size of the probe (0.8 mm), which is becoming large compared to this gap).

Poncet **[24]** reporting that for low superposed flow rates, the flow keeping the characteristics of a closed cavity (Batchelor type of flow) while in the case of a strong through-flow rates, reverting to Stewartson type flow with only one boundary layer on the rotating disk. Authors giving direct correlations between core rotation swirl and local turbulent parameter, also plotting the measured data in a log-log representation suggesting that the transition from Batchelor to Stewartson occurs when local turbulent parameter, $\lambda_t x^{-\frac{13}{5}}$ at the range of 0.16 to 0.19.

Their correlation for Batchelor type of flow given as,

$$S_f = 2\left(-5.9\left(\lambda_t x^{-13/5}\right)/2\pi + 0.63\right)^{5/7} - 1 \tag{2.43}$$

For a Stewartson types of flow as,

$$S_f = 0.032 + 0.32e^{-\left(\lambda_t x^{-13/5}\right)/0.056\pi} \tag{2.44}$$

It was possible to localize the experimental data of Daily **[18]** to compare with Poncet **[24]** , also experimental data of El Oun and Pincombe taken from Owen **[3]**, plotted in **Figure 2.23** with Daily’s experimental correlation where $S_{f_0} = 0.5$, and Da Soghe’s equation with $S_{f_0} = 0.46$.

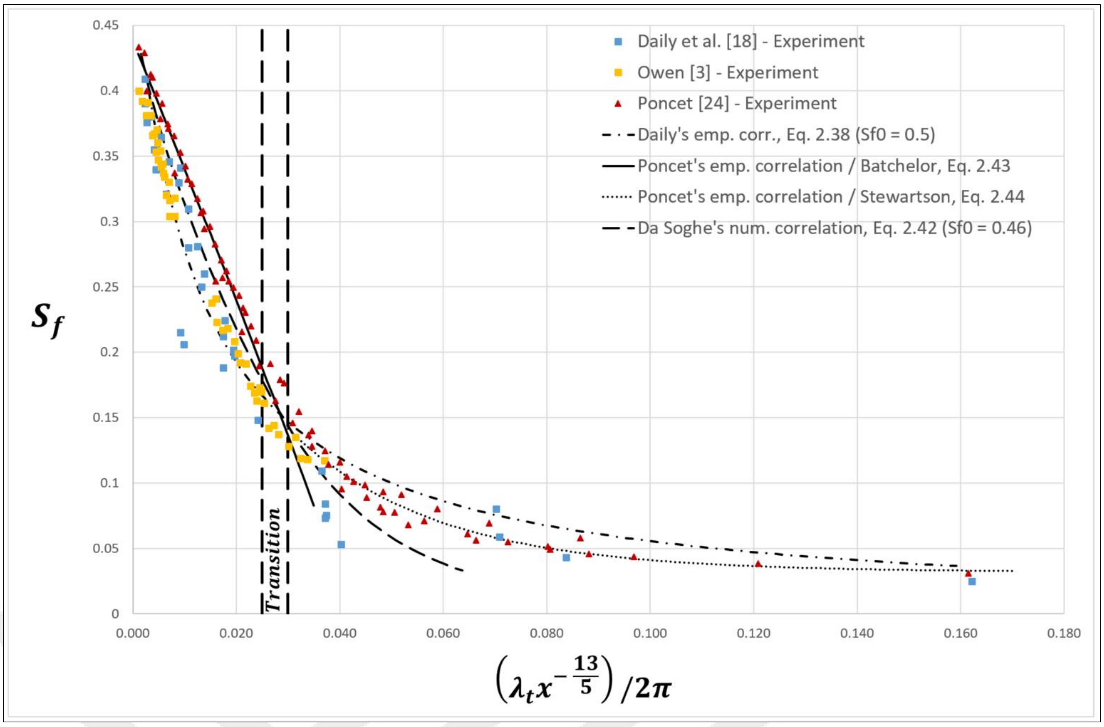

Figure 2.23: Comparison of correlations with experimental data.

Daily's and Poncet's correlations giving up to 20 percent difference at both regions. This difference can be explained with the gap ratios. In Poncet's test rig maximum gap ratio was $G = 0.036$, while in Daily's measurements taken at $G = 0.055$ and $G = 0.069$. Since both gaps are large enough to form two separate boundary layer, lower the gap ratio results in higher core rotation swirl as in Poncet's. Therefore, gap ratios in Daily's rig, at low through-flow rates where core rotation dominates, giving lower core rotation values.

More recently Micio et al. **[25]** taking same velocity measurements on a unshrouded rotor-stator cavity with a gap ratio of $G = 0.025$; using Kiel head probes located on stator disk to deduce corresponding velocities. Due to their unshrouded rotor-stator cavity rig (shroud enclosing the cavity better so that allowing higher core rotation values), swirl values becoming even lower than Daily's. Their experimental data fitting to Daily's correlation with $S_{f_0} = 0.426$ as given in **Figure 2.24**.

Authors explaining that the experimental data becoming more dispersed as the through-flow rates increases due to the dynamic pressure associated with the low tangential velocities becoming close to the uncertainty of their instrumentation.

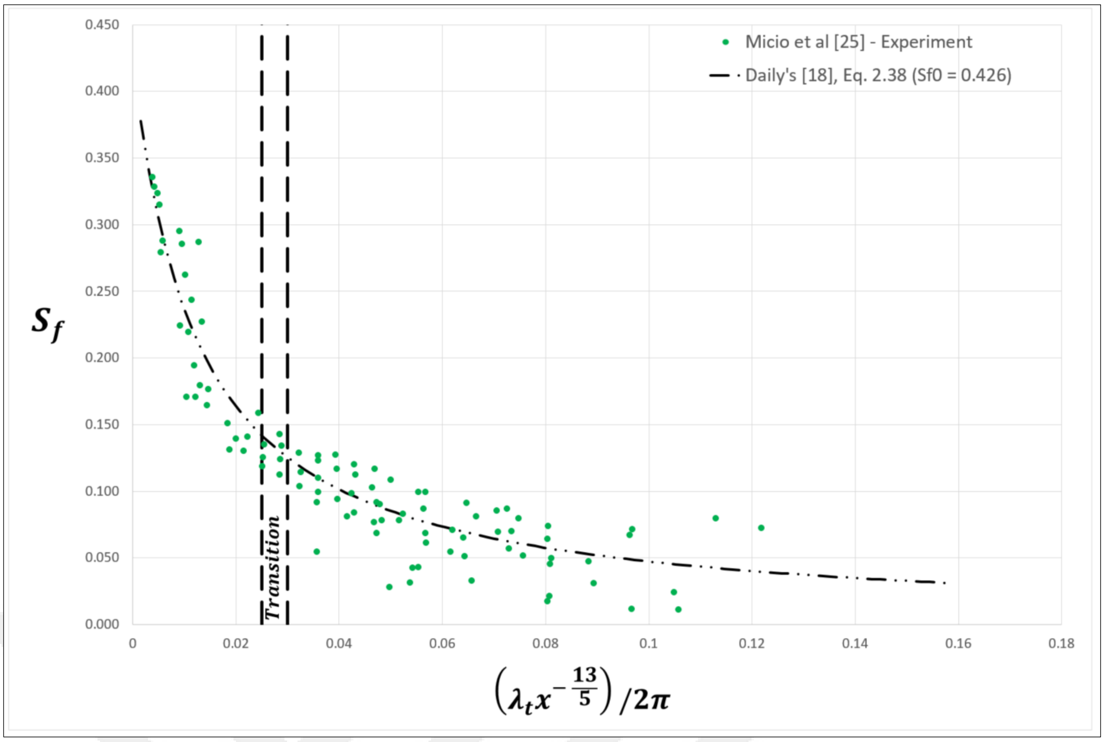

Figure 2.24: Comparison of Daily's correlation with experimental data.

There can be numerous case of gap ratios and flow rates but if we think overall, Daily's approach giving acceptable approximations with a proper ${S_f}_0$ estimation over whole range of through flow rates; and it is definitely predicting the trend.

It is important to remember that turbulent parameter, λ_t as well as superposed flow coefficient, C_w are defined according to full disks which meaning that these parameter are derived to investigate and understand the flow conditions inside the whole cavity. There will be only one turbulent parameter for a specific Reynolds number and superposed flow rate which meaning that to use the local turbulent parameter approach, one need a specific radius ratio, x, as Daily's showed in **Figure 2.22**. Otherwise, radius ratio will be decreasing towards the outer periphery and results in infinite local turbulent parameter definition throughout the radius but only corresponding to one specific core rotation swirl. This is the misunderstanding behind this approach together with the reason why it evolved differently from its originated derivation purpose. Normally, investigations should be made for a specific radius ratio and for different superposed flow rates to see that how core rotation swirls are decreasing with increased flow rates.

In real case (in gas turbines), however, cavities includes multiple axisymmetric surfaces, which may be rotating, co-rotating or stationary. Each disk surface may comprise of radial, conical and horizontal surfaces and may have protrusions like bolts that tend to break the overall symmetry of the cavity about its rotation axis. Additionally, the cavity may have multiple inlets and outflows at different radial location with different swirl, temperature and pressure conditions. Therefore, we need to divide cavity into control volumes and calculate swirl distribution with torque–angular momentum conservation for each control volume element, which will be explained later as our study method in cavities.

2.4. Windage Heating

The term windage heating can be defined as the viscous friction heating which results from the work transfer provided by shear forces in the presence of velocity gradient between fluid and the rotating disk in contact. Thus, windage is the rotor input to the system and cannot happen through stationary surfaces. However, stationary surfaces will contribute to windage indirectly through velocity gradients since fluid will be slowed down by negative torques taken from stationary walls (Sultanian **[1])**.

Newman **[16]**, for the first time referring its name as windage (as far as I found out), defining it as the energy required to rotate the disk. It is indeed a perfect explanation because if one brings the rotating disk from vacuum to fluid medium, the power required to maintain the disk rotation against this fluid resistance, is the windage power.

$$\dot{W}_{windage} = M_{rotor} * \omega \tag{2.45}$$

Where for full disks,

$$M_{rotor} = \frac{1}{2} C_m \rho \omega^2 R^5 \tag{2.46}$$

Thus,

$$\dot{W}_{windage} = \frac{1}{2} C_m \rho \omega^3 R^5 \tag{2.47}$$

Moment coefficient correlations derived for "free disks" by many authors can be used to calculate windage power directly with equation **(**2.47**)**, which will represent the maximum power required (compared to enclosed cavities) to rotate the one side of the disk. If there is a symmetry and similar flow conditions on the other side of the disk, simply multiplying these numbers by two will gave the total windage loss of the disk by neglecting the loss coming from the tip of the disk.

Figure 2.25 showing the windage power difference coming from power-law approximations as well as with Dorfman and Bayley's correlations calculated from equation **(**2.47**)** for our one side of the disk 0.45 m in diameter rotating in air at one atmosphere pressure and room temperature. Differences are maximum 12.5 percent at 10 million rotational Reynolds Number.

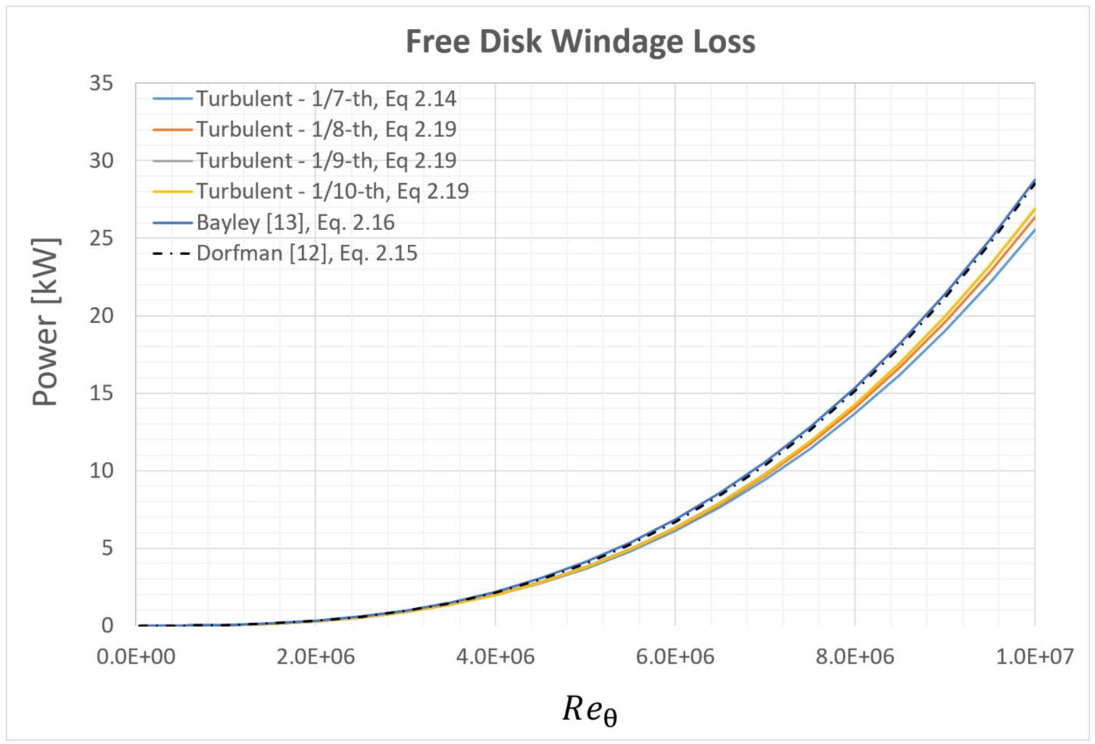

Figure 2.25: Calculated "Free disk" windage losses for our test rig case (for one side of the disk).

Even today, windage heating is not clearly defined in the literature. Some authors confuse it with viscous dissipation while others think windage heating can result from stationary walls. Only rotating surfaces do work on the fluid in contact because of the basic fact that a force only does work if there is a displacement in the direction of the force. Therefore, only rotating surfaces do work through tangential shear forces in the direction of the rotation and results in windage not the stator surfaces although they generate stator torque and participate indirectly to windage through torque and angular momentum balance.

If we think of a fluid flow in an adiabatic stationary pipe. The fluid total temperature should be conserved from inlet to exit of the pipe no matter that we have wall friction or shock anywhere inside. It is because, in spite of the wall shear stress, the work done on the fluid flow will be zero because the wall velocity is zero. It also makes sense through the second law of thermodynamics, if there is no work or heat transfer (adiabatic); total enthalpy of the system should be conserved. Therefore, friction cannot give energy to the system without any movement or displacement in the direction of the shear.

Lyman **[26]**, while trying to clarify the conservation of Rothalpy, transforming the total enthalpy equation for a viscous, compressible fluid with heat conduction which is firstly derived by Liepmann and Roshko **[27]**, from a fixed system of cylindrical coordinates to a system rotating about the z axis by means of prime relations

$$\rho \frac{Dh_0}{Dt} = \frac{\partial p}{\partial t'} + \omega r F_\theta + \nabla \cdot \left(\overleftrightarrow{\tau} \cdot \overrightarrow{W}\right) + \rho \vec{f} \cdot \overrightarrow{W} - \nabla \vec{q} \tag{2.48}$$

Where

$$F_\theta \equiv -\frac{1}{r}\frac{\partial p}{\partial \theta} + (\nabla \cdot \overleftrightarrow{\tau})_\theta + \rho f_\theta \tag{2.49}$$

Here $\frac{D}{Dt}$ is the substantial derivative operator in either the absolute or relative frame, $\vec{q}$ is the heat flux vector, and F_θ is the tangential component of the net force per unit volume. In addition, ρ is the density, θ is the tangential coordinate but as a subscript it refers to the tangential component of a vector, p is the static pressure, ω is the angular velocity, r is the radius, $\overrightarrow{W}$ is the relative velocity vector, $\overleftrightarrow{\tau}$ is the shear stress tensor, and $\vec{f}$ is a general body per unit mass force vector. The first term that changes the total enthalpy appears as the pressure fluctuations due to flow unsteadiness in the rotating frame. Lyman **[26]** explaining the second term as the power per unit volume that must be supplied to fluid, just to rotate a fluid particle with angular velocity ω against the tangential pressure, friction, and body forces acting on it. The third term is the rate at which work is done on the relative motion of the fluid in the rotating frame by viscous stresses. The fourth term on the right is the rate at which work is done on the relative motion by the body force and the fifth the net rate of heat addition.

If we adapt the equation (2.48) for a rotor-stator cavity with superposed radial outflow, now we have a fluid that is rotating at some portion of the disk angular velocity, ω with core swirl factor S_f while makes its way radially outward from inlet to the exit. Assuming steady state $\left(\frac{\partial}{\partial t'} = 0\right)$, adiabatic $(\vec{q} = 0)$, axisymmetric flow $\left(\frac{\partial}{\partial \theta} = 0\right)$ and neglecting body forces $\left(\vec{f} = 0\right)$; equation reduces to,

$$\rho \frac{Dh_0}{Dt} = \nabla \cdot \left(\overleftrightarrow{\tau} \cdot \overrightarrow{W}\right) \tag{2.50}$$

By splitting the term at the right hand side,

$$\nabla \cdot \left(\overleftrightarrow{\tau} \cdot \overrightarrow{W}\right) = (\nabla \cdot \overleftrightarrow{\tau}) \cdot \overrightarrow{W} + r : \nabla \overrightarrow{W} \tag{2.51}$$

Which yields to,

$$\rho \frac{Dh_0}{Dt} = (\nabla \cdot \overleftrightarrow{\tau}) \cdot \overrightarrow{W} + r : \nabla \overrightarrow{W} \tag{2.52}$$

The first term here is the rate at which the net viscous force per unit volume does work on the relative flow while the second term is the rate of viscous dissipation, $\Phi = r : \nabla \overrightarrow{W}$ which is never negative. In the rotating disk boundary layer, fluid will have both radial and tangential velocity gradient with the disk. Due to this gradient, the rotating disk continuously does work to fluid through tangential shear which is in the direction of rotation but the radial shear between would only results in dissipation. If we re-arrange the relative velocity vector terms,

$$\rho \frac{Dh_0}{Dt} = (\nabla \cdot \overleftrightarrow{\tau})_\theta r S_f \omega + \Phi \tag{2.53}$$

Which is equal to

$$\rho \frac{Dh_0}{Dt} = \Gamma'_\theta \omega + \Phi \tag{2.54}$$

Γ'_{θ} is the tangential torque per unit volume that rotor applies to fluid and multiplying with angular velocity giving us windage power per unit volume as the first term and viscous dissipation per unit volume as the second. Theory, also showing the windage heating and viscous dissipation separately. Since viscous dissipation always a positive term, it is also known as entropy generation term. On the other hand, windage, however, has a direction and can either be from disk to fluid or from fluid to disk, depending on which one is rotating faster so that doing the work to one another.

Moreover, Sultanian **[1]** underlying in his book the fact that viscous dissipation is changing the form of the energy through irreversible work transfer, which results in viscosity driven transfer of external flow energy into the internal energy and adding that it should not change the total enthalpy of fluid under adiabatic conditions. However, yet it appears in substantial derivative of the total enthalpy equation. Why? Readers are encouraged to find out.

In summary, windage power can either be measured as a shaft power since it is generally associated with the loss in rotor power or heat rise of the fluid passing through and exposing to windage. In other words, fluid resisting to rotating disk through viscous related friction forces and the power that is referred as frictional loss turn into the fluid as a total temperature increase. Simply, one using some portion of the power generated by turbines to heat the gas in cavities; or in the reverse scenario case with negative windage, fluid doing work so that losing enthalpy cooling itself and powering the shaft. Therefore, it is very important phenomenon to internal air system designers.

Overall, coming to the calculation part, one can calculate the windage power for one side of a disk with radius R as follows,

$$\dot{W}_{windage} = \Gamma_{rotor} * \omega \tag{2.55}$$

$$\Gamma_{rotor} = \int_{0}^{R} \tau_{\theta} r dA \tag{2.56}$$

Where $dA = 2\pi r dr$

$$\Gamma_{rotor} = \int_{0}^{R} \tau_\theta r(2\pi r dr) = 2\pi \int_{0}^{R} \tau_\theta r^2 dr \tag{2.57}$$

Where $\tau_\theta = \frac{1}{2} C_f \rho \, (\omega r)^2$ for simplicity at the beginning, later on we will write it according to relative velocities.

$$\Gamma_{rotor} = \int_{0}^{R} C_f \rho \, \omega^2 \pi r^4 dr \tag{2.58}$$

Assuming constant skin friction throughout the radius which will be discussed soon,

$$\Gamma_{rotor} = C_f \rho \omega^2 \pi \int_{0}^{R} r^4 dr \tag{2.59}$$

$$\Gamma_{rotor} = \frac{C_f \rho \omega^2 \pi R^5}{5} \tag{2.60}$$

If we write in terms of moment coefficient, C_m,

$$\Gamma_{rotor} = \frac{C_f \rho \omega^2 \pi R^5}{5} = \frac{1}{2} C_m \rho \omega^2 R^5 \tag{2.61}$$

Giving the relation between skin friction coefficient and moment coefficient as

$$C_m = \frac{2\pi}{5} C_f \tag{2.62}$$

Moments in test rigs generally measured from the consumed power of drivers (electric motors) with a deduction for losses (torque losses related to the transmission system, losses of bearings etc.) or directly with strain gages in a more accurate way as Daily and Nece **[19]** did. So these moments actually are the resistance of the fluid against rotating disks which meaning the power required to turn the whole disk at a specific rpm’s and also meaning the mechanical energy ,which is windage, supplied to the flow in unit time in a case where disk rotating faster than the fluid. Therefore, moments taken from test data’s non-dimensionalized by moment coefficient since they are obtained for whole and both side of the disks in rigs. Although one can simply use this relation to obtain skin friction coefficients for from moment coefficients, we are after on skin friction coefficients, C_f for partial disk torque calculations.

Based on the actual gas turbine test experience and with the experimental data of Daily and Nece **[19]**; Haaser, Jack and McGreehan **[28]** proposed the empirical correlation derived for constant tangential shear stress over the disk for the skin friction coefficient on one side of the rotor as

$$C_{f_R} = 0.042\,(1 - Sf)^{1.35} {Re_\theta}'^{\,-0.2} \tag{2.63}$$

In addition, that on one side of the stator disk as

$$C_{f_S} = 0.063\,S_f^{1.87} {Re_\theta}'^{\,-0.2} \tag{2.64}$$

Where the full disk Reynolds number ($Re_\theta = \rho\omega R^2/\mu$) has been modified to,

$$Re'_\theta = \frac{\rho\omega R(R - R_i)}{\mu} \tag{2.65}$$

However, Sultanian **[1]** stating that using these C_f values for partial disk torques yields greater torque values than full disks for $R_i/R < 0.5$, which is physically unacceptable. To eliminate this Sultanian **[1]** making the assumption that, instead of a constant tangential shear stress over the disk, as assumed in Haaser, Jack and McGreehan **[28]**, skin friction coefficient of the tangential stress is constant. Moreover, he deducting the new shear constants from the same test data but using fluid tangential velocity relative to the surface to compute the dynamic pressure. (See Sultanian **[1]**) Then coefficients re-casted as follows:

$$C_{f_R} = 0.070\,(1 - Sf)^{-0.65} {Re_\theta}^{-0.2} \tag{2.66}$$

For stator

$$C_{f_S} = 0.105\,S_f^{-0.13} {Re_\theta}^{-0.2} \tag{2.67}$$

Where $Re_\theta = \rho\omega R^2/\mu$ and $\tau_\theta = \frac{1}{2} C_f \rho [(1 - S_f)(\omega r)]^2$

Then, torque partial disk with a constant skin friction assumption using fluid relative velocity, equation becomes,

$$\Gamma_{rotor} = C_{f_R}\rho\left(1-S_f\right)^2\omega^2\pi\int_{R_i}^{R} r^4 dr \tag{2.68}$$

$$\Gamma_{rotor} = C_{f_R}\rho\left(1-S_f\right)^2\omega^2\pi\left(\frac{R^5}{5}-\frac{R_i^5}{5}\right) \tag{2.69}$$

Substituting $C_{f_R} = 0.070\ (1-Sf)^{-0.65}Re_\theta{}^{-0.2}$

Rotor torque become,

$$\Gamma_{rotor} = 0.044\rho\left(1-S_f\right)^{1.35}\omega^2\left(R^5-R_i^5\right)Re_\theta^{-0.2} \tag{2.70}$$

Then, windage power equals to

$$\dot{W}_{windage} = \Gamma_{rotor} * \omega \tag{2.71}$$

$$\dot{W}_{windage} = 0.044\rho\left(1-S_f\right)^{1.35}\omega^3\left(R^5-R_i^5\right)Re_\theta^{-0.2} \tag{2.72}$$

If we also expand Rotational Reynolds number,

$$\dot{W}_{windage} = 0.044\rho^{0.8}\left(1-S_f\right)^{1.35}\omega^{2.8}\mu^{0.2}R^{4.6}\left(1-\frac{R_i^5}{R^5}\right) \tag{2.73}$$

As we can see, the radius of the disk will cause the windage most as varies with $R^{4.6}$, after that, angular velocity of the disk that varies with third power of it, $\omega^{2.8}$. Then, tangential velocity gradient between effecting as the third most with $\left(1-S_f\right)^{1.35}$. Other variables in order are the density of the fluid that is exposing to windage and of course viscosity of the fluid. Equation (2.73) can also be used for scaling of the windage power from design point to off-design conditions simply by changing fluid properties and the angular velocity since swirl ratio would be almost constant and not change from design to off-design conditions **[29]** and the cavity is the same cavity.

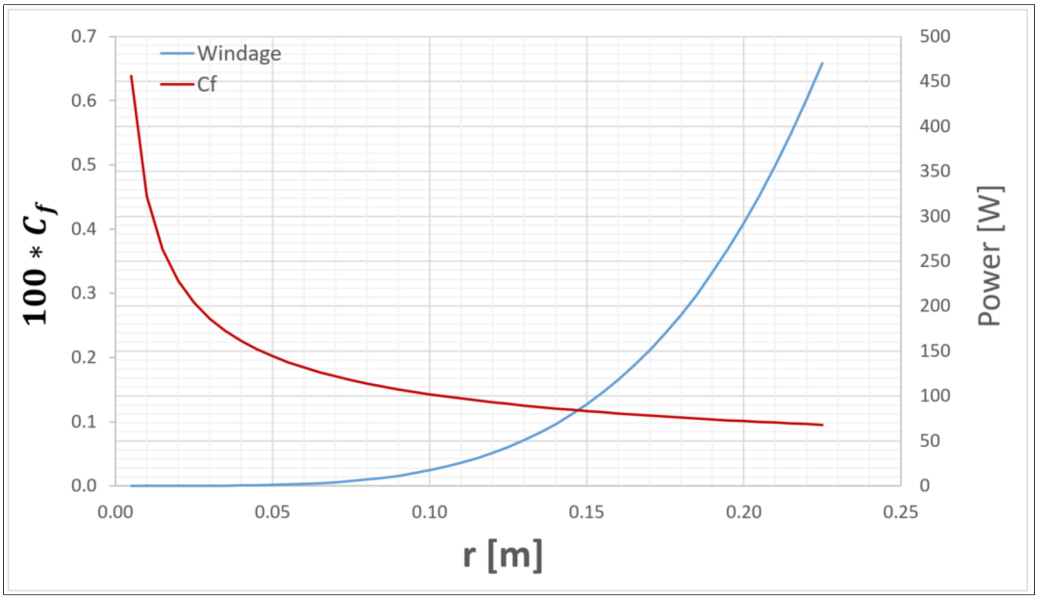

Figure 2.26: Variation of skin friction coefficient and windage power from center to the outer periphery of the disk.

Figure 2.26 showing how skin friction coefficients are changing from center to tip of the disk at Reynolds number of $Re_\theta = 5 \times 10^6$, using coefficients from Blasius's law of skin friction in pipe flow according to local Rotational Reynolds numbers for our 450 mm disk rotating in air at 1 atmosphere pressure and room temperature $\left(C_f = 0.045(x^2 Re_\theta)^{-0.25}\right)$. Also, "free disk" windage powers $\left(S_f = 0\right)$ at corresponding volumes (with 5 mm radius increment) are calculated from equation **(**2.72**)**. One can see that till the half of the disk there is nearly no windage at all and as we go further in radius skin friction coefficients becoming flat as Reynolds going higher to tip of the disk where the most of the windage coming from. Therefore, making constant C_f assumptions also seems reasonable by this point of view.

2.5. One-Dimensional Flow Modeling Through R-S Cavity

2.5.1. Conservation of Angular Momentum

1-D adiabatic steady state flow modeling in a simplified rotor-stator cavity shown in **Figure 2.27**. Same methodology is applied as in Ref. **[30**, **31]**. With $\dot{m}_{in} = \dot{m}_{out} = \dot{m}$, the steady mass conservation equation is satisfied. Since the system is adiabatic, the change in total temperature will occur entirely through the work transfer from the rotor as mentioned before. The stator torque only participates in the torque-angular momentum balance but not directly in the mechanical energy transfer with the fluid. To capture accurate variations of flow properties in the cavity, we divide it into a number of control volumes, n. For a radial outward flow, control volume 1 starting from radius r_i and exiting the outlet surface by $i+1$, we write the following angular momentum equation:

$$\Gamma_{rotor} - \Gamma_{stator} = \dot{m}\left(r_{i+1}V_{\theta_{i+1}} - r_i V_{\theta_i}\right) = \dot{m}\left(r_{i+1}^2 S_{f_{i+1}} - r_i^2 S_{f_i}\right)\omega \tag{2.74}$$

Where

$$\Gamma_{R_1} = 0.044\rho\left(1 - S_{f_1}\right)^{1.35}\omega^2\left(r_{i+1}^5 - r_i^5\right) Re_\theta^{-0.2} \tag{2.75}$$

$$\Gamma_{S_1} = 0.066\rho\, S_{f_1}^{1.87}\omega^2\left(r_{i+1}^5 - r_i^5\right) Re_\theta^{-0.2} \tag{2.76}$$

Where $Re_\theta = \rho\omega R^2/\mu$

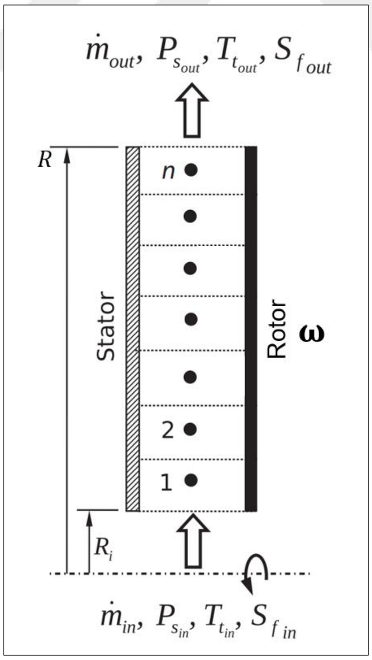

Figure 2.27: Rotor-stator cavity with through-flow **[1]**.

Making the assumption exit swirl ratio of the cavity equals to core swirl ratio of the cavity, $S_{f_{i+1}} = S_{f_1}$ where $S_{f_i} = S_{f_{in}}$

$$\left[0.044\rho\left(1 - S_{f_1}\right)^{1.35} - 0.066\rho\, {S_{f_1}}^{1.87}\right] \omega^2\left(r_{i+1}^5 - r_i^5\right) Re_\theta^{-0.2} = \dot{m}\left(r_{i+1}^2 S_{f_1} - r_i^2 S_{f_{in}}\right) \qquad (2.77)$$

Now S_{f_1} can be calculated iteratively which will be our inlet swirl boundary condition for the next cavity number 2. Pay attention to that, in this approach, we are making the assumption that exit swirl at the outlet surface, $i + 1$ equal to the core swirl ratio of the cavity itself. This assumption can either be used for whole cavity or dividing a cavity into multiple control volumes as we doing here; but undoubtedly using it for whole cavity where a swirls changing too much with changing radius would reduce the accuracy of calculations or can be true also in case of completely forced vortex with constant swirl from center to rim of the cavity. This will be discussed later with numbers in the theoretical approach part.

Since flow is adiabatic, through the first law of thermodynamics, the change in fluid total temperature will only occur through work transfer as a result of windage in the control volume, which can be obtained using the equation (2.78).

$$T_{t_{i+1}} - T_{t_i} = \frac{\dot{W}_{windage}}{\dot{m}c_p} = \frac{\Gamma_{R_1}\omega}{\dot{m}c_p} \qquad (2.78)$$

2.5.2. Axial Thrust on a Disk

The force on an elemental area δA, is δF

Where

$$\delta F = P_s \delta A = P_s 2\pi r \delta r \qquad (2.79)$$

If the inner radius static pressure P_{s_i} known such as radial outward flow case, then for a disk of inner radius R_i and the outer radius R, assuming incompressible flow, force equals to

$$F = \int_{R_i}^{R} \left(P_{s_i} + \frac{1}{2}\rho {S_f}^2 \omega^2 \left(r^{\,2} - R_i^2\right)\right) 2\pi r \,\mathrm{d}r \qquad (2.80)$$

$$F = \int_{R_i}^{R} \left(P_{s_i} 2\pi r + \pi\rho {S_f}^2 \omega^2 r^3 - \pi\rho {S_f}^2 \omega^2 {R_i}^2 r\right) \mathrm{d}r \tag{2.81}$$

$$F = \left[P_{s_i} \pi r^2 + \frac{\pi\rho {S_f}^2 \omega^2 r^4}{4} - \frac{\pi\rho {S_f}^2 \omega^2 {R_i}^2 r^2}{2}\right]_{R_i}^{R} \tag{2.82}$$

Then, axial thrust is

$$F_{thrust} = P_{s_{in}} \pi (R^2 - {R_i}^2) + \frac{\pi}{4} \rho {S_f}^2 \omega^2 (R^4 - {R_i}^4) - \frac{\pi}{2} \rho {S_f}^2 \omega^2 {R_i}^2 (R^2 - {R_i}^2) \tag{2.83}$$

If the outer radius static pressure $P_{s_{out}}$ known such as radial inward flow, then for a disk of inner radius R_i and the outer radius R, assuming incompressible flow, we can express the force that air exerting on disk as

$$F = \int_{R_i}^{R} \left(P_{s_o} - \frac{1}{2} \rho {S_f}^2 \omega^2 (R^2 - r^2)\right) 2\pi r \, \mathrm{d}r \tag{2.84}$$

$$F = \int_{R_i}^{R} \left(P_{s_o} 2\pi r - \pi\rho {S_f}^2 \omega^2 R^2 r + \pi\rho {S_f}^2 \omega^2 r^3\right) \mathrm{d}r \tag{2.85}$$

$$F = \left[P_{s_o} \pi r^2 - \frac{\pi\rho {S_f}^2 \omega^2 R^2 r^2}{2} + \frac{\pi\rho {S_f}^2 \omega^2 r^4}{4}\right]_{R_i}^{R} \tag{2.86}$$

Then, axial load become,

$$F_{thrust} = P_{s_{out}} \pi (R^2 - {R_i}^2) - \frac{\pi}{2} \rho {S_f}^2 \omega^2 R^2 (R^2 - {R_i}^2) + \frac{\pi}{4} \rho {S_f}^2 \omega^2 (R^4 - {R_i}^4) \tag{2.87}$$

2.5.3. Torque Calculations on Arbitrary Surfaces

A cavity can have a rotor or stator disk with conical and cylindrical surfaces. For the conical part of a rotating disk, we will again be using shear stress coefficient correlation given by equation (2.88), and if it's a stator disk, we use equation (2.89) to calculate its skin friction coefficient.

$$C_{f_{R_{cone/disk}}} = 0.070\,(1 - Sf)^{-0.65} {Re_{\theta}}^{-0.2} \tag{2.88}$$

$$C_{f_{S_{cone/disk}}} = 0.105\, S_f^{-0.13} {Re_{\theta}}^{-0.2} \tag{2.89}$$

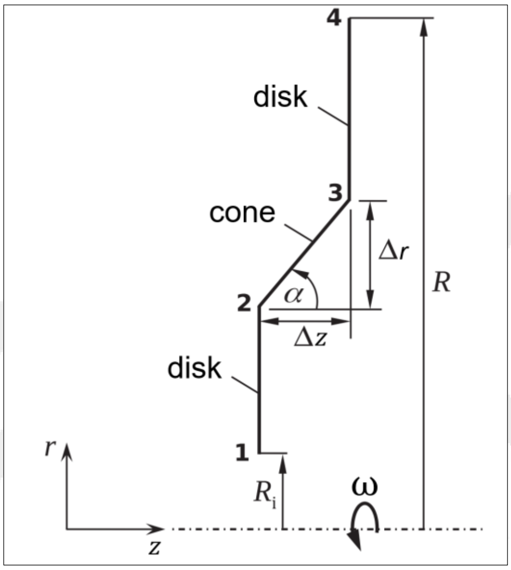

Figure 2.28: Disk with a conical surface **[1]**.

Now, area becomes,

$$A_{cone} = \frac{2\pi}{\sin\alpha} \int_{r_2}^{r_3} r^4 dr \tag{2.90}$$

Where

$$\sin\alpha = \sin(\tan^{-1}(\Delta r/\Delta z)) \tag{2.91}$$

For the conical surface part of the rotor disk shown in **Figure 2.28**, we calculate its torque as

$$\Gamma_{R_{cone}} = C_{f_R} \frac{1}{2} \rho \left(1 - S_f\right)^2 \omega^2 \frac{2\pi}{\sin\alpha} \int_{r_2}^{r_3} r^4 dr \tag{2.92}$$

Which is equal to,

$$\Gamma_{R_{cone}} = \frac{0.044\rho\left(1 - S_f\right)^{1.35}\omega^2(r_3^5 - r_2^5)\, Re_\theta^{-0.2}}{\sin\alpha} \tag{2.93}$$

For the corresponding conical surface part of a stator disk

$$\Gamma_{S_{cone}} = \frac{0.066\rho\, {S_f}^{1.87}\omega^2(r_3^5 - r_2^5)\, Re_\theta^{-0.2}}{\sin\alpha} \tag{2.94}$$

Where both $Re_\theta = \rho\omega R^2/\mu$

For the cylindrical rotor surface shown in **Figure 2.29**, we take the shear stress coefficient correlation proposed by Haaser, Jack, and McGreegan **[28]**.

$$C_{f_R} = 0.042\ (1 - Sf)^{-0.65}{Re_h}^{-0.2} \tag{2.95}$$

Where

$$Re_h = \frac{\rho\omega R_h^2}{\mu} \tag{2.96}$$

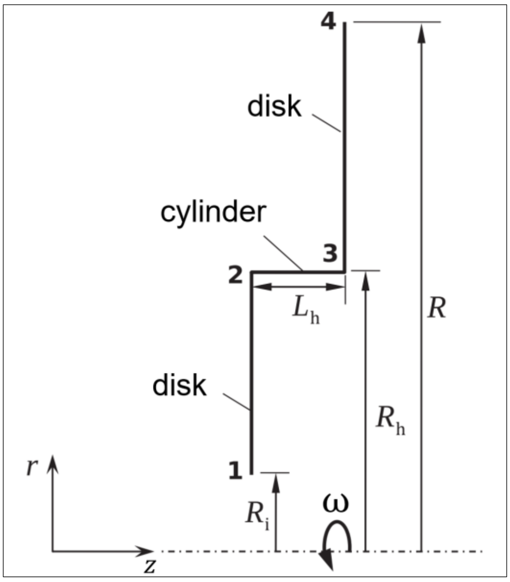

Figure 2.29: Disk with a cylindrical surface **[1]**.

For cylindrical area shown in **Figure 2.29**,

$$A_{cylinder} = 2\pi R_h^4 \int_{z_2}^{z_3} dz \tag{2.97}$$

Then, the torque of the cylindrical surface part of the rotor can be calculated as follows:

$$\Gamma_{R_{cylinder}} = C_{f_R} \frac{1}{2} \rho \left(1 - S_f\right)^2 \omega^2 2\pi R_h^4 \int_{z_2}^{z_3} dz \tag{2.98}$$

Which is equal to,

$$\Gamma_{R_{cylinder}} = 0.132 \rho \left(1 - S_f\right)^{1.35} \omega^2 R_h^4 L_h Re_h^{-0.2} \tag{2.99}$$

For the corresponding conical surface part of a stator disk, extending the skin frictions proposed by Haaser, Jack, and McGreegan **[28]** to the generalized form,

$$C_{f_S} = 0.063\, S_f^{-0.13} {Re_h}^{-0.2} \tag{2.100}$$

Which yields the corresponding torque as

$$\Gamma_{S_{cylinder}} = 0.198\, \rho\, S_f^{1.87} \omega^2 R_h^4 L_h Re_h^{-0.2} \tag{2.101}$$

Where $Re_h = \frac{\rho \omega R_h^2}{\mu}$

2.5.4. Static Pressure Distribution inside the Cavity

Knowing the core swirl of the cavity, S_f, static pressure increase/decrease from inlet to exit can be obtained using the radial equilibrium equation for steady and axisymmetric flow,

$$\frac{\partial p}{\partial r} = \rho \frac{V_\theta^2}{r} - \rho V_r \frac{\partial V_r}{\partial r} - \rho V_z \frac{\partial V_r}{\partial r} + \mu \left(\nabla^2 V_r - \frac{V_r}{r^2} \right) \tag{2.102}$$

Generally, cavity gap ratios are big enough to allow core rotation with separate boundary layers at rotor and stator. In this kind of flow structures, core rotation will be the one controlling the radial pressure gradient. If we remember the velocity profiles of the Batchelor type of flow structures (see **Figure 2.16**), in this core region, we have a vortex that forced by rotating disk, rotating at some portion of the disk angular velocity, ω with almost zero radial and axial velocity. Since the viscous terms can be neglected outside the boundary layers, equation **(**2.102**)** reduces to

$$\frac{\partial p}{\partial r} = \rho\frac{V_\theta^2}{r} \tag{2.103}$$

Or

$$\frac{\partial p}{\partial r} = \rho\omega_\theta^2 r \tag{2.104}$$

Where $S_f = V_\theta/\omega r = \omega_\theta/\omega$

If the flow can assumed to be incompressible, integration will yield

$$\int_{r_i}^{r_{i+1}} dp = \int_{r_i}^{r_{i+1}} \rho\omega_\theta^2 r dr \tag{2.105}$$

$$P_{s_{i+1}} - P_{s_i} = \rho\omega_\theta^2\left(\frac{r_{i+1}^2}{2} - \frac{r_i^2}{2}\right) \tag{2.106}$$

$$P_{s_{i+1}} - P_{s_i} = \frac{1}{2}\rho\, {S_f}^2\omega^2\,(r_{i+1}^2 - r_i^2) \tag{2.107}$$

Using an average value of density,

$$\bar{\rho} = \frac{(\rho_{i+1} + \rho_i)}{2} \tag{2.108}$$

For control volume 1 exit static pressure become

$$P_{s_{i+1}} = P_{s_i} + \frac{1}{2}\bar{\rho}\, S_{f_1}^2\omega^2\,(r_{i+1}^2 - r_i^2) \tag{2.109}$$

2.6. Surface Roughness

Surface roughness is a significant quantity for many engineering concerns such as friction (as the most interested topic for us), contact deformation, contact tightness etc. and for this reason; it has been the subject of many theoretical and experimental investigations for decades.

Throughout these years, researches have introduced many roughness parameters to measure this relative smoothness of the surface's profile in two-dimensional scale and 2D profile analysis has been the main design practice for more than half a century in science and engineering. However, the real surface geometry is actually so complicated at the microscale that a finite number of parameters cannot provide a full description. In recent years, therefore, three-dimensional surface analysis are more in demand for surface evaluation.

2.6.1. Surface Roughness Definition

In the scope of this study, only the parameters that is mostly used in literature will be defined and used throughout the analysis.

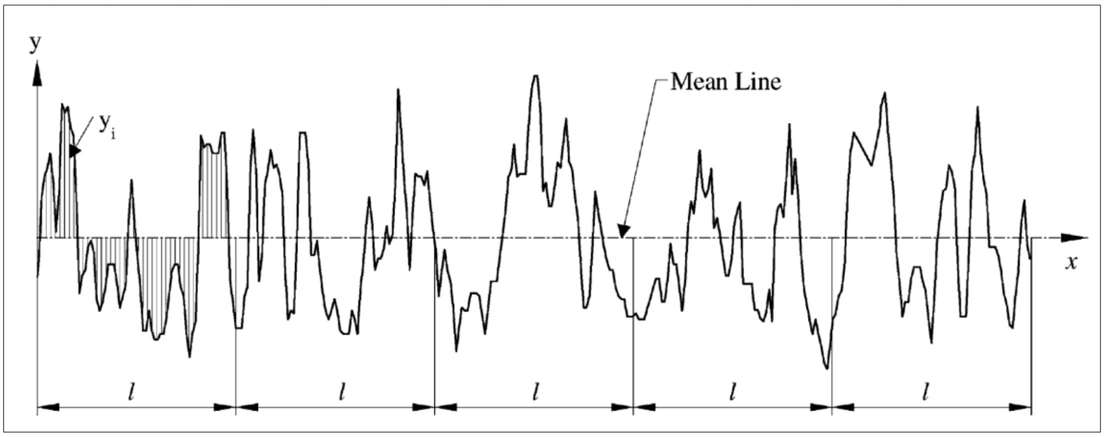

Figure 2.30: Definition of the arithmetic average height parameter **[32]**.

The arithmetic average height parameter, R_a is the most commonly used roughness parameter. It is defined as the average absolute deviation of surface peaks and valleys from the mean line over sampling length as shown in **Figure 2.30**. The mathematical definition and the digital implementation of R_a are, respectively, as follows:

$$R_a = \frac{1}{l}\int_0^l |y(x)|\, dx \tag{2.110}$$

$$R_a = \frac{1}{n}\sum_{i=1}^{n} |y_i| \tag{2.111}$$

RMS (Root mean square) roughness, R_q , represents the standard deviation of the distribution of surface heights; hence, it is an important parameter to evaluate the surface roughness by statistical methods. This parameter is more sensitive than average height parameter, R_a to large deviation from the mean line. The mathematical definition and the digital implementation of R_q are, respectively,

$$R_q = \sqrt{\frac{1}{l}\int_0^l y(x)^2\, dx} \tag{2.112}$$

$$R_q = \sqrt{\frac{1}{n}\sum_{i=1}^{n} {y_i}^2} \tag{2.113}$$

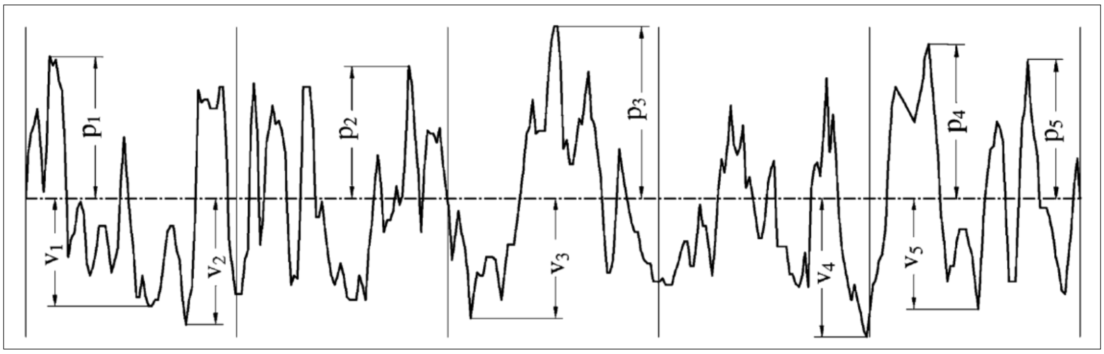

Figure 2.31: Definition of the ten-point height parameter **[32]**.

The last one is the, R_z which is known as ten-point height parameter. This parameter is more sensitive to occasional high peaks or deep valleys than, R_a. It is defined by two method according to the definition system. The International ISO system defines this parameter as the difference in height between the average of the five highest peaks and the five lowest valleys along the assessment length of the profile.

The German DIN system defines R_z as the average of the summation of the five highest peaks and the five lowest valleys along the assessment length of the profile. **Figure 2.31** above showing the definition of the ten-point height parameter. The mathematical definitions of the two types of R_z are,

$$R_{z(\mathrm{ISO})} = \frac{1}{n}\left(\sum_{i=1}^{n} p_i - \sum_{i=1}^{n} v_i\right) \tag{2.114}$$

$$R_{z(\mathrm{DIN})} = \frac{1}{2n}\left(\sum_{i=1}^{n} p_i + \sum_{i=1}^{n} v_i\right) \tag{2.115}$$

2.6.2. Surface Roughness Modelling

Nikuradse J. **[33]** carried out extensive measurements on rough pipes that covered on the inside with sand of a specific grain size glued on to the wall. Schlichting **[4]** then used Nikuradse's data to correlate different types of non-sand roughness (such as rivets and protuberances). In doing so, Schlichting **[4]** introduced the term k_s, the equivalent sandgrain height or the roughness height, to define a roughness feature and spacing that has the equivalent effect on skin friction losses as a uniform layer of actual sandgrains of diameter k_s. Though Schlichting's quantitative results have since been questioned by Coleman et al. **[34]** his equivalent roughness method has gained universal acceptance.

In roughness work related to gas turbines, a variety of correlations have been utilized to relate measurable surface roughness parameters, R_a, R_q or R_z to equivalent sandgrain roughness k_s in accordance with the Schlichting model as follow:

$$k_s = C * R_a \tag{2.116}$$

In equation **(**2.116) both k_s and R_a have the same units of micrometers or microns(μm) and C is the constant. The troublesome part on finding the effective roughness k_s is to determine the constant C. Since it will be depended on the flow structure as well as on the flow characteristics through Reynolds Number; meaning it will be different for a flow going through a turbine nozzle guide vanes and for a flow with a core rotation in a rotor-stator cavity (for example impeller back cavity flow) even though they have same surface quality on vane or disk.

In addition, since the roughness related losses will be related to specific length of the rough surface so that the most convenient way will be to represent roughness relative to the blade chord, c as $k_s/\ c$ or to disk radius, R as $k_s/\ R$ respectively when total loss or total torques derived.

Table 2.4 contains literature survey about roughness in gas turbines given by Bons **[37]**. As one can see from the table, there is a wide variety of correlations ranging up from 1 to 10 for specific cases.

Table 2.4: Roughness relations for k_s determination of gas turbines **[37]**.

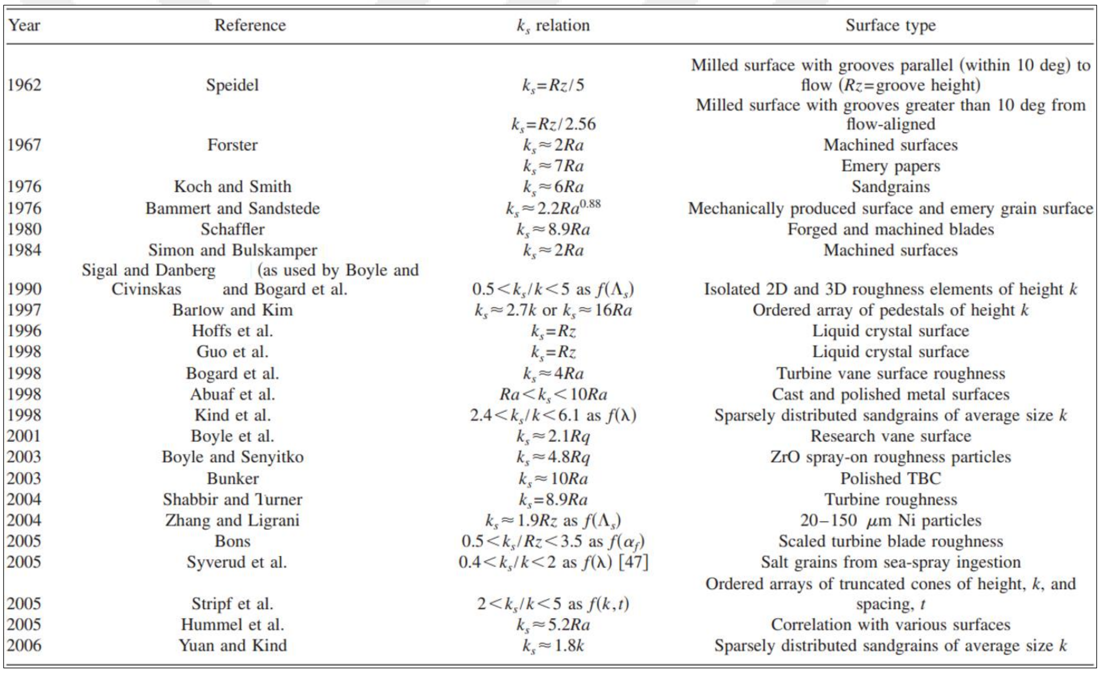

Year	Reference	k_s relation	Surface type
1962	Speidel	$k_s=Rz/5$	Milled surface with grooves parallel (within 10 deg) to flow (Rz=groove height)
		$k_s=Rz/2.56$	Milled surface with grooves greater than 10 deg from flow-aligned
1967	Forster	$k_s\approx 2Ra$	Machined surfaces
		$k_s\approx 7Ra$	Emery papers
1976	Koch and Smith	$k_s\approx 6Ra$	Sandgrains
1976	Bammert and Sandstede	$k_s\approx 2.2Ra^{0.88}$	Mechanically produced surface and emery grain surface
1980	Schaffler	$k_s\approx 8.9Ra$	Forged and machined blades
1984	Simon and Bulskamper	$k_s\approx 2Ra$	Machined surfaces
1990	Sigal and Danberg (as used by Boyle and Civinskas and Bogard et al.	$0.5<k_s/k<5$ as $f(\Lambda_s)$	Isolated 2D and 3D roughness elements of height k
1997	Barlow and Kim	$k_s\approx 2.7k$ or $k_s\approx 16Ra$	Ordered array of pedestals of height k
1996	Hoffs et al.	$k_s=Rz$	Liquid crystal surface
1998	Guo et al.	$k_s=Rz$	Liquid crystal surface
1998	Bogard et al.	$k_s\approx 4Ra$	Turbine vane surface roughness
1998	Abuaf et al.	$Ra<k_s<10Ra$	Cast and polished metal surfaces
1998	Kind et al.	$2.4<k_s/k<6.1$ as $f(\lambda)$	Sparsely distributed sandgrains of average size k
2001	Boyle et al.	$k_s\approx 2.1Rq$	Research vane surface
2003	Boyle and Senyitko	$k_s\approx 4.8Rq$	ZrO spray-on roughness particles
2003	Bunker	$k_s\approx 10Ra$	Polished TBC
2004	Shabbir and Turner	$k_s=8.9Ra$	Turbine roughness
2004	Zhang and Ligrani	$k_s\approx 1.9Rz$ as $f(\Lambda_s)$	20–150 μm Ni particles
2005	Bons	$0.5<k_s/Rz<3.5$ as $f(\alpha_f)$	Scaled turbine blade roughness
2005	Syverud et al.	$0.4<k_s/k<2$ as $f(\lambda)$ [47]	Salt grains from sea-spray ingestion
2005	Stripf et al.	$2<k_s/k<5$ as $f(k,t)$	Ordered arrays of truncated cones of height, k, and spacing, t
2005	Hummel et al.	$k_s\approx 5.2Ra$	Correlation with various surfaces
2006	Yuan and Kind	$k_s\approx 1.8k$	Sparsely distributed sandgrains of average size k

For flow in pipes or over plates, roughness has no effect on the shear stress providing either the flow is laminar or the protrusions do not penetrate through the viscous sublayer. (see Schlichting **[4]**). It follows that for turbulent flow, the thickness of the viscous sublayer,

$$\frac{\delta_s u^*}{v} \cong 5 \tag{2.117}$$

Where u^* is the friction velocity and defined as

$$u^* = \sqrt{\tau_w/\rho} \tag{2.118}$$

Note that it is called the friction velocity because of it has dimension m/s, although it is not actually a flow velocity. A surface is regarded as hydraulically smooth if the equivalent sand grain height thickness less than the thickness of the viscous sublayer, $k_s < \delta_s$. In other words, the height of the roughness is so small that all protrusions are contained within the laminar sub-layer in this region.

According to Nikuradse's experimental data, it is convenient to classify turbulent flow into three region depending on the size of roughness height parameter, $k_s u^*/v$

1- Hydraulically-smooth region : $k_s u^*/v < 5$
2- Transition region: $5 < k_s u^*/v < 70$
3- Completely-rough region: $k_s u^*/v > 70$

In hydraulically-smooth region, the shear stress depends only on the Reynolds number; in transition, it depends on both the Reynolds number and the roughness and in completely-rough regime, it depends only on the roughness. Later researches shows that theory is valid in a same manner for rotating disks and; moment correlations are also derived from tests for rough disks, which will be given on next chapter.

As a conclusion of this part, roughness effects are generally explained with the protuberance of the effective roughness k_s in comparison with the thickness of the viscous sublayer, δ_s. In the two-dimensional boundary layer flow along a smooth flat plate, δ_s is known to increase gradually in proportion to the one-tenth power of the flow-directional distance. On the other hand, in the three-dimensional boundary layer flow along a smooth rotating disk, the tangential velocity difference $(1 - S_f)(\omega r)$ becomes larger toward the outer radius of the disk, and accordingly, the thickness of the viscous sublayer, δ_s becomes thinner toward the outer periphery. This can be proved theoretically as follows: Using equation (2.117), the thickness of the viscous sublayer of the disk is

$$\delta_s = \frac{5v}{\sqrt{\frac{1}{2} C_f [(1 - S_f)(\omega r)]^2}} \tag{2.119}$$

Which yields with some constant C_s,

$$\delta_s = C_s \frac{v}{\omega r\sqrt{C_f/2}} \tag{2.120}$$

For a forced vortex S_f will be constant or varies little in the radial direction as well as with the skin friction coefficient. As a result, the thickness of the viscous sublayer δ_s is nearly proportional to $1/r$ and becomes thinner toward the outer radius of the disk.

Thickness of the boundary layers and viscous sublayers are plotted in **Figure 2.32** for a smooth disk and the flat plate to make a comparison between. Calculations on the disk side, made for “free disk” case $\left(S_f = 0\right)$ of a 450 mm diameter disk rotating at constant nearly 14000 rpm in air at 1 atmosphere pressure and room temperature which corresponds to rotational Reynolds numbers, $Re_\theta = 5 \times 10^6$. Boundary layer thickness is written according to 1/7 th power law which corresponds to $\delta = 0.526\, r/\, Re_\theta^{0.2}$ and for the viscous sub length, skin friction coefficients is written according to Blasius’s law of skin friction but using local rotational Reynolds number as $C_f = 0.045(x^2 Re_\theta)^{-0.25}$ where $\delta_s = 5v/\omega r\sqrt{C_f/2}$.

On flat plate side, free stream velocity chosen as the tip speed of the disk ($U_\infty = \omega r$) to make the same Reynolds number axially at the end of the plate for a length of the plate equal to the radius of the disk. Boundary layer thickness is written from Schlichting as $\delta = 0.37\, l/\, Re_l^{0.2}$ where l is the axial distance and Re_l is the axial Reynolds number that equal to $Re_l = U_\infty l/v$. For viscous sublayer thickness of the flat plate again from Schlichting $\delta_s = 50l/Re_l\sqrt{C_f/2}$ was used where $C_f = 0.074Re_l^{-0.2}$. Assuming the transition completed at $Re = 3 \times 10^5$; turbulent boundary layer thicknesses are calculated from $Re_\theta = 3 \times 10^5$. Normally, it is expected that the secondary radial flow induced on boundary layer would have an effect on suppressing the boundary layer thickness in this kind of three-dimensional boundary layer. However, results not approving this, and in fact, boundary layer thicknesses for disk becoming larger than flat plate at same rotational and axial Reynolds number as shown in **Figure 2.32**.

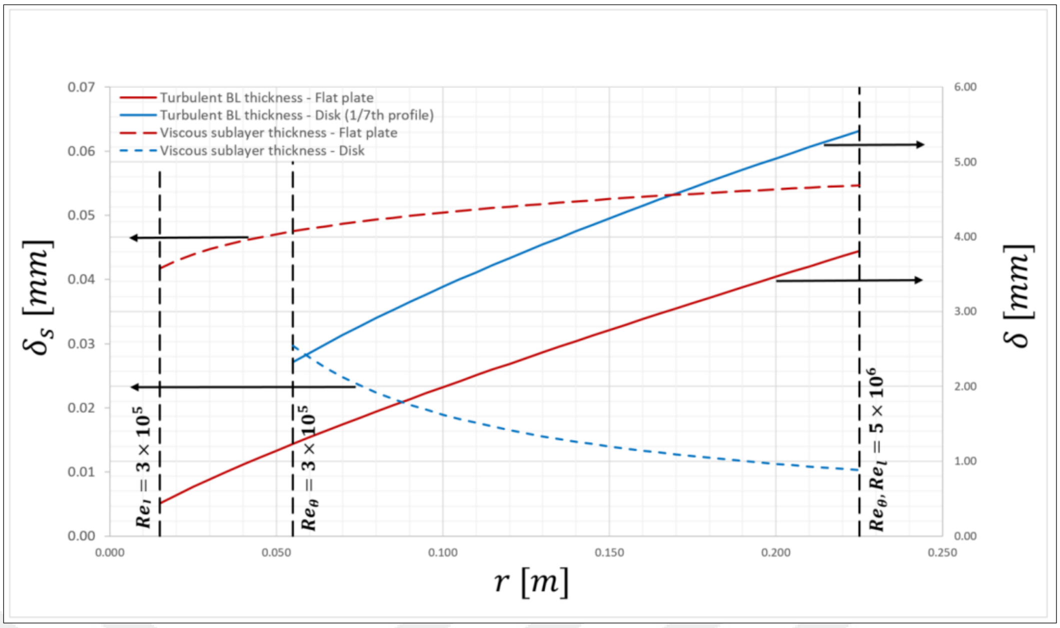

Figure 2.32: Comparison of turbulent boundary layer and viscous sublayer thicknesses for smooth disk and flat plate at same Rotational and Axial Reynolds Number.

It can be seen from the **Figure 2.32** that although both boundary layer thickness for the plate and the disk are increasing with the axial distance and through outer radius; the thickness of the viscous sublayer δ_s of the disk decreasing towards the outer radius while it is increasing for the flat plate. On the other hand, disk boundary layer thickness higher than the flat plate at same Reynolds number, which is also interesting.

2.6.3. Effect of Surface Roughness

Nece and Daily **[35]** studying the effects of disk roughness in the same enclosed rotor-stator rig that was explained in section by using the commercial grid papers bonded to the surfaces of the disk and casing. Authors used a neoprene bonding cement as the adhesive, and applied Duco cement in a fillet around the edges of the paper to serve as a sealer. The experiments are conducted for three different relative roughness R/k_s of 1000, 2000 and 3200 for three gap ratios $G = 0.023$, 0.061 and 0.112 in the range of rotational Reynolds numbers $4\times10^3 < Re_\theta < 6\times10^6$.

Nece and Daily **[35]** measured surface roughnesses of these waterproof grit papers and found that equivalent roughness k_s were about 2 times the arithmetic average roughness, R_a values. All measured and equivalent roughness values given in **Table 2.5**.

Table 2.5: Summary of measured and equivalent roughness height values of Nece and Daily test data **[35]**.

Surface finish	*ks[μm]*	*Rrms* [μm]	*Ra* [μm]	*ks/R*	*R/ks*	*ks/Ra*	*ks/Rrms*
Grit paper #180	79	45.7	35.6	3.2E-04	3165	2.2	1.72
Grit paper #120	124	66.0	53.3	5.0E-04	2003	2.3	1.88
Grit paper #60	249	157.5	134.6	1.0E-03	1001	1.8	1.58

As we mention before the four flow regimes in their tests repeated for equal roughnesses on both rotor and stator and also with a rough disk but smooth enclosure. It was found that roughness had no significant effect on the moment coefficient in the laminar regimes I and II; for $Re_\theta > 2 \times 10^5$ in turbulent regimes III and IV, C_m increased as the roughness increased. **Figure 2.33** shows a summary of the results obtained for the variation of C_m with Re_θ for equally roughened disk and enclosure case. It can be seen that, at large values of Re_θ, the moment coefficient becomes independent of the rotational Reynolds number. This is equivalent to the completely-rough region as we discussed in previous section 2.6.2.

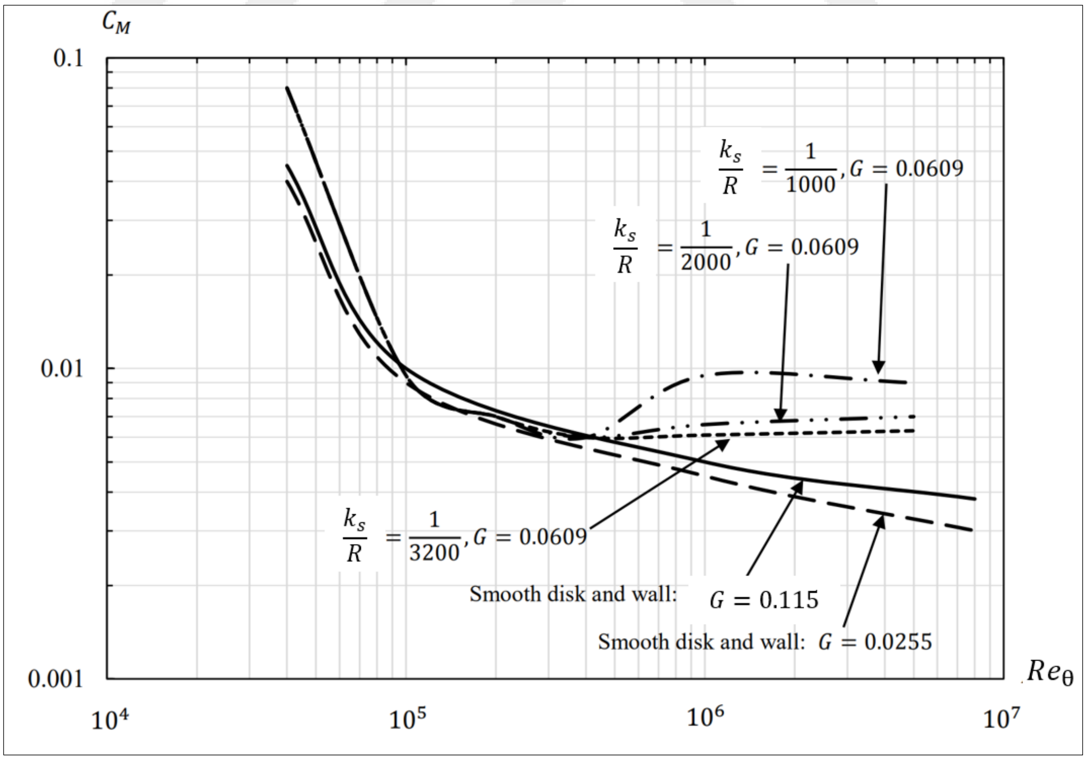

Figure 2.33: Nece and Daily's **[35]** rough disk torque data (equal roughness on disk and casing wall, two sides immersed), taken from Bo Hu **[20]**.

From results obtained at the largest values of rotational Reynolds number, Re_θ, for equal roughness on both rotor and stationary casing; Nece and Daily obtained the correlation for completely rough case where moment coefficients C_m become only depend on roughness

$$C_m^{-1/2} = 5.374 \log\left(\frac{R}{k_s}\right) - 3.394\, G^{1/4} \tag{2.121}$$

Which was in good agreement with their nine data points. Although velocity measurements conducted at $G = 0.0227$ showed that merged boundary layers occurred, there was no significant differences of C_m between Regimes III and IV.

The authors concluded that roughness effects started to become significant for

$$Re_\theta \cong 777.8\, \frac{\left(\frac{R}{k_s}\right)^{\frac{2}{5}}}{{C_m}^{1/2}} \tag{2.122}$$

Beyond this critical Reynolds number, values of C_m became greater than for corresponding smooth-disk cases and the completely rough regime started at

$$Re_\theta \cong 8131.7\, \frac{\left(\frac{R}{k_s}\right)^{\frac{1}{10}}}{{C_m}^{1/2}} \tag{2.123}$$

Once again, note that all values are given for the one side of the disk only.

Dorfman **[12]** calculates the frictional torque of a rough disk using logarithmic velocity profile that driven for rough tubes and develops equation **(**2.124) for the moment coefficient of “free disk” case stating that valid for the range of $125 < R/k_s < 3000$ relative roughness values.

$$C_m = 0.054 \left(\frac{R}{k_s}\right)^{-0.272} \tag{2.124}$$

Kurokawa, Toyokura, Shinjo and Matsuo **[36]** carried out a combined theoretical and experimental study of the effects of roughness on a flow along an enclosed cavity (similar to Daily’s test rig) where rotor and stator could be made independently rough or smooth. They solving the momentum-integral equations using logarithmic velocity profiles and test data for both rotating disk and stationary casing which giving close results to Daily's experiment. In their experiments, a disk of 328 mm diameter was rotated in a water-filled casing with radial and axial clearances of 2 mm and 12.8 mm ($G = 0.078$) respectively. Surface roughness were obtained by cementing commercial waterproof grit papers onto the surface of the disk and/or the casing inner wall with a waterproof bonding cement. By using this method, their rotor and stator surfaces could be roughened to relative roughness R/k_s values from around 8500 to 1700. When a grit paper cemented, they adjusted the axial position of the disk by using the same grit paper as a spacer to keep constant gap ratio in the cavity and tests were conducted at constant rpm corresponding to rotational Reynolds number of $Re_\theta = 3.1 \times 10^6$ which meaning a fully turbulent flow over the whole disk except the center of the disk.

Authors measured the surface roughness of disk by roughness meters and tabulated all values in terms of arithmetic average height, R_a as well as corresponding root mean square heights, R_{rms}. In their study, it is found out that effective roughness heights, k_s were about 1.6 times (1.54 – 1.69) the root mean square, R_{rms} values and were about 2 times the arithmetic average roughness, R_a values as given in **Table 2.6**. Although the exact values are not given it is also stated that effective roughness heights, k_s were also nearly equal to the ten-points heights , R_z measured in accordance with JIS. (According to Japan Industrial Standard (JIS), the ten-point height , R_z is defined as the difference in height between the average of the third highest peaks and the third lowest valleys).

Table 2.6: Summary of measured and equivalent roughness height values of Kurokawa et al. test data **[36]**.

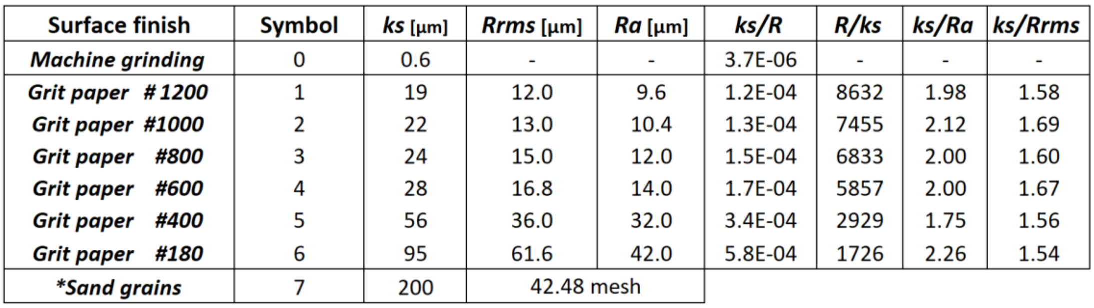

Surface finish	Symbol	*ks* [μm]	*Rrms* [μm]	*Ra* [μm]	*ks/R*	*R/ks*	*ks/Ra*	*ks/Rrms*
Machine grinding	0	0.6	-	-	3.7E-06	-	-	-
Grit paper #1200	1	19	12.0	9.6	1.2E-04	8632	1.98	1.58
Grit paper #1000	2	22	13.0	10.4	1.3E-04	7455	2.12	1.69
Grit paper #800	3	24	15.0	12.0	1.5E-04	6833	2.00	1.60
Grit paper #600	4	28	16.8	14.0	1.7E-04	5857	2.00	1.67
Grit paper #400	5	56	36.0	32.0	3.4E-04	2929	1.75	1.56
Grit paper #180	6	95	61.6	42.0	5.8E-04	1726	2.26	1.54
**Sand grains*	7	200	42.48 mesh					

*To realize No.7 roughness, they cemented the sieves of the No. 42-43 meshes onto the disk surface.

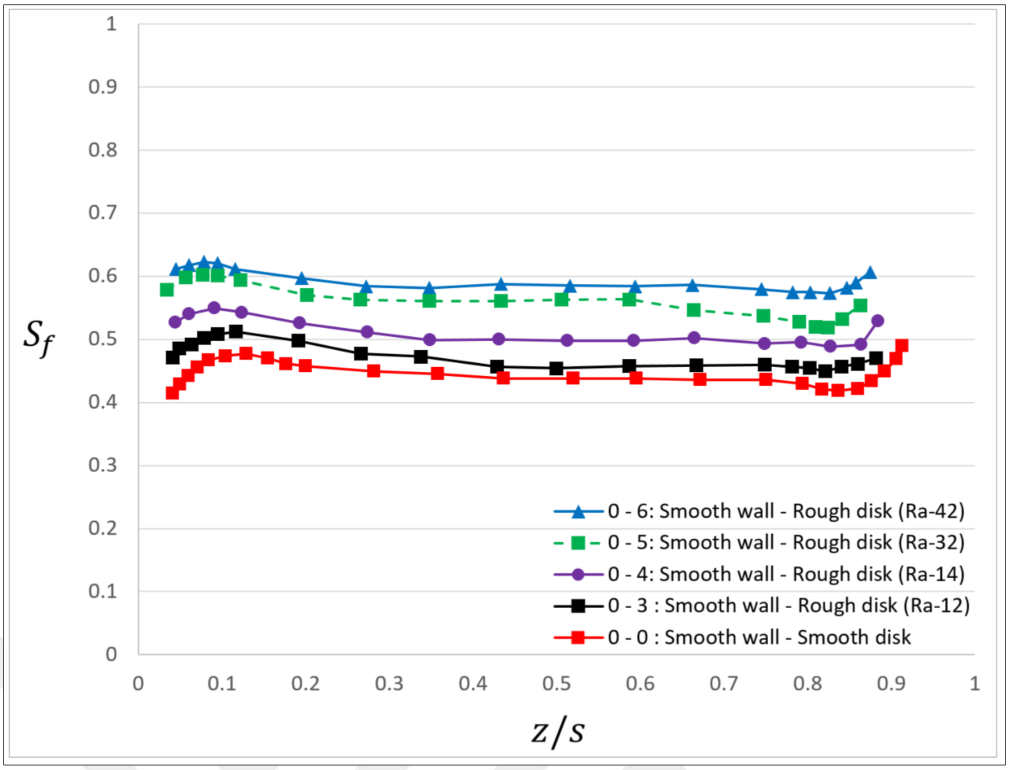

Figure 2.34: Roughness effects on swirl factor re-plotted from Kurokawa et al. **[36]**.

Tangential velocity profiles that measured at $x = 0.79$ with a three hole cobra probe, are re-plotted in **Figure 2.34** for the case where only the roughness of the disk is adjusted and the casing kept smooth. It can be seen that roughness has a significant effect on the core rotation swirl factors but the boundary layer thicknesses on both walls just show a slight change with it. Since increasing the roughness of the rotating disk meaning additional rotor torque, swirl factor of the rotating core increasing from $S_f = 0.43$ (both casing and disk smooth) to approximately $S_f = 0.58$ for the roughest case measured (No. 6).

Figure 2.35 shows the results when the surface roughness kept constant for the rough disk, smooth enclosure case, for the smooth disk, rough enclosure case, and for the rough disk, rough enclosure case in comparison with the results for the smooth disk, smooth enclosure case. Moreover, as we expect, when casing roughness increased which meaning additional negative torque, core rotation swirl factor is decreasing; also swirl data showing that if roughness increased same amount on both the disk and the enclosure wall, swirl factors are almost the same with smooth walls on both the disk and the enclosure case.

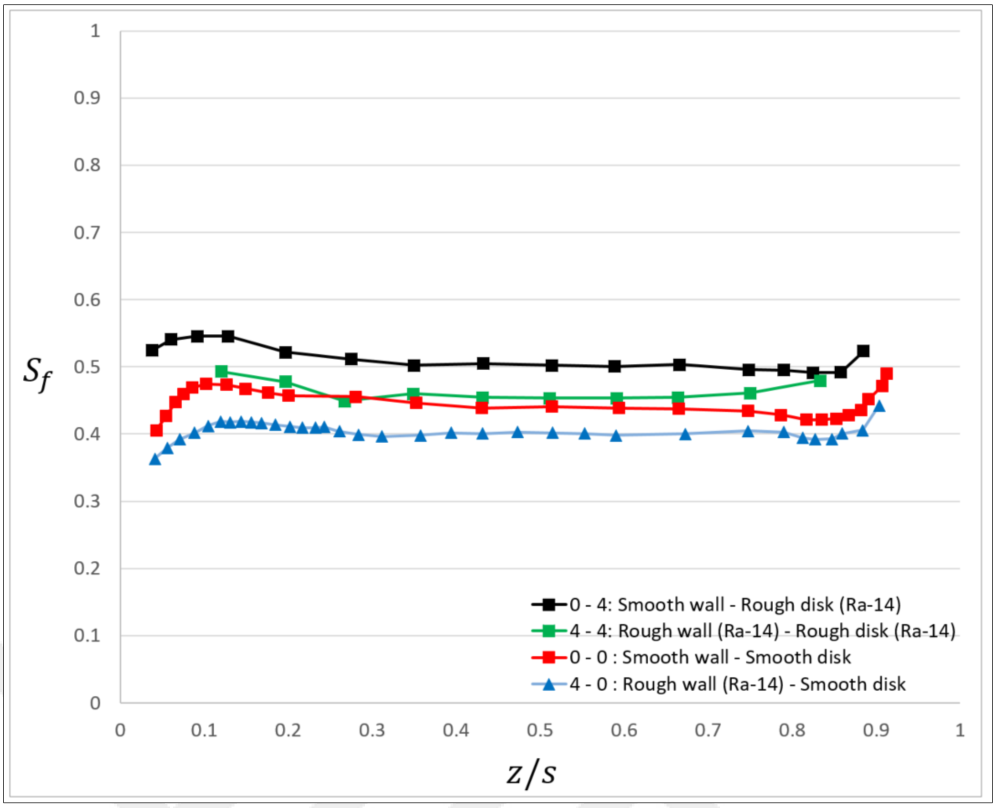

Figure 2.35: Core rotation swirl factors, S_f for constant roughness re-plotted from Kurokawa et al. **[36]**.

Kurokawa and others **[36]** additionally taking measurements through radially by traversing three-hole cobra probe and a pitot tube. **Figure 2.36** shows the test data taken for smooth enclosure and roughness of the disk varying. As we mention previously on section 2.6.2., thickness of the viscous sublayer on the disk and on the stationary casing becomes thinner toward the outer periphery; accordingly, roughness effects appearing first at the outer periphery of the disk. From **Figure 2.36** this effect can be recognized from the curves of number 2 and 3, swirl factor increasing first at the outer radii with an increase of the disk roughness. With further increase of roughness (number 4 and 5 roughness case), swirl factors beginning to apart from those for the smooth case and the boundary layer flow might be in the transition region($\delta_s \leq k_s$) at $0.4 < x < 0.8$. When the roughness are large enough (No.6 case), the boundary layer flow comes into the completely rough region from x=0.4 to outer periphery, and the core rotation becomes nearly constant in the radial direction. From other perspective, torques are increased enough (No.6 case) to make forced vortex throughout the whole radius so that fluid core starting to rotate with constant swirl factor.

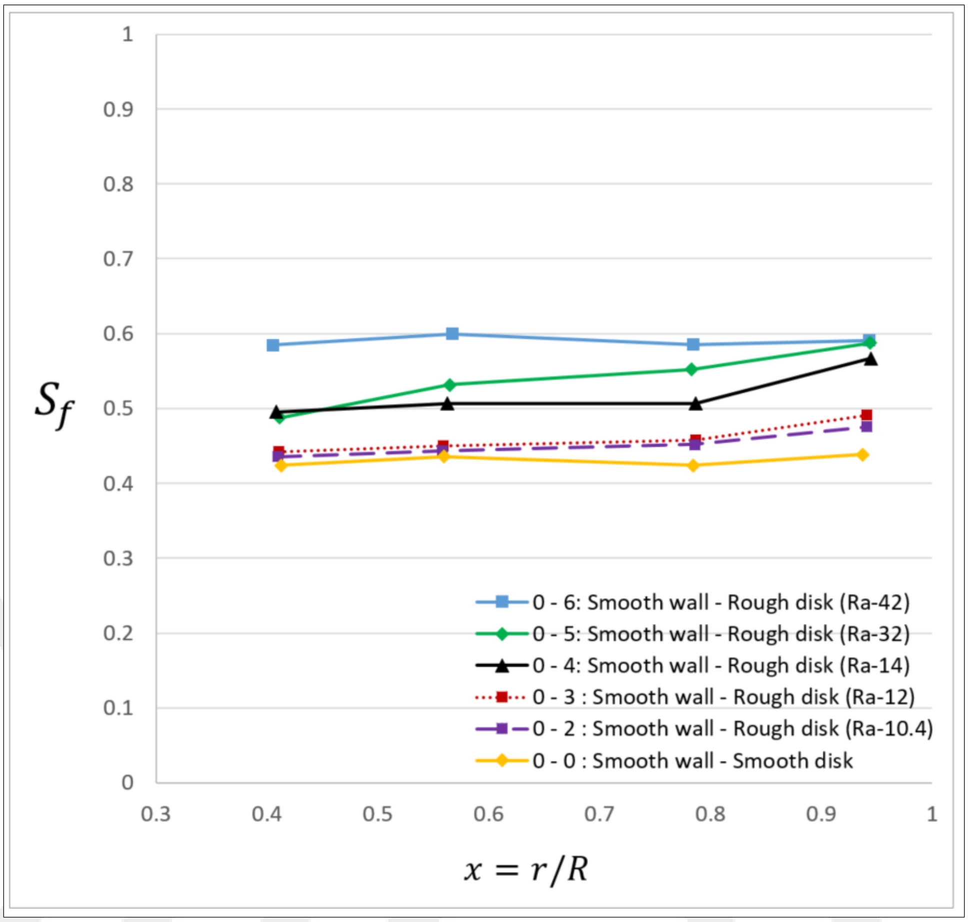

Figure 2.36: Roughness effects on radial distribution of swirl factors re-plotted from Kurokawa et al. **[36]**.

In **Figure 2.37**, we are seeing the same behavior for constant roughness cases, the core rotation swirl factor is smaller for the smooth disk, rough enclosure case, and is larger for the rough disk, smooth enclosure case than that for the smooth disk, smooth enclosure case. Moreover, for the rough disk, rough enclosure case of equal roughness, swirl factor is a little higher than that for the smooth disk, smooth enclosure case. In addition, roughness effect appearing again first at outer radii and forcing higher and lower swirl factors at the outer periphery of the disk.

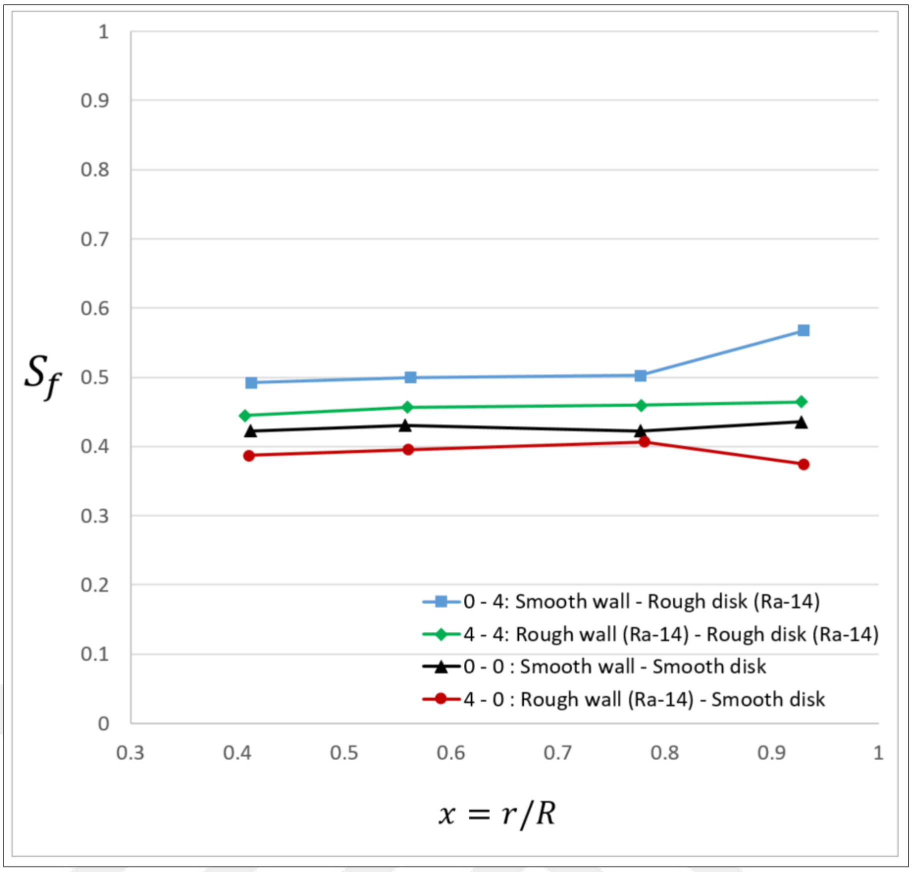

Figure 2.37: Radial distribution of swirl factors for constant roughness cases **[36]**.

The "free disk" windage powers are calculated from equation **(**2.47**)** and re-plotted in **Figure 2.38** for rough disks together with smooth ones that calculated in section 2.4 for our test rig case 450 mm diameter disk rotating in air at 1 atmosphere pressure and room temperature. For rough disks, equivalent roughness, k_s values are taken as 2 times average roughness, Ra and moment coefficients calculated with equation **(**2.124**)** which corresponding to the range of $890 < R/k_s < 4100$ for our disk. It can be seen from the figure, as the surface roughness increases, there is a significant increase in friction and therefore an increase in windage. For $Ra = 32$ µm, windage powers almost doubling the power required for smooth ones. Although this value is simply too rough for gas turbine applications, less roughened values are not plotted to stand in the relative roughness range of the correlations. Note once again that these powers all calculated to rotate the one side of the disk. If there is a symmetry and similar flow conditions on the other side of the disk, simply multiplying these numbers by two will gave the total windage loss of the disk by neglecting the loss coming from the tip of the disk.

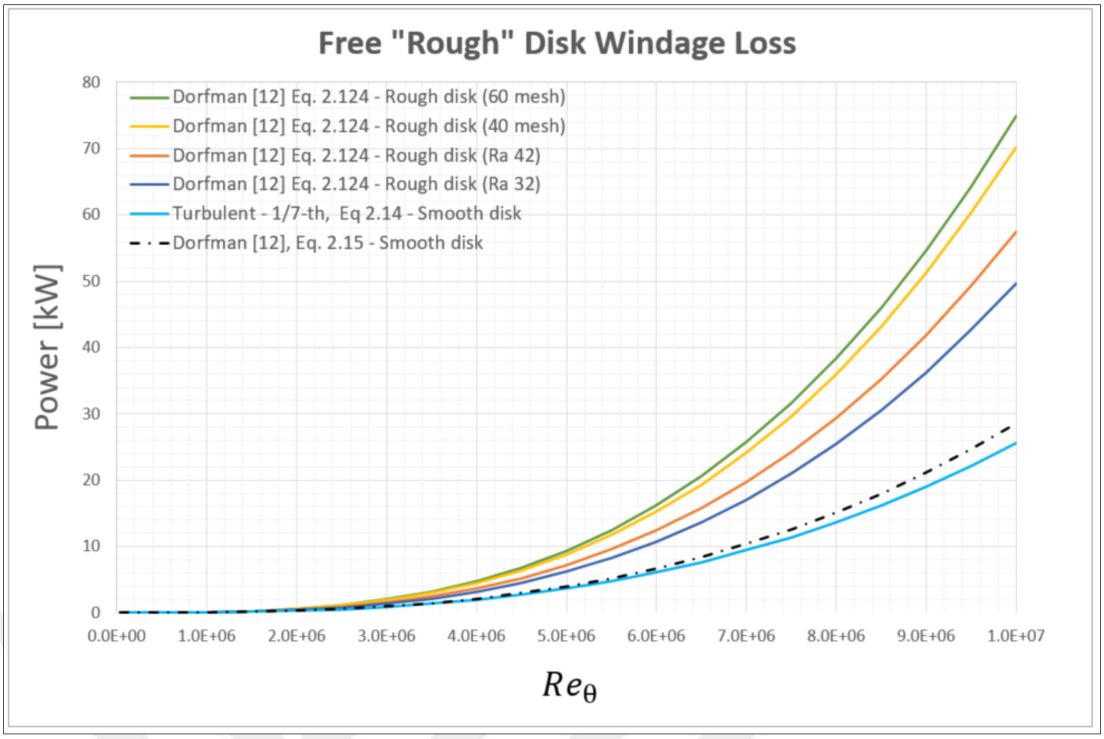

Figure 2.38: Comparison of “Free disk” windage losses for smooth and roughened cases.

In **Figure 2.39**, experimental data from Theodorsen and Regier **[6]** for smooth and roughened disk (60 mesh) compared with the curves from the theory. Although authors do not state it in their article, the relative roughness, R/k_s value given by Dorfman **[12]** as 1205 for this specific test. This value corresponding to equivalent roughness height, k_s value of 250 and seems to be logical if we consider Kurokawa’s value of $k_s = 200$ for 40 mesh. From the figure, one can clearly see the early transition for roughened disk. Smooth disk passing to transition at about $Re_\theta = 3 \times 10^5$ while this value dropping to around $Re_\theta = 2.2 \times 10^5$ when the disk roughened. For roughened disk, completely rough regime starting around $Re_\theta = 6 \times 10^5$ and corresponding moment coefficients becoming independent of the Reynolds number where the moment coefficient calculated with the equation **(**2.124**)** giving about 15 percent less value than experimental data. Dorfman **[12]** stating that this difference can be resulting from the rim of the disk. Since the disk thickness was not given by authors no comments can be made related to total power consumption of it.

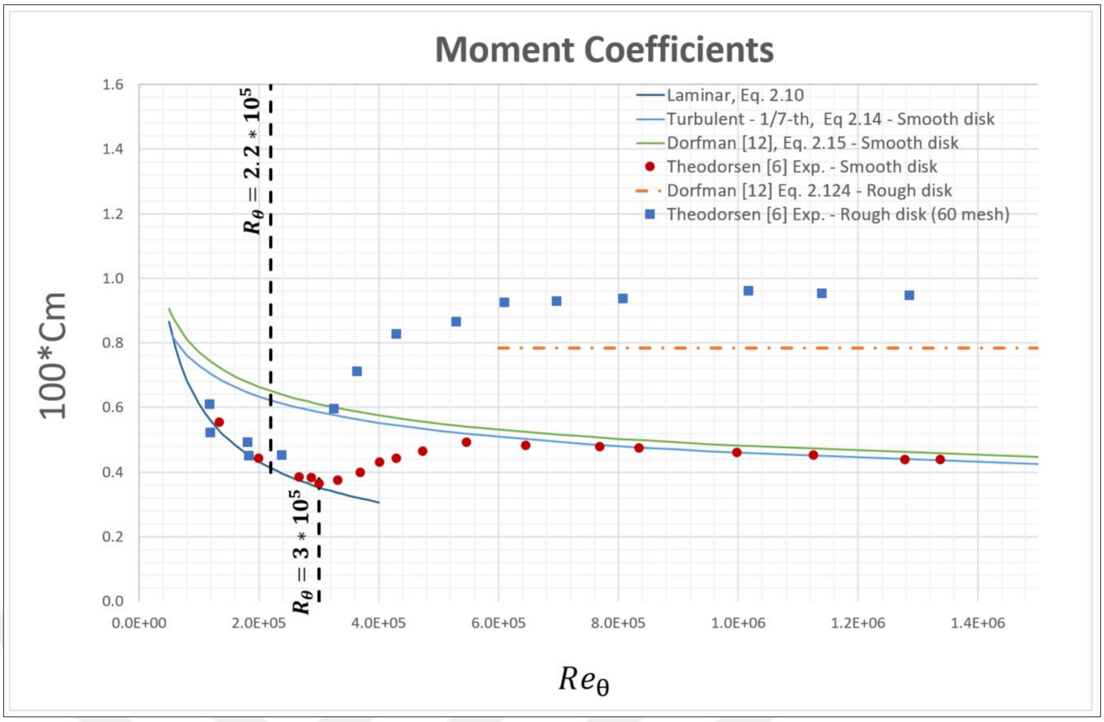

Figure 2.39: Comparison of "free disk" case theory with experimental data of Theodorsen and Regier **[6]** on 24-inch diameter smooth and rough disk that roughened for $R/k_s = 1205$.

In **Figure 2.40**, windage powers for our test rig case re-calculated from equation **(**2.47**)** for moment coefficients coming from Nece and Daily's empirical equation **(**2.121**)** that derived from their enclosed cavity tests, together with moment coefficients coming from equation **(**2.124**)** that theoretically derived by Dorfman **[12]** for completely-rough "free disk" case. One can see how significantly windage powers decreasing due to the decrease in tangential shear under core rotation. Nece and Daily **[35]** conducted these roughness experiments for three gap ratios $G = 0.023, 0.061$ and 0.112 as they did before for smooth disks; and corresponding core rotation swirls are given in **Table 2.7** by Daily et al. **[19]** for smooth disks and casings. Since Nece et al. **[35]** derived these correlations by roughening both disks and casing in experiments, we can assume that smooth case swirl factors will remain same for roughened cases as we saw from Kurokawa et al. **[36]** test results. Therefore, we can conclude that windage reducing about 40 percent for each equally roughened disk cases from "free disk" to cavity where core rotation swirl factor at about $S_f \approx 0.45$.

Table 2.7: Measured swirl factors for zero throughflow by Daily and Nece **[19]**.

G	S_{f_0}
0.064	0.46
0.102	0.44
0.217	0.41

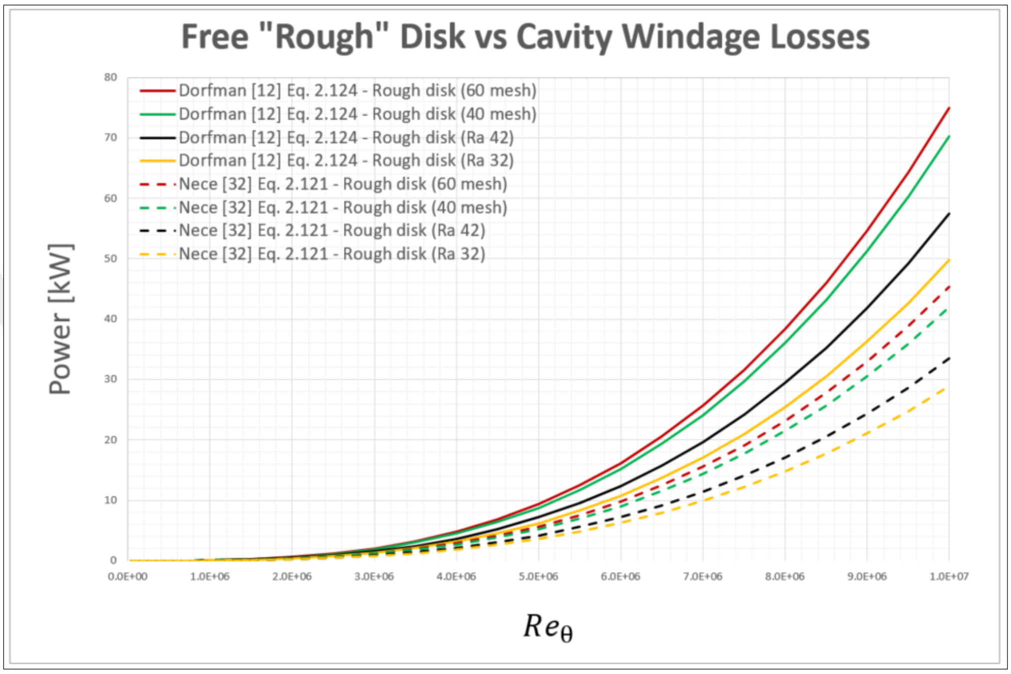

Figure 2.40: Comparison of “free disk” vs cavity ($S_f \approx 0.45$) cases for roughened disks.

It can be concluded that a too much increase in the roughness of the disks can lead to a significant increase in the windage power. However, if the height of the protrusions causing the roughness is considerably smaller than the thickness of the viscous sublayer, $k_s \ll \delta_s$ roughness has no effect because the fluid then will flow round the protrusions without separation and without vortex formation. When they are of the same order of magnitude as δ_s, the influence of the roughness begins to be noticeable (transition) and finally the roughness is of decisive importance when the protrusions are noticeably higher than the thickness of the viscous sublayer so that separation of the flow round the protrusions leads to the result that the structure of the flow and the friction become independent of the Reynolds number and depend only on the roughness which is the condition of complete roughness.

From other perspective, roughening disks or casing will increase the positive or negative torque taken by fluid respectively and can alter the core rotation swirl inside the cavity. If core rotation swirl changes, everything from windage power to static pressure distribution will also change as well as with pumping flow and axial thrusts to disk and casing. Therefore, although these cases are simply for too rough compared to our real case applications, it can be concluded roughness is an important parameter and results in significant windage increases depends on how rough the surface is. However, what is the limit roughness value for a disk to be considered as smooth? This will be our next topic under the "admissible roughness" title.

2.6.4. Admissible Roughness

Schlichting **[4]** plotting skin friction data for two-dimensional turbulent boundary layer flow over sand-roughened plates (again based on Nikuradse's pipe flow data **[33]**) and noted that the first evidence of roughness influence for

$$k_{s,adm} \cong C_{adm}\nu/U_\infty \quad (C_{adm} = 100) \tag{2.125}$$

In other words, admissible roughness $k_{s,adm}$ is defined as the maximum roughness which produces no effect upon the flow and for which the disk behaves hydraulically "smooth". From other perspective, hydraulically "smooth" region ends when the dimensionless roughness parameter $k_s U_\infty/\nu$ becoming higher than threshold value of "100". Therefore, this parameter sometimes called as roughness Reynolds number, Re_k which defined as

$$Re_k = k_s U_\infty/\nu \tag{2.126}$$

Nece and Daily **[35]** writing roughness Reynolds number according to tip speed of the disk ωR and giving the range for admissible roughness as

$$100 < \frac{\omega R k_{s,adm}}{\nu} < 200$$

Kurokawa et al. **[36]** later on, confirming that admissible roughness formula (Eq. **(**2.125) proposed by Schlichting is still effective in three-dimensional boundary layer flow, if the free stream velocity, in fact, U_∞ replaced with the relative velocity of the core rotation flow to the wall velocity $(1 - S_f)\omega r$.

Based on this fact, if we re-consider Nece and Daily **[35]**'s enclosed cavity tests; they also had average core rotation about $S_f \approx 0.45$, and if we re-write their results according to their relative velocities by simply multiplying with $(1 - S_f)$, admissible roughness range becomes

$$55 < \frac{(1 - S_f)\omega R k_{s,adm}}{\nu} < 110$$

Which also closely confirming once again the "100" threshold given by Schlichting as the upper limit.

For a better understanding the concept of the admissible roughness, "100" threshold roughnesses to rotational Reynolds numbers are given in **Figure 2.41** in terms of average roughness height for free disk ($S_f = 0$) case by assuming $k_{s,adm} = 2 \times Ra_{adm}$. One way of looking at, for a disk to be fully smooth from center to rim, surface finish should be equal to or below the corresponding value for a specific rotational Reynolds number.

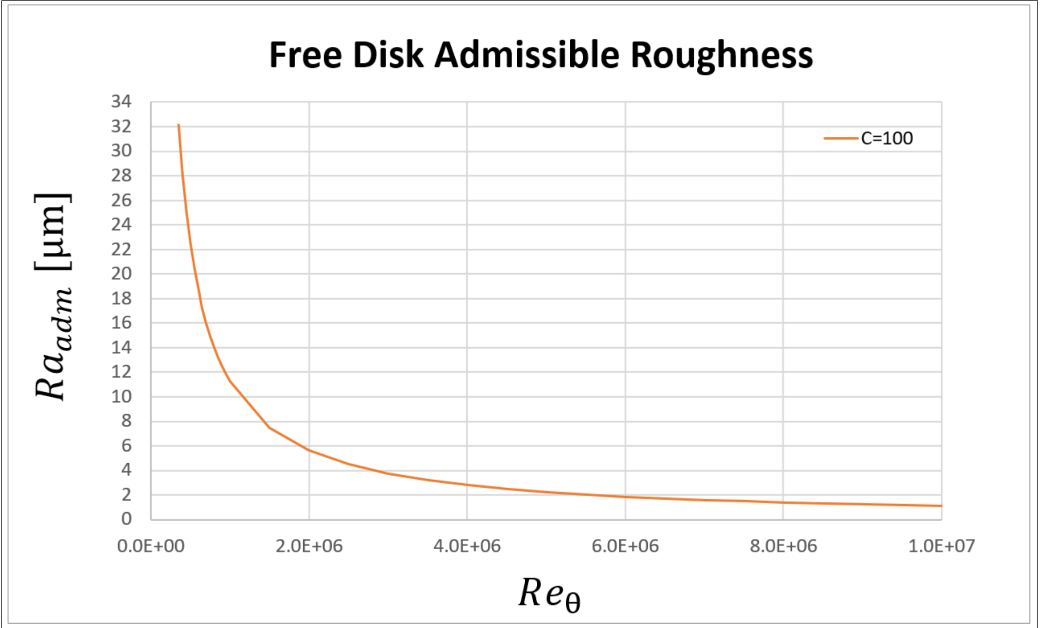

Figure 2.41: Admissible average roughness height variation with rotational Reynolds number ($k_{s,adm} = 2 \times Ra_{adm}$).

Other way of looking at **Figure 2.41,** it gives us the maximum Reynolds that a disk with a specific surface finish can reach while remaining fully smooth or up to which local Reynolds will the disk remain fully smooth.

In gas turbine applications, generally, surface quality of the disks around N8-N7 grade while for main aero path could be reducing to N5-N6 as one can see the corresponding finish values for grades from the chart below in **Table 2.8**.

Table 2.8: Surface finish chart.

Ra [μ m]	Ra [μ in]	Grade Numbers
25	1000	N11
12.5	500	N10
6.3	250	N9
3.2	125	N8
1.6	63	N7
0.8	32	N6
0.4	16	N5
0.2	8	N4

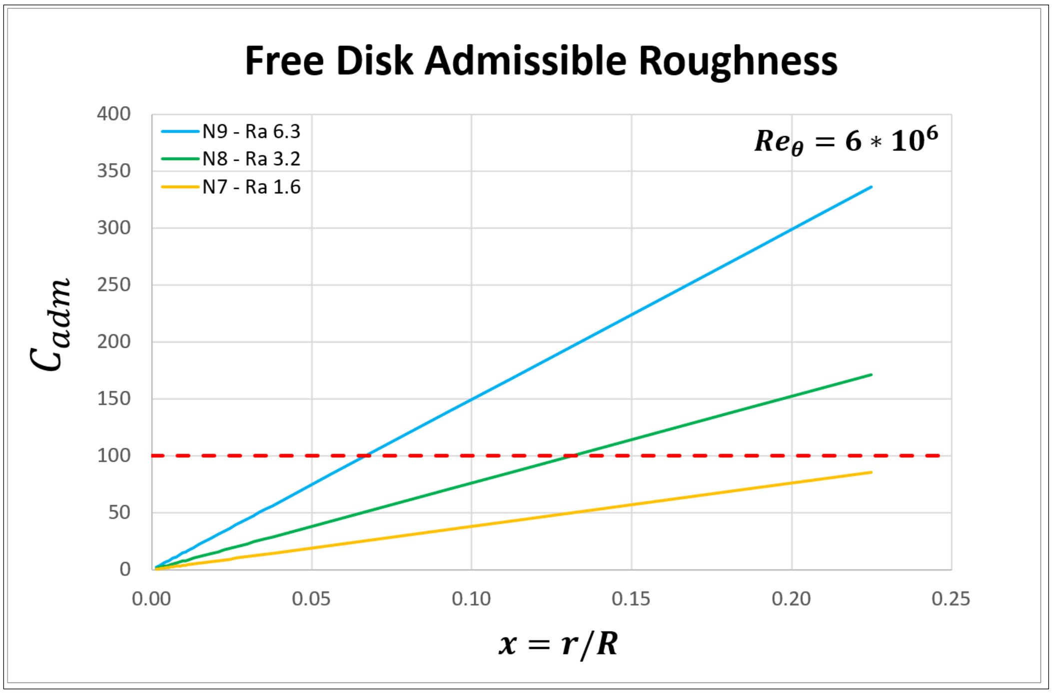

Figure 2.42: Admissible roughness constants according to local radii with different surface finishes at constant rotational Reynolds number of 6 million $(k_{s,adm} = 2 \times Ra_{adm})$.

In order to implement this, **Figure 2.42** written at maximum Reynolds number for our test rig case at different surface finishes and according to local radii. Figure shows that at maximum Reynolds number, $Re_\theta = 6 \times 10^6$, if we had a surface quality of 3.2 Ra, the disk will smooth only up to half the radius while will be fully smooth for 1.6 Ra or below.

However, remember that these values were calculated for free disk case. If we consider enclosed or shrouded cavities with core rotation, due to the reduction in shear between the disk and fluid, admissible roughness values will be higher as one can see from **Figure 2.43** below.

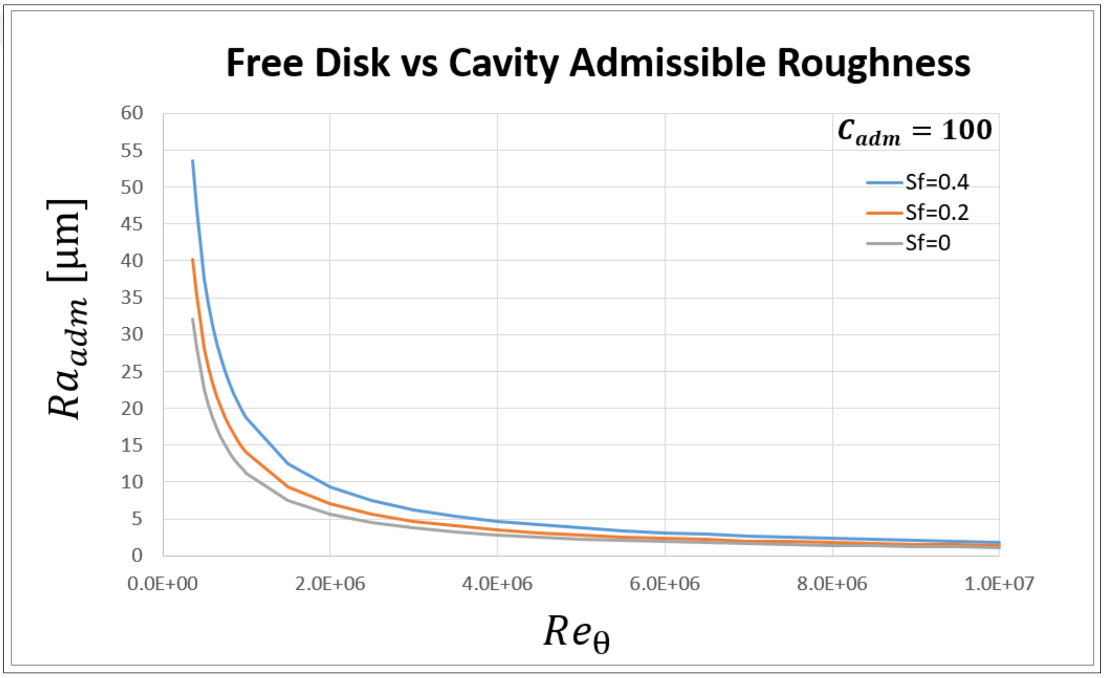

Figure 2.43: Admissible average roughness height variation with rotational Reynolds number for different swirl factors ($k_{s,adm} = 2 \times Ra_{adm}$).

As a conclusion of this part, all these remarks applied to a disk of constant radius, so that changes in Reynolds number imply changes in rotational speed if the fluid properties remain constant. Reader should give attention to that surface roughness should have no effect for laminar flows and below admissible roughness values for turbulent regime also. The transition to turbulence on disk is a function of the surface roughness and as for smooth disks, transitions from one regime to another do not occur over the entire disk surface at one time and it moves over the surface with changes of Reynolds.

Following the Reynolds at which turbulence originates, three types of flow may exist simultaneously on the disk surface: at the inner radii the flow is laminar; following the transition to turbulence the flow can be first turbulent “smooth”, in which case the roughness projections are effectively submerged within the viscous sublayer; then, at outer radii flow may become turbulent “rough”. If relative roughness (R/k_s) low enough and Reynolds high enough, the flow over the entire disk surface may become “fully rough” and at this condition, further increase in Reynolds will have no effect upon the value of the local friction coefficient thus be expected that C_m would be constant within this regime.

3. THEORETICAL ANALYSIS

Within the scope of this thesis, one-dimensional flow modelling mentioned in chapter 2.5 has been developed into the “SOCS design tool” with additional futures and capabilities using C-sharp and Microsoft Visual Studio whose interface shown in **Figure 3.1** for the first v0.1 release that capable of solving co-rotating and rotor-stator cavities for radial inward and outward flows.

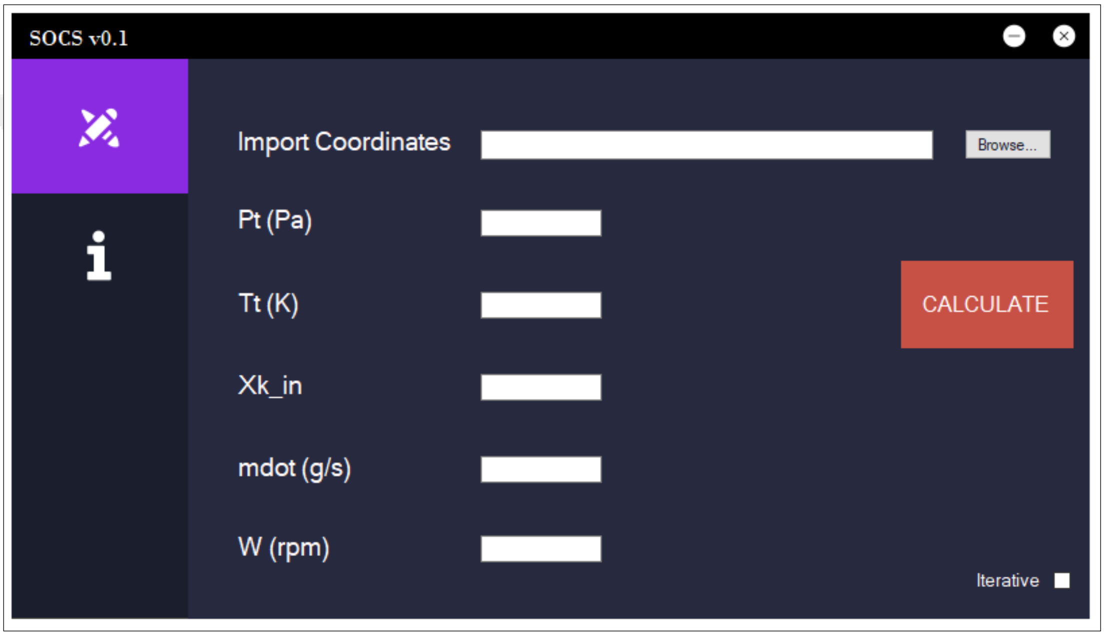

Figure 3.1: The interface of the improved cavity solver tool.

The SOCS design tool can automatically compute windage and swirl distributions for given inlet boundary conditions by user in a complex rotor-stator or rotor-rotor cavities regardless of co-rotation or counter rotation with varying physical properties such as density, specific heat capacity and viscosity for either radial inward or radial outward flow. In addition to being user-friendly, it is solution-robust and always converging in a few iterations without any user intervention. If iterative option selected, it is calculating each interval that given by user as a one cavity (even by assigning imaginary points if there is no radial match between walls in the data), then giving resulted pressure, and temperature distribution throughout the cavity.

Moreover, it is showing the axial load that is exert on the disks as well as displaying important parameters for flow characteristics such as rotational Reynolds number, non-dimensional superposed flow rate, turbulent flow parameter together with “free disk pumping” as well as corrected disk-pumping value according to averaged core swirl factor. One can see a test case example results file given in **Figure 3.2** for our shrouded test case cavity divided into 10 sub-cavity and solved with iterative option from its inlet to outlet.

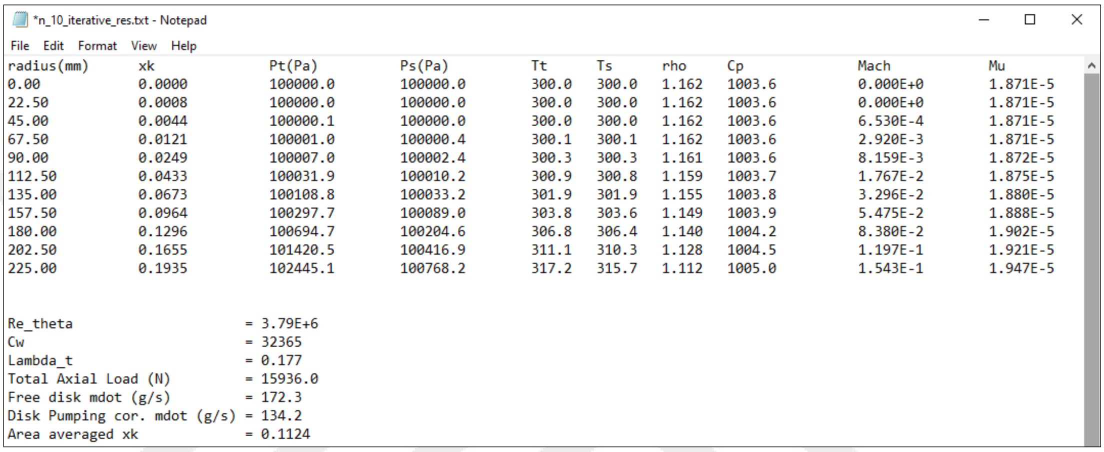

```
radius(mm)      xk            Pt(Pa)        Ps(Pa)        Tt     Ts     rho    Cp            Mach          Mu
0.00            0.0000        100000.0      100000.0      300.0  300.0  1.162  1003.6        0.000E+0      1.871E-5
22.50           0.0008        100000.0      100000.0      300.0  300.0  1.162  1003.6        0.000E+0      1.871E-5
45.00           0.0044        100000.1      100000.0      300.0  300.0  1.162  1003.6        6.530E-4      1.871E-5
67.50           0.0121        100001.0      100000.4      300.1  300.1  1.162  1003.6        2.920E-3      1.871E-5
90.00           0.0249        100007.0      100002.4      300.3  300.3  1.161  1003.6        8.159E-3      1.872E-5
112.50          0.0433        100031.9      100010.2      300.9  300.8  1.159  1003.7        1.767E-2      1.875E-5
135.00          0.0673        100108.8      100033.2      301.9  301.9  1.155  1003.8        3.296E-2      1.880E-5
157.50          0.0964        100297.7      100089.0      303.8  303.6  1.149  1003.9        5.475E-2      1.888E-5
180.00          0.1296        100694.7      100204.6      306.8  306.4  1.140  1004.2        8.380E-2      1.902E-5
202.50          0.1655        101420.5      100416.9      311.1  310.3  1.128  1004.5        1.197E-1      1.921E-5
225.00          0.1935        102445.1      100768.2      317.2  315.7  1.112  1005.0        1.543E-1      1.947E-5


Re_theta                     = 3.79E+6
Cw                           = 32365
Lambda_t                     = 0.177
Total Axial Load (N)         = 15936.0
Free disk mdot (g/s)         = 172.3
Disk Pumping cor. mdot (g/s) = 134.2
Area averaged xk             = 0.1124
```

Figure 3.2: Results file example.

This tool will be compared with validation test cases and CFD results later on but in this chapter, we will be questioning the necessity of dividing cavity into multiple control volumes. As we mentioned in chapter 2.5, the problem with one-dimensional flow modelling is the assumption that exit swirl at the outlet surface equals to the core rotation swirl of the cavity itself and calculating torques as well as static pressures accordingly. The accuracy of this assumption will be discussed in this chapter for one test cases cavity given in **Figure 3.3** between no division on whole cavity and dividing it into multiple control volumes.

In the **Figure 3.3**, cavity gap ratio is $G = 0.18$ and there is 1 mm axial clearance corresponding to $G_c = 0.0044$; all results are calculated for constant $12000\, rpm$ which corresponding to $Re_\theta \; = \; 3.8 \times 10^6$. Inlet conditions are 140 g/s air going into the rotor-stator cavity with zero swirl, where inlet total pressure are $P_{t_{in}} = 1\, bar$ and inlet total temperature are $T_{t_{in}} = \; 300\, K$.

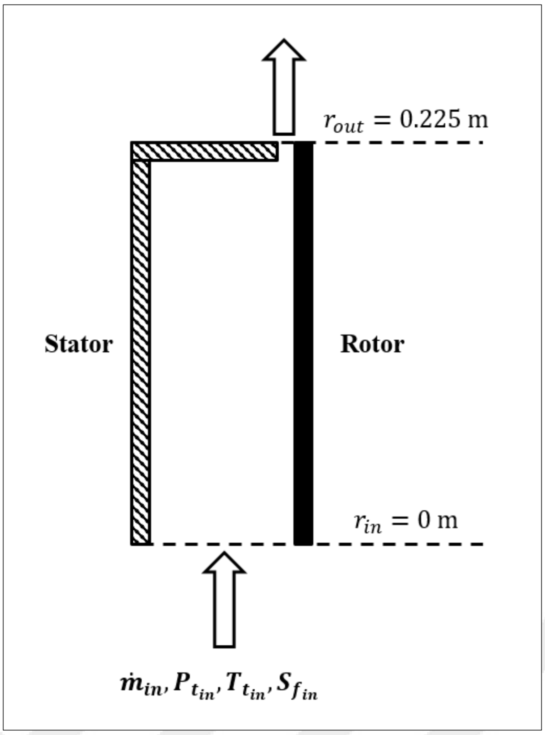

Figure 3.3: Cavity solver tool test case example rotor-stator cavity dimensions.

If we first look at swirl factors which is the key parameter for windage, pressure increase/decrease as well as for torques taken from rotating and stationary parts. One can see from **Figure 3.4** how dividing allows us to see more accurate results in terms of swirl distribution inside the cavity.

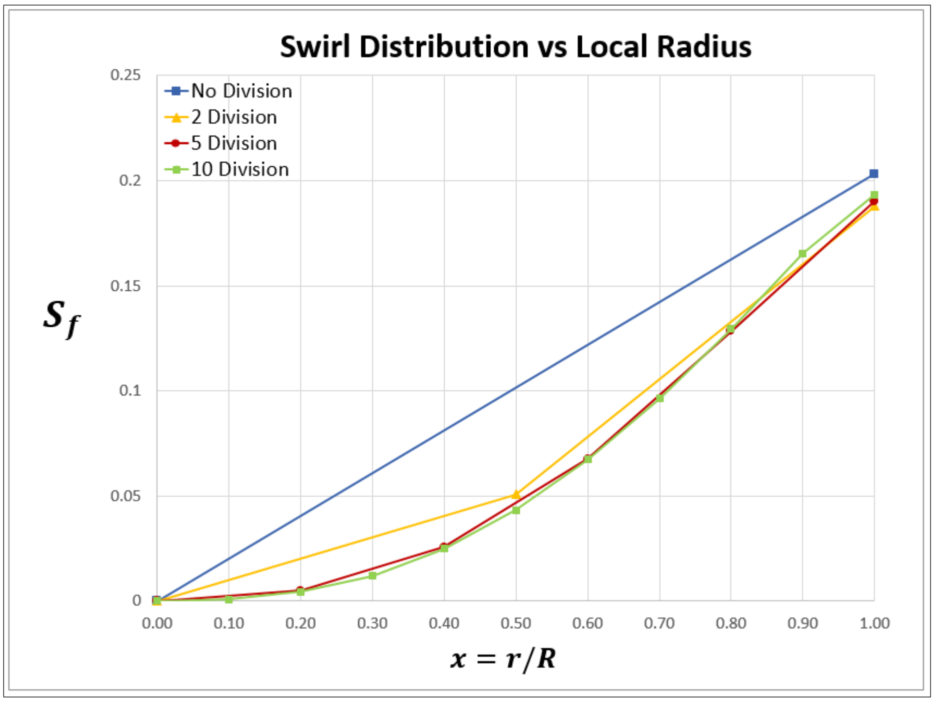

Figure 3.4: Swirl distributions inside the cavity for different number of division.

At low radii, since the torques are low, fluid cannot increase its swirl suddenly and actually, it is not even increasing up to almost half of the cavity. Although this depends on the superposed flow rates, we never expect much torques at low radii so that even if the amount of superposed flow was much less than this we would probably not expect an increase in swirl, if not up to half of the cavity may be up to a third. In terms of swirl distributions, dividing cavity into five in this case will be the reasonable choice. If we look at the exit swirl change with number of division as shown in **Figure 3.5**, exit swirl converging around 40 division and dividing it further does not change exit swirl anymore but differences are lower than 5 percent even when compared to no division case. Therefore, in addition to being not practical as well not applicable without programming, it seems not necessary thing to do.

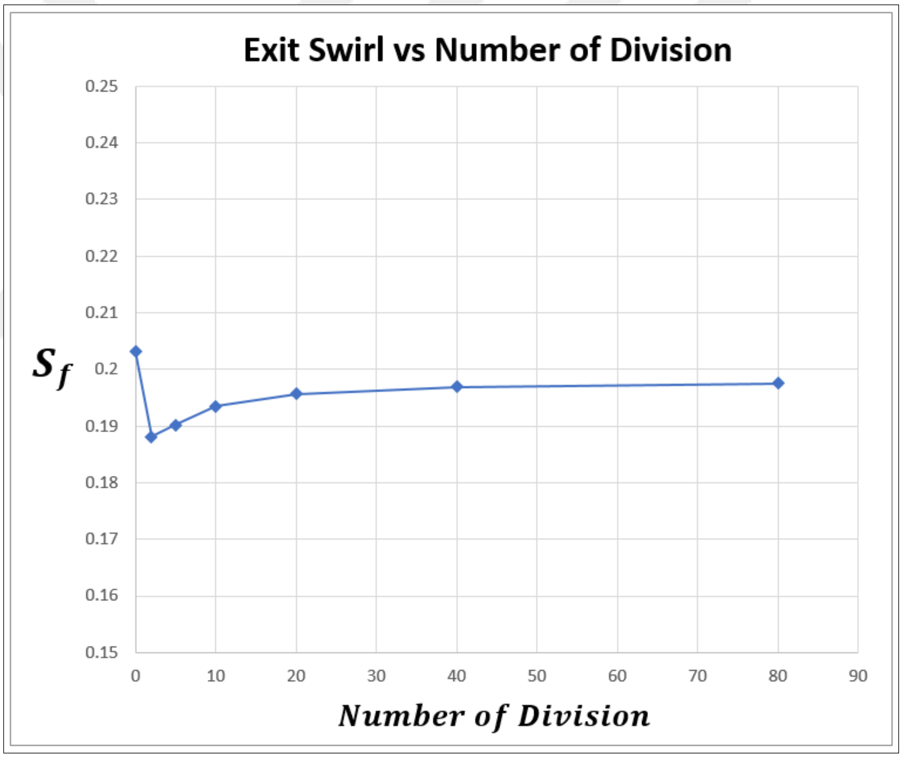

Figure 3.5: Exit swirl factor for different number of division.

If we investigate the windage heating by looking at total temperature increases from center to rim as shown in **Figure 3.6**, again almost through half of the cavity there is nearly no temperature increase at all and dividing cavity into multiple volumes allowing us to see more meaningful results in terms of heating. At low radii, where torques are low, windage levels are also low as we expect. After dividing it to even two control volume, exit total temperature not changing much with further division.

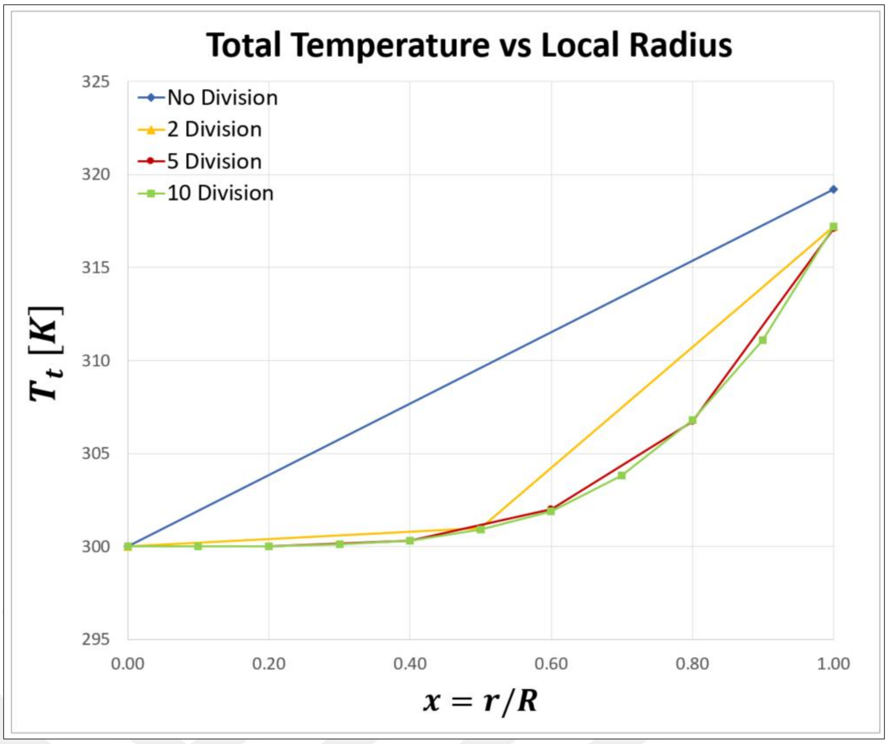

Figure 3.6: Total temperature increase of air for different number of division.

As we expect, exit total temperature converging with 40 division as swirls converge but differences are less than 1 percent as shown in **Figure 3.7.**

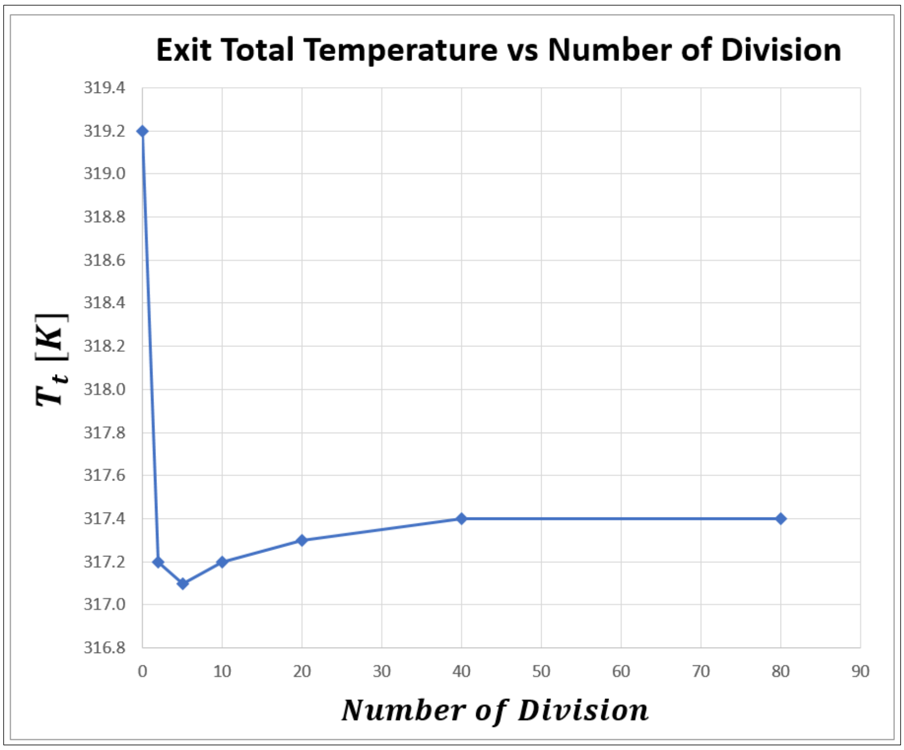

Figure 3.7: Exit total temperature for different number of division.

However, as shown in **Figure 3.8**, pressure increases are much more sensible to divisions compared to temperature increases. Since pressure increases are directly proportional to the square of the swirl factor through equation **(**2.109), when we model whole cavity as one, we have only one core rotation swirl, which is equal to the exit swirl. For this reason, we are calculating much more pressure increase. Even though it seems wrong and generating error for this particular case, it can be also true for such cases that the torques are sufficient enough to make core rotation completely forced vortex with constant swirl factor from center to rim through whole cavity.

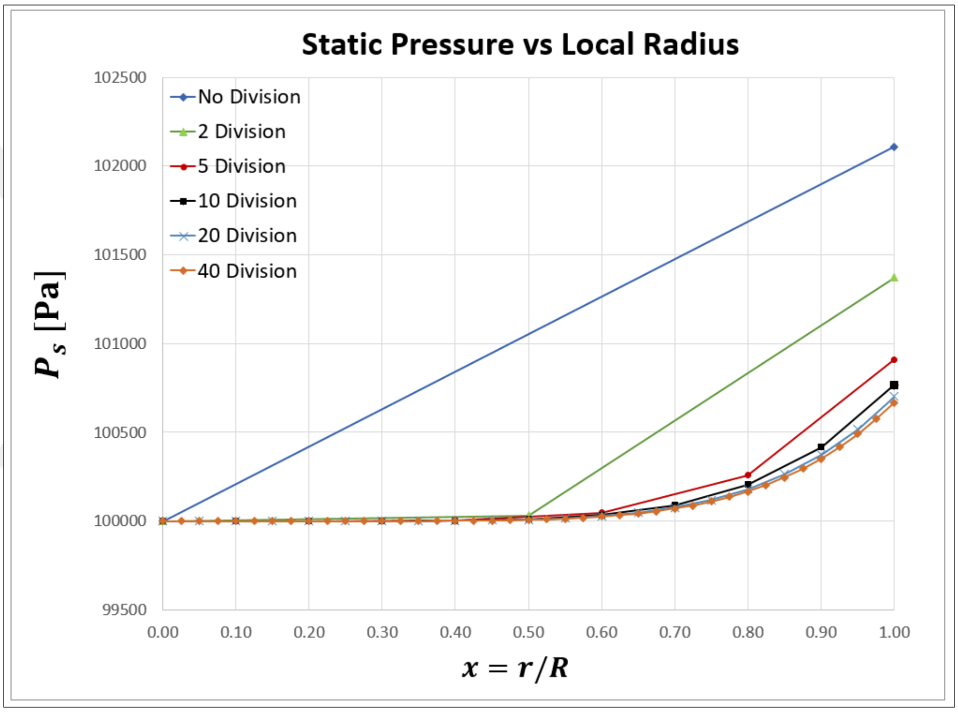

Figure 3.8: Static pressure distributions inside the cavity for different number of division.

When we look at the exit static pressure change with number of division**,** we can accept a converging around 40 division but to investigate its resulted error on axial thrust, **Figure 3.9** plotted for different number of divisions. Axial load changing around 1 percent between converged value and no division case.

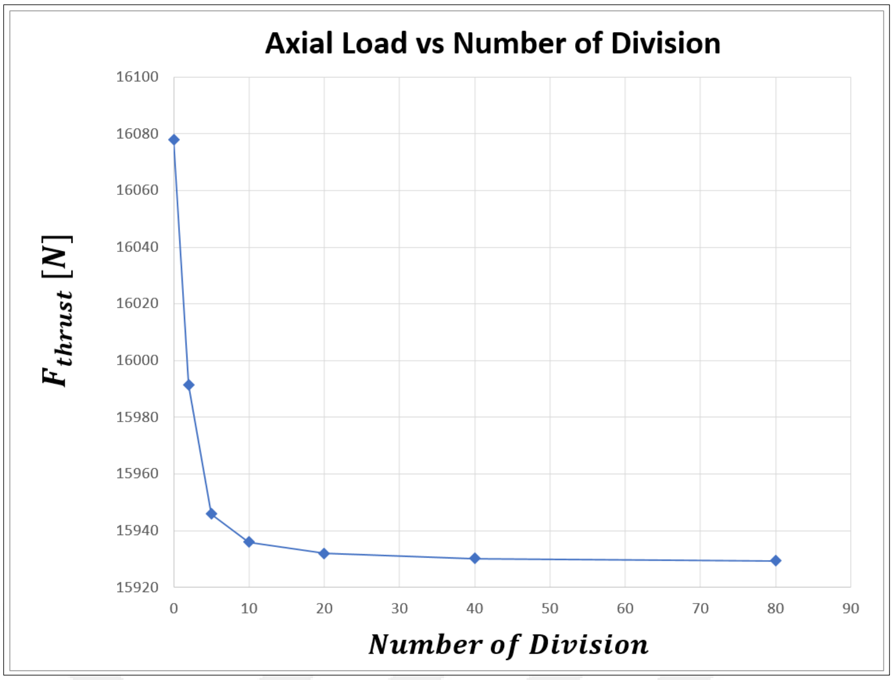

Figure 3.9: Variation of axial thrust with number of division.

As a conclusion to this part, it should remembered that in real gas turbine applications pressures are way higher than atmospheric pressures as in this case, so that meaning much dense fluid and usually have some swirl so that have its own momentum. Cavities includes multiple axisymmetric surfaces, which may comprise of radial, conical and horizontal surfaces and may have protrusions like bolts that tend to destroy the overall symmetry of the cavity. Additionally, the cavity may have multiple inflows and outflows at different radial location with different swirl, temperature and pressure conditions. For this reasons, these vortexes are neither completely free nor completely forced but in between, going in from some place to other, merging with another source of air so that adding itself some momentum or separating from and losing some. Behaving closely to forced vortex if torques are dominant and closely to free vortex if its own momentum is dominant. These are main factors in the first place that create a natural need to divide cavity into control volumes. In addition, dividing into one or two cavity where the radii are small so that torques would not be significant; and dividing into multiple cavities where radii are high meaning higher torques and high windage levels would be the best practice for real applications. Thus, these errors for a test case can be much higher for real case examples, and would be reduced by this way.

4. NUMERICAL ANALYSIS

Numerous CFD simulations using the commercial Ansys Fluent codes have been performed in the course of this study. The goal was to gather experience in how far the results close to experiments and the derivation of best practice of guidelines for the successive prediction of the flow in the rotor-stator cavities with throughflow. The major and most important results will be given in the following, but before diving into that a brief benchmark study is given about CFD studies and what has been learned so far.

4.1. Turbulence Model

Based on Owen and Rogers **[3]** writings, by the mid-1980s, eyes were turning from main flow-path to secondary air systems aiming further benefits and improvements, for example by reducing the amount of compressed air that is used for cooling of the vanes and blades as well as for sealing of the disks. Today, we aware of that SAS has a primary role for the reliability and performance of the engine not only one but from many aspects. Therefore, the accurate prediction of fluid flow within rotating systems has a great importance, and for this reason, it has been widely considered and being the subject of many studies from those years to the present. However, selection of a suitable turbulence model for the study of such complex flow remains an open issue in the literature for a long time with many lessons learned.

Chew **[38]** is the one who first studying the radial outflow between co-rotating disks, rotor-stator as well as for “free disks” using k-ε turbulence model. He compared simulation results with available experimental results of Bayley and Owen **[13]**, and also with Pincombe’s test results and concluded that k-ε model is not suitable for solving the flow around rotating systems. Later on, Chew and Vaughan **[39]** studying rotor-stator cavity with and without throughflow with a model based on Prandtl’s mixing length hypothesis inside whole cavity. Author’s finite difference solution giving quite comparable results to the experimental data of Daily and Nece **[19]** and Daily et al. **[18]** in terms of moment coefficients; and also velocity measurements are in reasonable agreement except with a tendency to under-predict the core rotation swirl in some cases. Authors concluding that mixing length model of turbulence is sufficiently accurate for engineering purposes. Iacovides and Theofanopoulos **[40]** trying a zonal turbulence modelling where using an algebraic model of Reynolds stress tensor and k-ε models in fully turbulent region and employing two different version of mixing length hypothesis near the wall for both co-rotating and the rotor-stator cavity either with and without throughflow. Authors trying to validate their rotor-stator cavity results with the experimental data of Daily et al. **[18]**, and for every test case examined, satisfactory predictions were obtained with at least for one of their turbulence models, however, no single form was satisfactory in all cases. Later on, Elena and Schiestel **[42]** proposed a variant of Reynolds Stress Model (RSM) that takes into account the implicit effects of rotation on the turbulence field and pointed out that the RSM model is the adequate level of closure compared to the classical k-ε model or to the Algebraic Stress Model approach. In addition, Poncet et al. **[24]** compared pressure and velocities measurements to improved version of the RSM of Elena and Schiestel **[42]** and confirming once again with excellent agreement in all conditions.

Some authors using k-ω Shear-Stress Transport model of Menter **[41]** in the meantime; and Da Soghe et al. **[43]** are comparing the standard k-ε and k-ω SST models including high and low Reynolds approaches together with those previously evaluated by Poncet et al. **[24]** through the RSM of Elena and Schiestel **[42]**. They are concluding that although the RSM improves the predictions compared to the other models, regarding the boundary layer profiles and for the turbulent field, the k-ω SST model offers best trade-off between accuracy and computational cost.

All of the models we have mentioned so far are using statistical methods based on the decomposition of average values and fluctuating parts for all randomly varying properties to predict turbulent flows. Averaging the equations giving the Reynolds averaged Navier-Stokes (RANS) equations, and closing the RANS equations by modelling Reynolds stress term (non-linear term) giving the solution which known as the closure problem. From eddy viscosity concept (k-ε, k-ω) to Prandtl's mixing length, all hypothesis answering the closure problem with additional equations where for k-ω, with additional two and for most complete turbulence model RSM with additional 8 equations. Although as we saw from benchmarks that RSM improves the predictions on the boundary layers profiles and for the turbulent field, it will result in much longer calculation times, since 8 additional equations are solved instead of two, which makes it impractical for most industrial applications.

Beyond these, there is a direct numerical simulation (DNS) as the most expensive one in terms of computational cost, where Navier-Stokes equations are numerically solved without any turbulence model or via low-pass filtering of the Navier-Stokes equations, Large eddy simulations (LES) as reduced cost comparing to DNS. For the first time, Lygren and Andersson **[52]** was performed direct simulations of fully turbulent flow between infinite rotor-stator disks. Their tangential velocity predictions are in good agreement with the experimental data from Itoh et al. **[46]** however, turbulent intensities were differ from the data. They stating the difference might be coming from the simulation model that based on infinite disks while in experiments of Itoh et al. **[46]** was finite shrouded rotor-stator cavity. As large eddy simulations being more affordable, their variety of applications, including rotor-stator cavities, are more commonly found in the literature. Andersson and Lygren **[53]**, later on, performing LES in an unshrouded rotor-stator cavity with high and low gap ratios for turbulent flows that corresponding to Regime III and Regime IV in **Figure 2.17**. Authors states that moment coefficients deduced from simulations matching well with correlations derived by Daily and Nece **[19]** on the rotor side, while at the stator side substantially lower. However, no conversion was given for skin friction coefficients to moment coefficients which is the non-dimensional form given by Daily and Nece **[19]** and their constants are not matching with those obtained for the one side of the disk from Daily and Nece **[19]** as given in equation **(**2.31**)**, and equation **(**2.32**)**. Severac et al. **[44]**, for the first time, investigating turbulent flow in an enclosed rotor-stator cavity both numerically using LES and experimentally using Laser Doppler Velocimetry (LDV) up to $Re_\theta = 10^6$ without throughflow. Authors found out that the stator boundary layer becoming already turbulent at $Re_\theta = 10^5$ while rotor boundary layer at $Re_\theta = 4 \times 10^5$. Makino et al. **[45]** using LES investigating laminar-turbulent transition in enclosed rotor-stator cavity for the rotational Reynolds numbers between $4 \times 10^4 \leq Re_\theta \leq 4 \times 10^5$, their numerical predictions are in agreement with the experimental data of Itoh et al. **[46]** and Cheah et al. **[47]**. Authors also stating that although the fluctuations decrease toward the hub on the stator side, the turbulent intensities are relatively larger than those on the rotor side. More recently, Fernando et al. **[48]** using LES to investigate surface roughness effects in rotor-stator cavity without throughflow. They are validating the model against the experimental and numerical data of **[44]**, **[46]**, **[47]** for smooth cases; and combining with the parametric force approach of Busse and Sandham **[49]**, obtaining results for rough cases. Although the model has not been validated for rough cases, authors showing that the method is applicable to model roughness effects in DNS and LES methods. Summary of turbulence models used in the literature given in **Table 4.1**.

Table 4.1: Summary table of turbulence models used.

Authors	**Through-flow**	**Shroud**	**Turbulence Model**	**Findings**
Chew **[38]**	Outflow	No	k-ε	Not suitable turbulence model for rotating systems
Chew and Vaughan **[39]**	Outflow	Yes	Mixing-length formulation	Acceptable agreements with test results.
Iacovides and Theofanopoulos **[40]**	Outflow	Yes	k-ε and algebraic stress model	No universal model is satisfactory in all cases
Elena and Schiestel **[42]**	No	Yes	RSM	Succeed to predict the velocity and Reynolds stress profiles
Lygren and Andersson **[52]**	No	No	DNS	Isotropic eddy viscosity model resulting in acceptable results
Poncet **[24]**	Outflow	Yes	RSM	Good agreement with the measurements
Da Soghe et al. **[43]**	Inflow/ Outflow	Yes	k-ε, k-ω SST, RSM	k-ω SST offers best trade-off between accuracy and comp. cost
Andersson and Lygren **[53]**	No	No	LES	Investigating turbulent flow in a cavity for different gap ratios
Severac et al. **[44]**	No	Yes	LES	Good agreements with LDV measurements.
Makino et al. **[45]**	No	Yes	LES	Good agreements with experimental data
Fernando et al. **[48]**	No	Yes	LES	Parametric force approach is feasible method to model roughness effects in LES

After long literature review, Shear-Stress Transport (SST) k-ω model of Menter **[41]** was chosen due to its high accuracy vs computational cost performance that experienced on previous researches. The idea behind SST model is to retain Wilcox k-ω model in the boundary layer region and to take advantage of free stream independence of a standard k-ε model in the outer part of the boundary. To achieve this, a k-ω formulation of a standard k-ε model is derived and merged together via blending function, which is activating k-ω in the near wall regions by being one and outside of it activating k-ε model by being zero **[54]**. Model used in their original form kept available by Fluent, no tuning of turbulence model constants was done. In addition, the corrections for compressibility and transition are applied. The correction for transition representing the low Reynolds number modification to turbulent viscosity proposed by Wilcox. On the other hand, compressibility correction affect turbulence through so called “dilatation dissipation” which accounts for the decrease in spreading or growing rate of mixing and free shear layers with increasing Mach number **[54]**.

4.2. Numerical Simulation Setup

In the current study, 2D axisymmetric (with swirl) RANS equations are solved with pressure based double precision solver of Ansys Fluent 2022 R1. The pressure-based (coupled) algorithm solves coupled system of equations comprising the momentum equations and the pressure-based continuity equation. The remaining equations are solved in a decoupled manner as in the segregated algorithm. Second order upwind scheme is utilized for all, except for pressure where PRESTO! is used. Pressure staggering option (PRESTO!) calculating pressure on the control volume face to discretize momentum equation rather than interpolating by using cell center values or assuming zero pressure gradient at the wall boundary layer **[54]**. Therefore, this discretization scheme giving more accurate results by avoiding interpolation errors and boundary layer assumptions; and recommendable for strong body forces (swirl) on the boundaries as in our case. Computational domain is formed between adiabatic rotating and stationary walls with no slip shear condition. For roughened cases, roughness values are given directly by roughness height through wall roughness option which will be mentioned later in detail. Mass flow rate and total temperature of the air is given as inlet boundary conditions while static pressure given as outlet by setting the reference pressure to zero. Full-multi grid initialization is used, in which Euler equations solved starting from coarse to fine grid and then setting the solution as an initial rather than providing constant initial conditions. The benefit of this method is accelerated convergences. Core rotation swirls are monitored through simulations, which was the parameter that converged last especially for low throughflow rate cases. Unless otherwise stated, a numerical setup is as given in **Table 4.2**.

Table 4.2: CFD model setup.

Coordinate System	2D Axisymmetric swirl
Fluid - Air	Density : Ideal gas Specific Heat (Cp) : Piecewise-polynomial Viscosity : Sutherland
Reference Pressure	0 Pa
Turbulence Model	k-ω SST
Discretization Schemes	Pressure – Velocity Coupling : Coupled Gradient : Least-Squares Cell Based Pressure : PRESTO! Density : Second Order Upwind Momentum : Second Order Upwind Swirl Velocity : Second Order Upwind Turbulent Kinetic Energy : Second Order Upwind Specific Dissipation Rate : Second Order Upwind Energy : Second Order Upwind
Wall BC's	Rotating and stationary adiabatic walls with no slip shear condition
Inlet BC's	Mass flow inlet and total temperature (%5 turbulent intensity)
Exit BC's	Pressure Outlet
Convergence criteria	10^{-7} for all residuals
Monitoring	Core rotation swirl factor at different radii, exit total temperature, exit mass-weighted average velocity magnitude

4.3. Grid Generation and BC's

The computational grid is formed for our shrouded rotor-stator case with different gap ratios, which is also representing our test rig cases. Fully structured approach used to generate meshes, which is composed from regular quadrilaterals elements. Elements generated gradually from coarse to fine in the domain regions with high gradients close to walls as seen in **Figure 4.1**; also while paying attention to aspect ratios and smoothly growing layers on transition between cells. This approach offers higher accuracy and lower numerical errors through near zero skewness values and one orthogonality over all cavity. A grid independence was made for the largest gap ratio case which will be given later in detail. Multiple grids are generated obeying mentioned quality criteria together with non-uniform grid spacing to ensure that the values of y^+ for the grid points nearest the walls were less than unity.

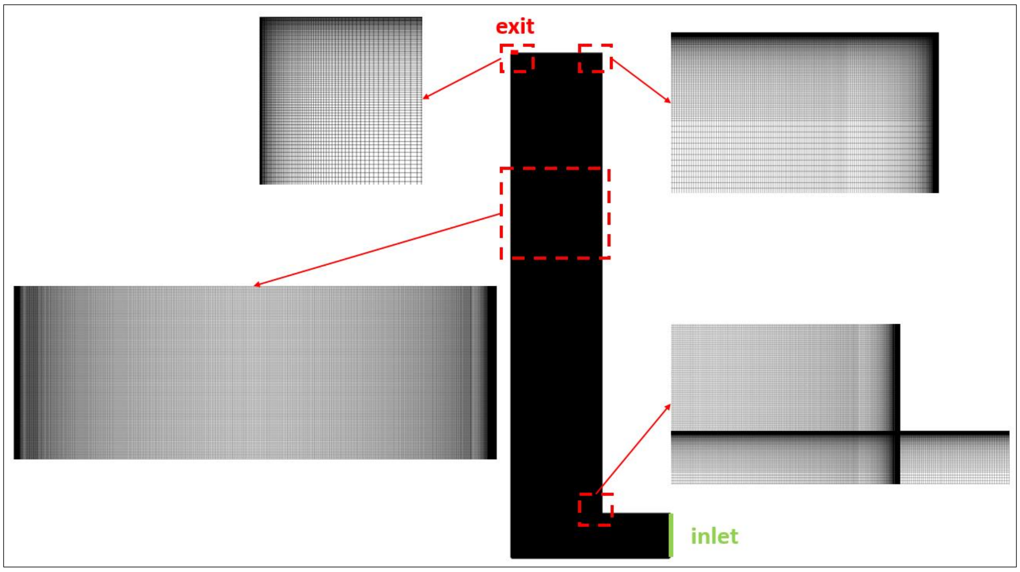

Figure 4.1: Computational grid (fine mesh).

The computational domain is formed between adiabatic rotating disk and stationary shrouded casing as illustrated in **Figure 4.2**, which also giving the details of the boundary conditions types imposed on the model. Mass flow rate and total temperature values for non-pre-swirl throughflow are specified; while in terms of turbulence, intensity values (5%) with hydraulic diameters also given at the inlet. Static pressure boundary condition is applied at the outlet directly by setting reference pressure to zero.

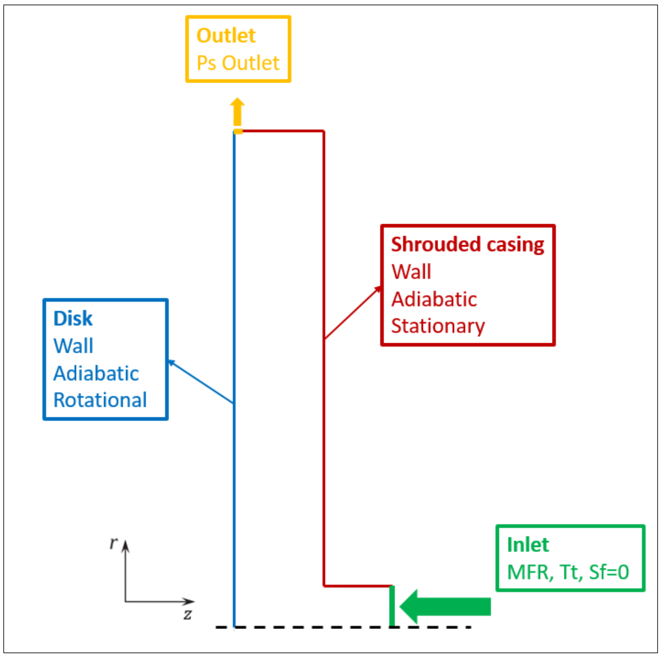

Figure 4.2: Computational domain and boundary conditions.

4.4. Mesh Independence

One of the most time-consuming step in the CFD simulation is the generation of meshes for the computational domains. The quality of the meshes has a significant impact on both convergence and the accuracy of the results. In this thesis, structured meshes are generated for all simulation models with Ansys Meshing as mentioned on previous section. A grid independence study was set for the largest gap ratio case which corresponding to $G = 0.18$. Bulk cavity swirl factor at $x = 0.8$ is drawn against cell count in **Figure 4.3** for $Re_\theta = 4.15 \times 10^6$and $C_w = 33000$ which corresponding to $\lambda_t = 0.168$. Cell count of about 1 million is considered to be enough to capture bulk cavity dynamics therefore is chosen for further study cases.

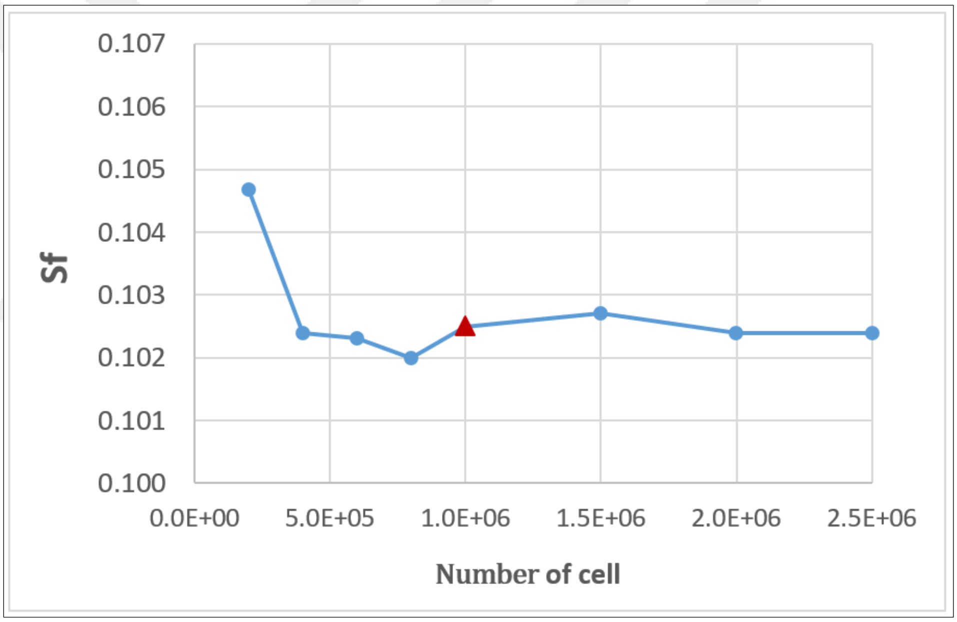

Figure 4.3: Computational grid dependency study for $G = 0.18$ and $\lambda_t = 0.170$ (core rotation swirl values at x=0.8).

Multiple grids generated from coarse to fine by applying non-uniform grid spacing to ensure that the values of y^+ for the grid points nearest the walls were close to unity. Thus, even with the case in 1 million cell, maximum y^+ values almost equal to 1 as seen in **Table 4.3**. Near unity y^+ (non-dimensional wall distance) values are very important to predict the velocity profile properly on viscous sublayer where highest gradients exists.

Table 4.3: Maximum y^+ values for different grid numbers.

Total cell numbers $(\times 10^6)$	0.2	0.4	0.6	0.8	1.0	1.5	2.0	2.5
Max. y^+	2.44	1.42	1.34	1.27	1.18	1.13	1.10	0.97

4.5. Validation Test Cases

Validation studies was made for two different test cases that representing both high and low windage levels with radial outward flow. One of the test model also representing our test rig case, which will be given in detail later.

4.5.1. Numerical Approach Validation

First validation study made with experimental data of Kilic and Owen **[51]** as low windage case where authors using Laser Doppler Anemometry (LDA) to measure the radial and tangential components of velocity of the air between the disks. The test rig schematic given in **Figure 4.4**, where the disk 762 mm in diameter and could be rotating independently both clockwise and counter clockwise. Results are compared for rotor-stator case only that has gap ratio $G = 0.12$ and at $Re_\theta = 1.1 \times 10^6$ for three throughflow rate where turbulent flow parameters corresponding to 0.0572, 0.0889 and 0.142 respectively.

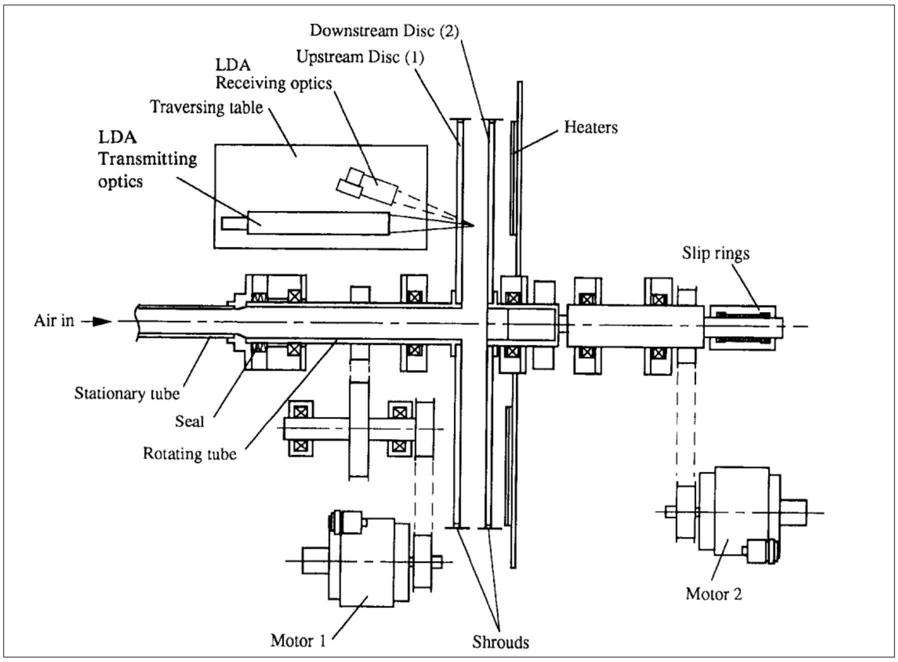

Figure 4.4: Test rig schematic **[50]**.

In **Figure 4.5**, and **Figure 4.6**, the results from numerical simulations for swirl factors and non-dimensionalized radial velocities at $x = 0.8$ are compared with those from LDA measurements by Kilic and Owen **[51]**, respectively, for three different throughflow rate. The results of the simulations and the measurements are in an acceptable agreement on predicting radial and tangential velocities in core rotation and comparison showing that simulation setup should be reasonable for low windage cases.

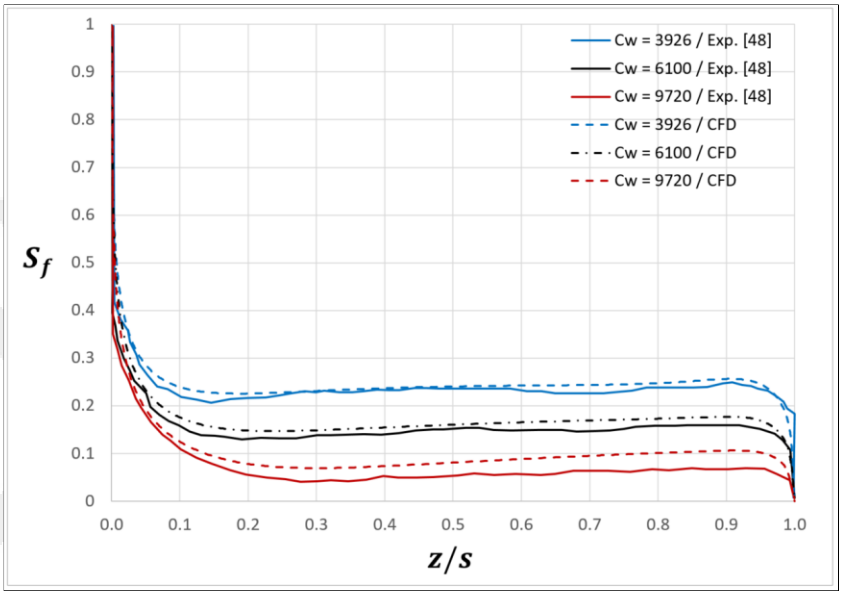

Figure 4.5: Axial distribution of the swirl factor at $x = 0.8$ for $Re_\theta = 1.1 \times 10^6$.

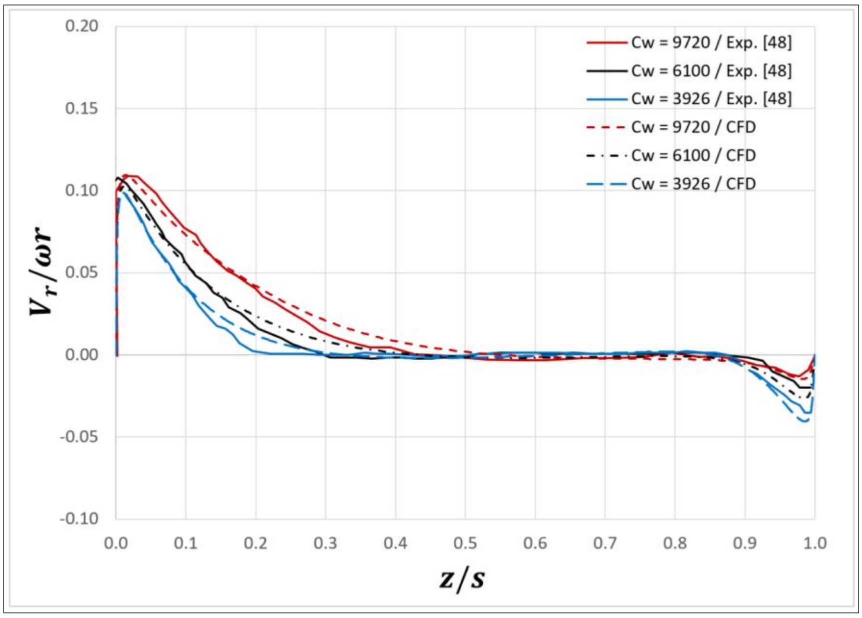

Figure 4.6: Axial distribution of non-dimensional radial velocities at $x = 0.8$ for $Re_\theta = 1.1 \times 10^6$.

4.5.2. Validation of Test Rig Case

Second validation study made with experimental data of Tao et al. **[55]** as high windage case, where authors using Particle Image Velocimetry (PIV) to measure the tangential components of the rotating core in the rotor-stator cavity. The setup is given in **Figure 4.7**, where the disk 450 mm in diameter and PIV measurements was taken in the middle-plane ($z/s = 0.5$) between rotor and stator with CCD camera from the plexiglass window opened on the stationary shrouded casing side. Results are compared at gap ratio $G = 0.18$ for two different Reynolds numbers $Re_\theta = 4.2 \times 10^6$ and $Re_\theta = 2.8 \times 10^6$, respectively, for three throughflow rate where turbulent flow parameters ranging from 0.034 to 0.236.

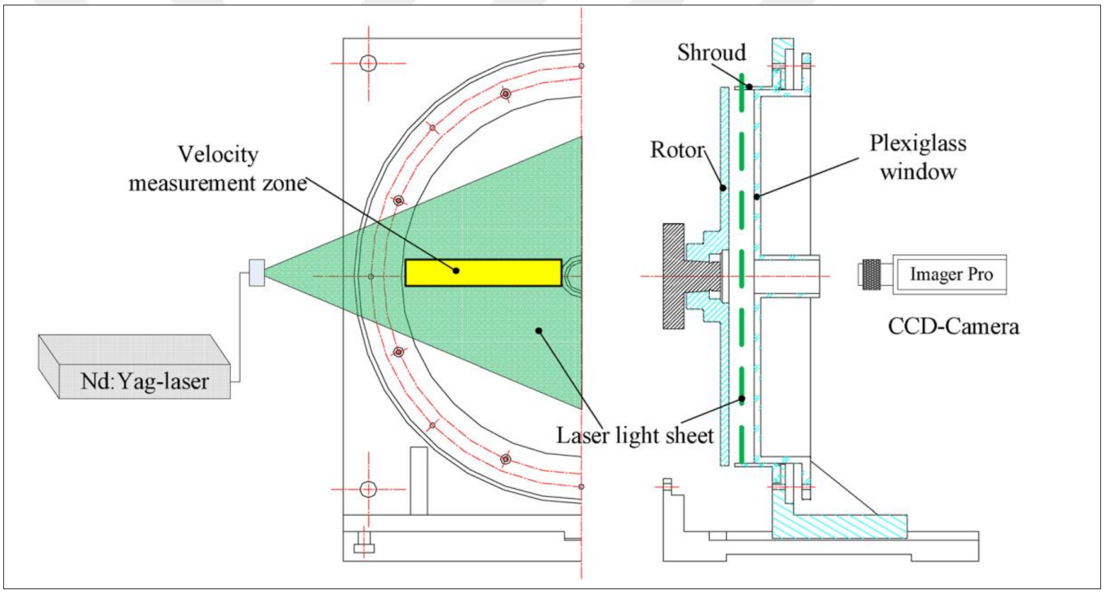

Figure 4.7: PIV setup of the rig **[55]**.

In **Figure 4.8**, and **Figure 4.9**, the numerical simulations are compared with PIV measurements taken by Tao et al. **[55]** for the radial distribution of tangential velocities at mid-span cavity ($z/s = 0.5$) from x=0.19 to 0.89, at $Re_\theta = 4.2 \times 10^6$ and $Re_\theta = 2.8 \times 10^6$, respectively, for three different throughflow rate. The results of the simulations and the measurements are in good agreement for most of the cases. The comparison showing that simulation setup also giving acceptable results for high windage cases.

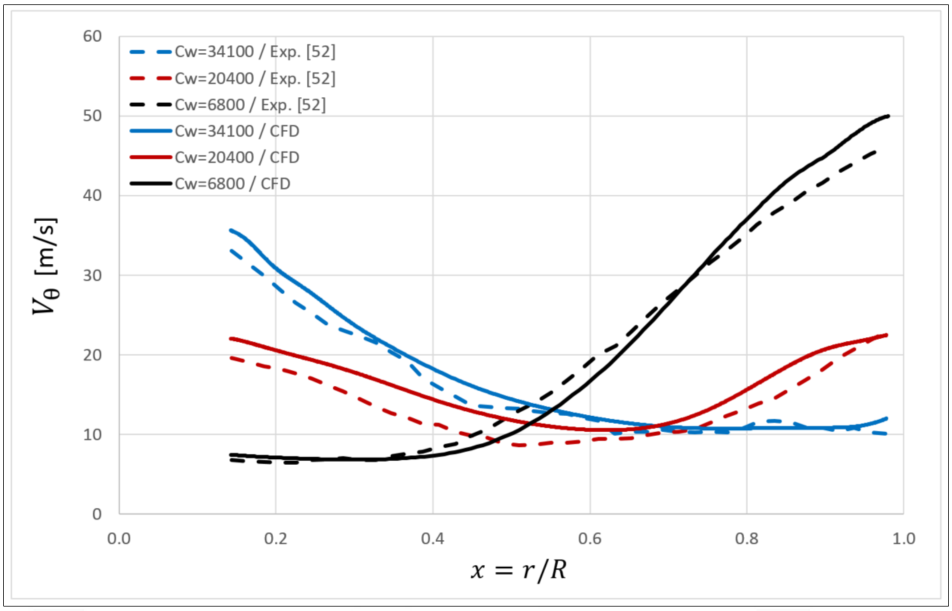

Figure 4.8: Radial distribution of the tangential velocities at mid-span ($z/s = 0.5$) for $Re_\theta = 2.8 \times 10^6$.

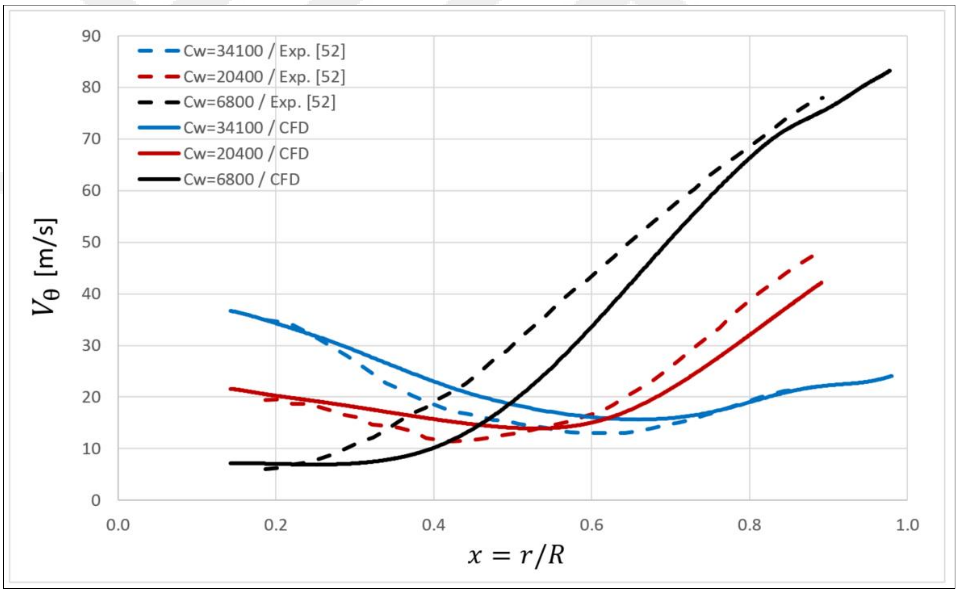

Figure 4.9: Radial distribution of the tangential velocities at mid-span ($z/s = 0.5$) for $Re_\theta = 4.2 \times 10^6$.

In **Figure 4.9**, only the lowest throughflow case gives results that are far from the test data. For this reason, a full 3D model (not a sector) was also performed with the same setup used in the publication as authors. However, the results were very close to the 2D axisymmetric cases, and in fact were almost identical. On this occasion, although 3D is a prominent necessity when there is non-symmetric futures or 3D effects, the 2D axisymmetric model was found to be quite advantageous compared to 3D in terms of computational cost and effort, of course, if all futures are axisymmetric as in our case.

4.6. Smooth Disk and Casing Results

4.6.1. Existence of Core Rotation

All our theoretical analysis actually depends on the existence of core rotation together with its swirl factor which is the key parameter for heat transfer, windage generated, static pressure increase/decrease and also the pumping flow in the cavity. One thing for sure, superposed flow rate, no matter how much is it, will suppress the core rotation (for radial outward flow) and decrease the core rotation swirl as long as it enters from the center of the cavity with zero swirl as in our case; and can even bring an end to its existence if the amount is high enough. However, a general misunderstanding about the concept is that if the amount of the superposed flow is higher than the amount of disk pumping need or free disk pumping rate, core rotation would be suppressed completely and will not exist.

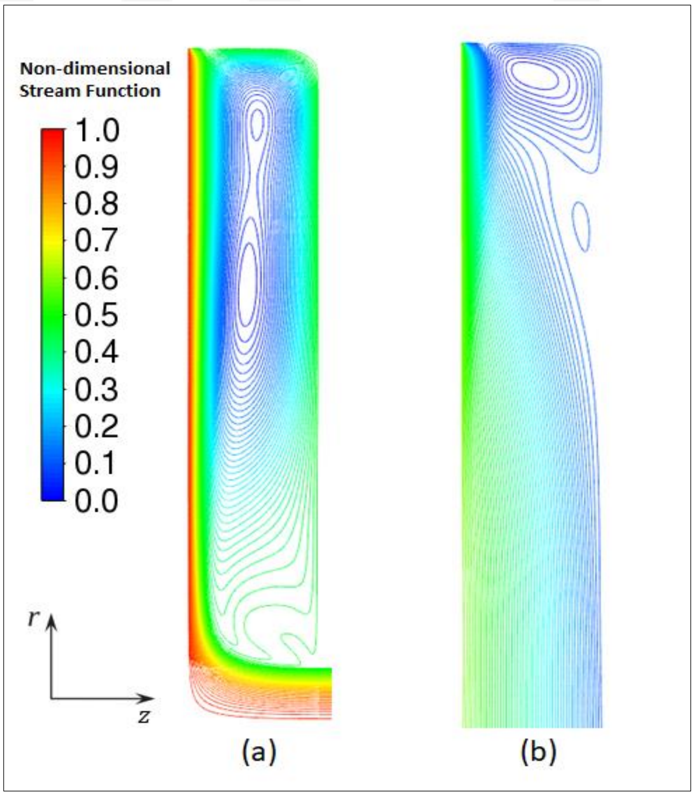

Figure 4.10: Effects of inlet flow condition on core rotation for $Re_\theta = 2.6 \times 10^6$, $C_w = 3.3 \times 10^4$, $G = 0.18$, $\lambda_t = 0.243$; a) axial inlet b) radial inlet.

Figure 4.10 actually proves that is not true and the throughflow rate is not a single parameter for the existence of the core rotation. In figure, the turbulent flow parameter values are same for both radial and axial inlet cases and greater than 0.219 ($\lambda_t > 0.219$) which meaning that the amount of flow rates introduced into the cavities are even higher than the free disk pumping value which is corresponding to 0.219 for 7-th power law profile. Yet in **Figure 4.10**, even for radial inlet case, although its formation supported by shroud, there is still a core rotation at high radii; and actually for the axial inlet in **Figure 4.10**, as a contrary to general belief, whole cavity dominated by the core rotation. Therefore, how the throughflow conditions into the cavity is important as indeed is the amount of it entering the cavity; and the existence of the core rotation does not depend directly on the pumping flow rate.

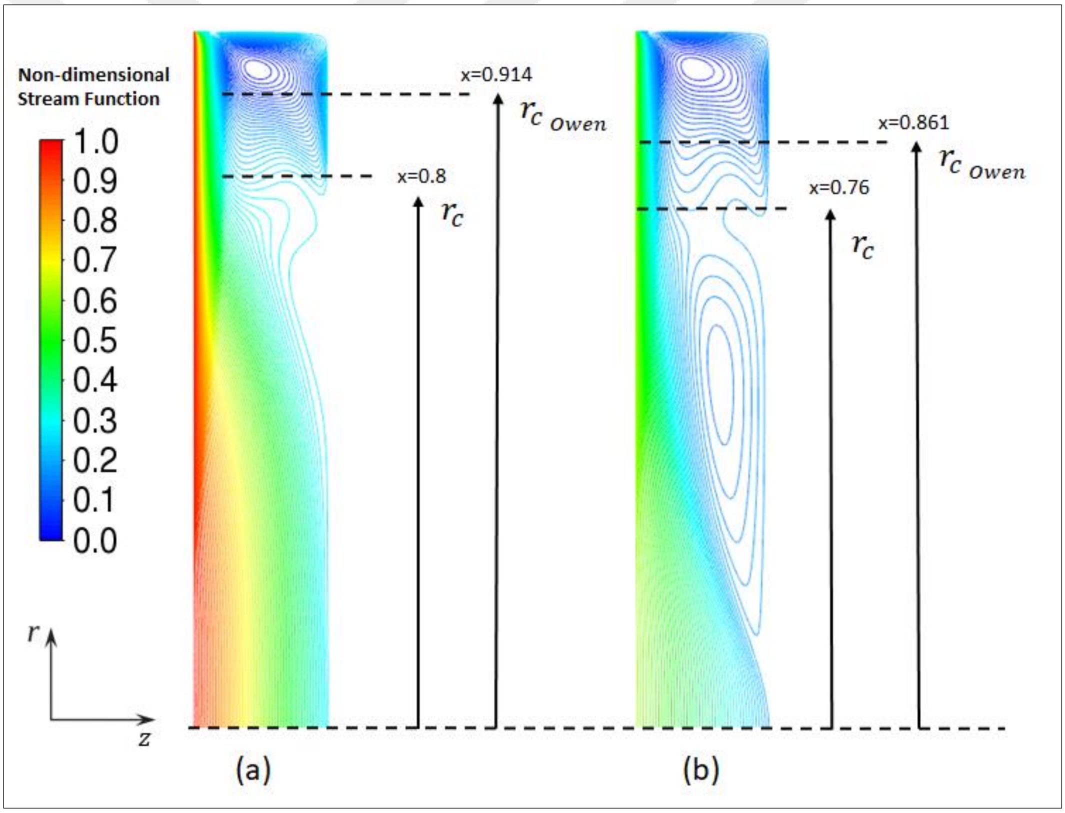

Figure 4.11: Radius at which “source region” ends and “core rotation” begins for radial inlet cases, $G = 0.18$; a) $\lambda_t = 0.173$, b) $\lambda_t = 0.151$.

For radial inlet cases, if superposed flow introduced into the cavity lower than “free disk” pumping value, according to Owen **[22]** source region will end and core rotation at the local radius where local “free disk” pumping value equal to throughflow rate.

However as shown in **Figure 4.11**, Owen's approach underestimating the radius where the core region starts.

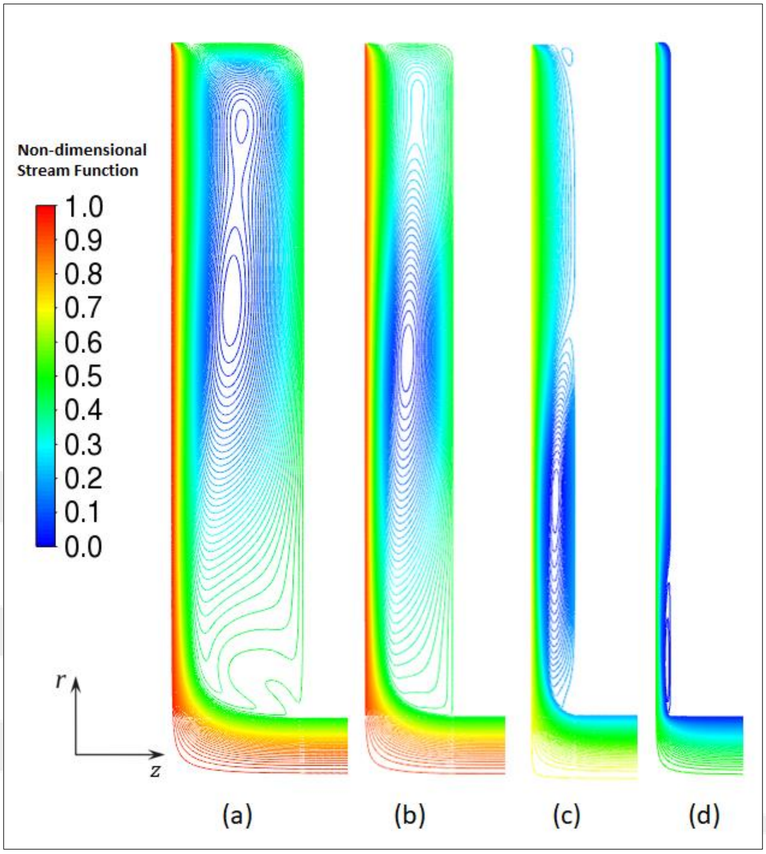

Figure 4.12: Effects of gap ratio on core rotation for $Re_\theta = 2.6 \times 10^6$, $C_w = 3.3 \times 10^4$, $\lambda_t = 0.243$; a) $G = 0.18$, b) $G = 0.12$, c) $G = 0.06$, d) $G = 0.02$.

In **Figure 4.12**, high λ_t case again evaluated for different gap ratios. One can see how gap ratio suppressing the core rotation in a much more dominant way as moving from largest to smaller gaps, and results in almost no core rotation at all for the smallest gap ratio $G = 0.02$ as we expect. Thus, it can noted once again as long as gaps are big enough to allow two separate boundary layer on rotor and stator, there will be a core rotation between. For real gas turbine applications also, all rotor-stator cavity flows, generally, flowing through rotating and stationary disk boundaries as in our case and most of the time there is an enough gap to form core rotation between.

However, as the gap becomes smaller, no longer expected to have separated but a single boundary layer shearing from disk speed, ωr to zero on the stationary casing side as in **Figure 4.13**, which are swirl factors at different radii inside the cavity plotted for the same $\lambda_t = 0.243$ case with smallest gap ratio $G = 0.02$. Showing typical Stewartson type of flow structure as we remember from **Figure 2.16**.

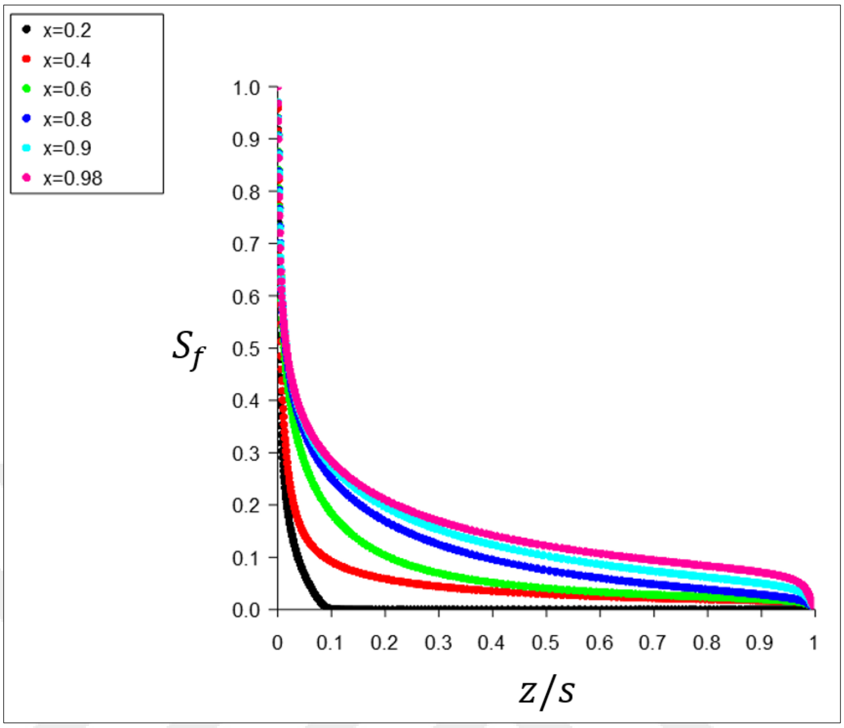

Figure 4.13: Axial distributions of swirl factors at different radii for $Re_\theta = 2.6 \times 10^6$, $C_w = 3.3 \times 10^4$, $\lambda_t = 0.243$, $G = 0.02$.

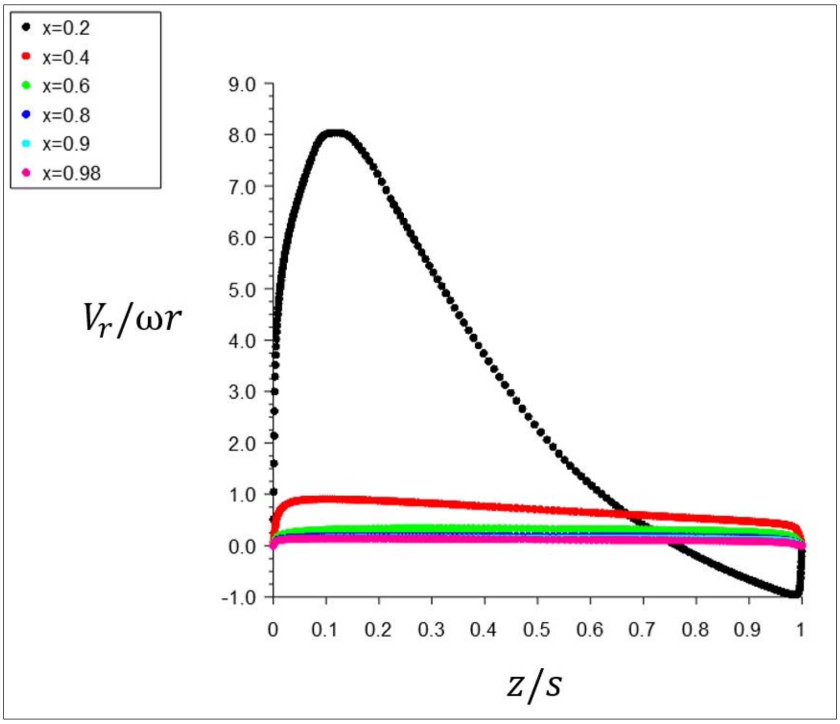

Figure 4.14: Axial distributions of non-dimensional radial velocities at different radii for $Re_\theta = 2.6 \times 10^6$, $C_w = 3.3 \times 10^4$, $\lambda_t = 0.243$, $G = 0.02$.

In **Figure 4.14**, non-dimensionalized radial velocities also plotted for the same gap ratio case, except the effect of inlet turning and small core formation at $x = 0.2$, plot showing again the typical velocity profile for the Stewartson type of flow structure as expected.

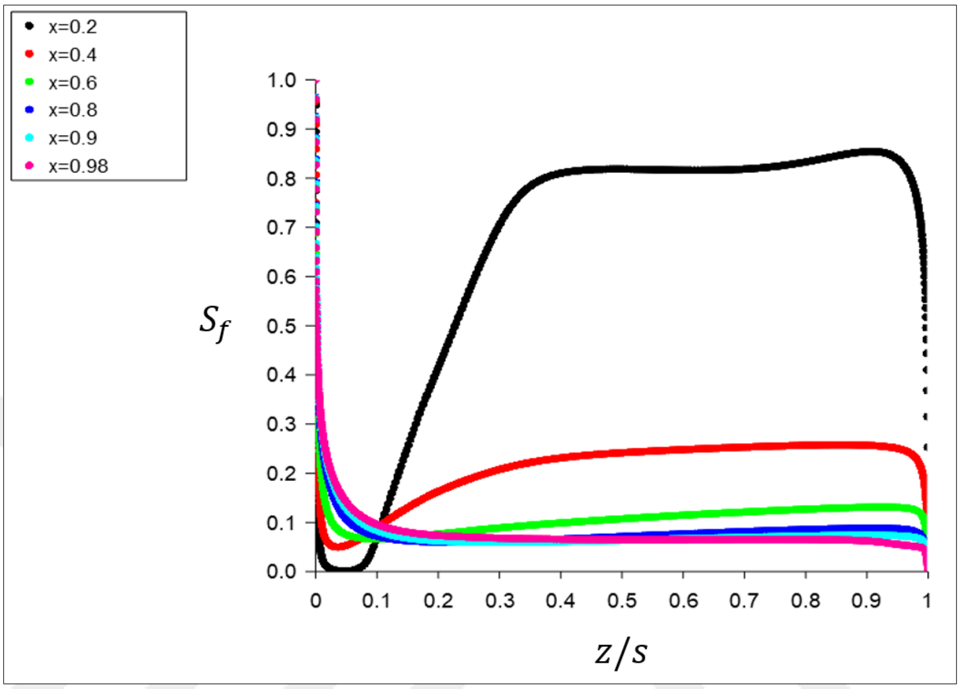

Figure 4.15: Axial distributions of swirl factors at different radii for $Re_\theta = 2.6 \times 10^6$, $C_w = 3.3 \times 10^4$, $\lambda_t = 0.243$, $G = 0.18$.

In **Figure 4.15**, swirl factors plotted for the largest gap ratio $G = 0.18$ and now separate boundary layers visible on both on rotor and stator sides what we known as Batchelor type of flow structure. On the rotor side, draw attention to growing boundary layer thickness with increasing radii. However, on the stator side, there is almost no difference but in fact a small boundary layer growth in the opposite (radially inward) direction as being very interestingly. This might be due to the increased velocity gradients on core rotation side at lower radii; and the reasoning for this, core rotation actually starting to behave like a free vortex from around $x = 0.6$ to lower radii but at higher radius, with increased torques, a completely forced vortex with almost constant swirl factor as shown in **Figure 4.16**.

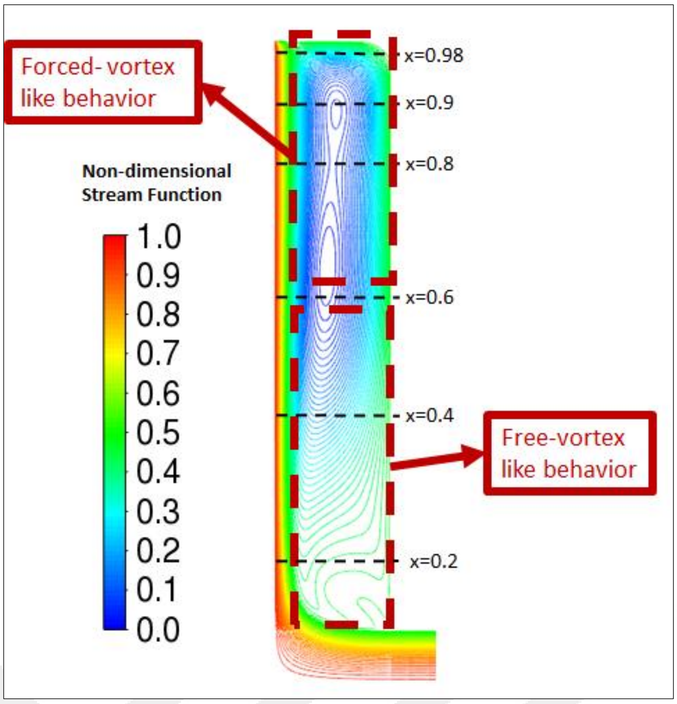

Figure 4.16: Core rotation flow types for $Re_\theta = 2.6 \times 10^6$, $C_w = 3.3 \times 10^4$, $\lambda_t = 0.243$, $G = 0.18$.

If we remember the fact that core rotation continuously being fed from the radially inward flow along the stator and axially from the stator boundary layer to the rotor boundary layer. At lower radii, core rotation’s own momentum that being fed from radially inward flow becoming dominant against low torques and starting to behave like a free vortex increasing its swirl with decreasing radius.

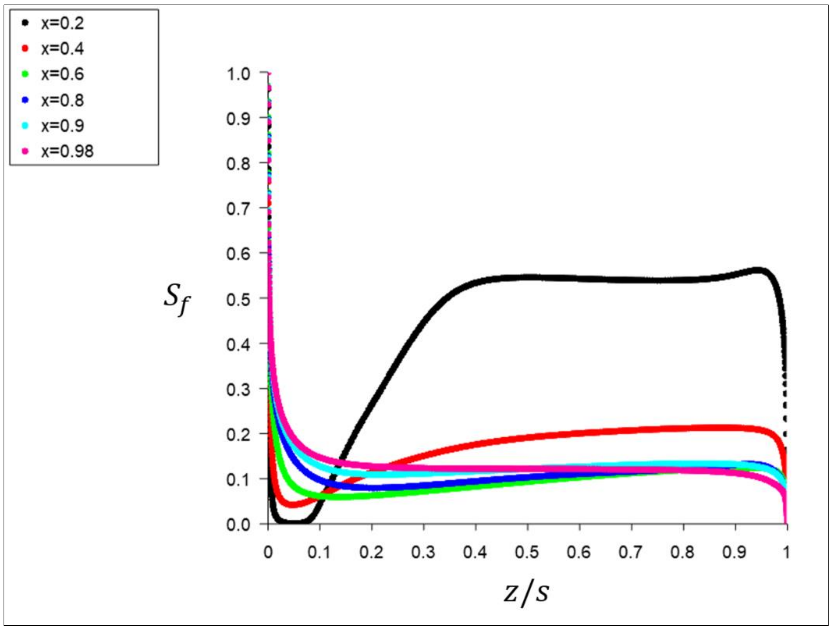

Figure 4.17: Axial distributions of swirl factors at different radii for $Re_\theta = 2.6 \times 10^6$, $C_w = 2.04 \times 10^4$, $\lambda_t = 0.151$, $G = 0.18$.

If we decrease the amount of throughflow introduced into the cavity, since the momentum entering the cavity itself decreases, torque of the disk now more dominant for the core rotation at lower radii and although free vortex behavior still exist but decreased a bit as shown in **Figure 4.17**. At same non-dimensional radius, $x = 0.2$ core rotation swirl value decreasing from about 0.8 for $\lambda_t = 0.243$ to 0.5 for $\lambda_t = 0.154$ case. On the other hand, at higher radii, core rotation now forced to slightly higher swirl values as we expect.

With further decrease in throughflow rate for the same Reynolds case, now free vortex like behavior completely vanished as can be seen from **Figure 4.18**; at lower radii almost forced to lower swirl value and at higher radii core rotation to much higher swirl values.

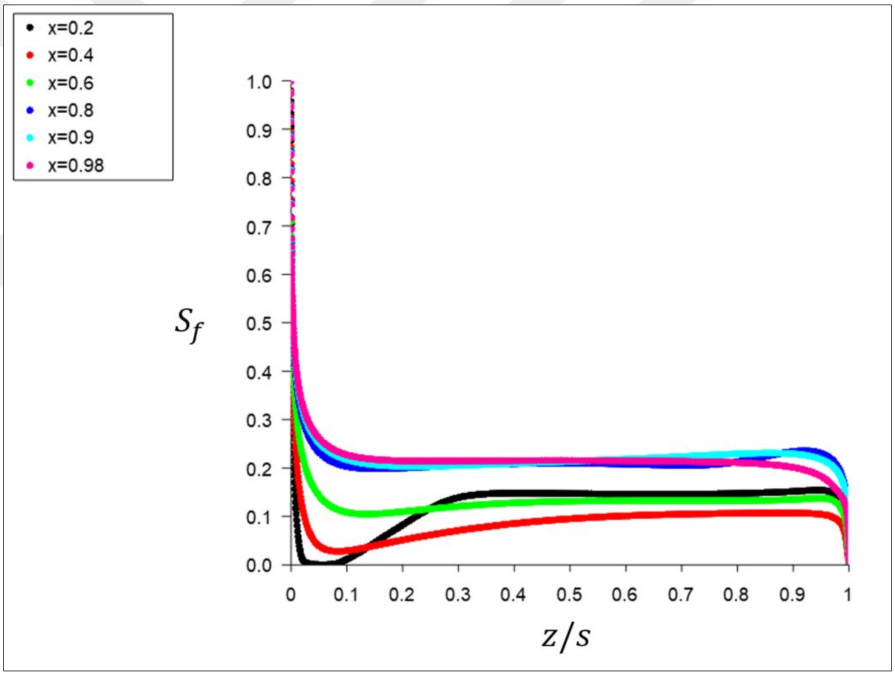

Figure 4.18: Axial distributions of swirl factors at different radii for $Re_\theta = 2.6 \times 10^6$, $C_w = 0.66 \times 10^4$, $\lambda_t = 0.05$, $G = 0.18$.

However, in this case $\lambda_t = 0.05$, the amount of flow introduced into the cavity is now much lower than the disk pumping value. For such cases, it is known that ingestion into the cavity can occur from surroundings due to the phenomenon known as "Rotationally Induced Ingress". Bayley and Owen **[56]**, carried out an experimental study with an almost identical shrouded rotor-stator cavity to ours, using pressure measurements to determine the minimum throughflow to prevent ingestion for the case of a simple axial clearance as in our case with clearance ratios $G_c = 0.0033$ and 0.0067 for values of Re_θ up to 4×10^6. According to their correlation ($C_{w,min} = 0.61 G_c Re_\theta$), for our $\lambda_t = 0.05$ case, the minimum sealing flow to prevent ingestion corresponding to $C_{w,min} = 0.7 \times 10^4$, while we are sending less amount, and in fact ingestion could occur. However, we cannot account for ingestion in our 2D CFD model where we have only one inlet and outlet, which always converges to the inlet mass flow rate at outlet, in accordance with mass conservation. Therefore, although this low throughflow case has converged and has a solution, it doesn't mean that it represents the real case. Some unsteady flow structures can even occur where in our model, we are taking steady-state results only and don't take into account any unsteadiness. Therefore, using CFD for this much low throughflow cases with current steady-state 2D axisymmetric swirl approach, the results are always questionable in my opinion.

4.6.2. Windage Results

The effect of gap ratio effect on windage power loss is complex when throughflow is introduced, and it does not have a simple explanation just like in enclosed cavity cases revealed by Daily and Nece **[19]**. However, its effect also seems negligible compared to throughflow effect.

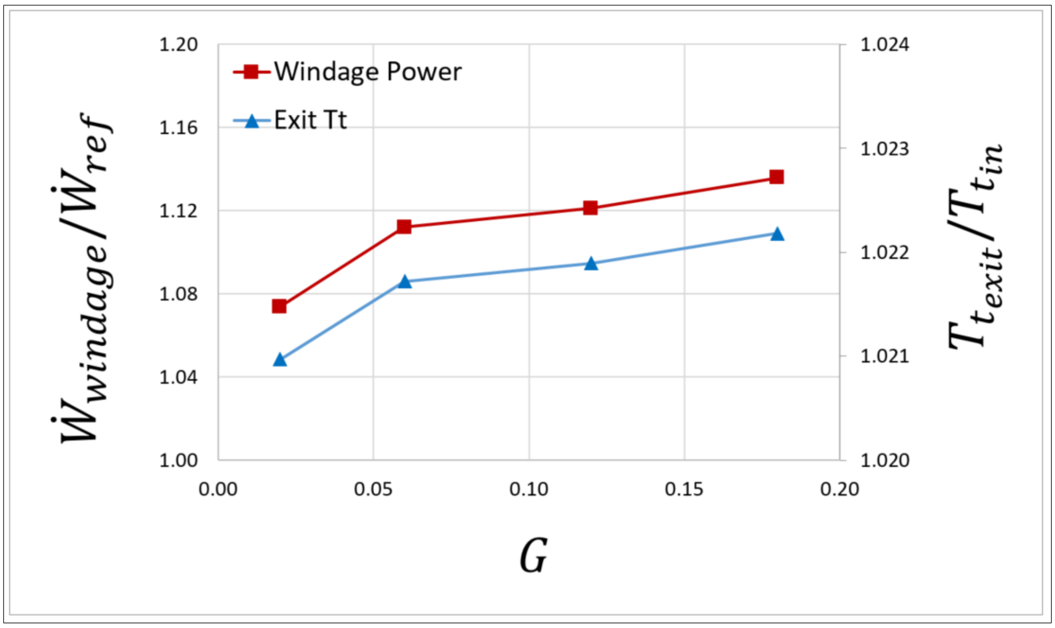

Figure 4.19: Gap ratio effect on windage power and resultant exit total temperature for $Re_\theta = 2.6 \times 10^6$, $C_w = 3.3 \times 10^4$, $\lambda_t = 0.243$.

In **Figure 4.19**, windage power loss and resultant exit total temperature of the air are compared for all gap ratios at same rotational Reynolds number (the lowest case). As the gap ratio decreases from $G = 0.18$ to $G = 0.02$, the core rotation occurring at lower radii is suppressed resulting in lower swirl ratio values; however, more importantly, at higher radii where the most of the windage power loss coming from, higher swirl factors are attained as seen in **Figure 4.20**. Therefore, windage power increases slightly as the gap ratio increases, not significantly though and resultant temperature rise is rather small but of course, this rise depends on the superposed flow rate.

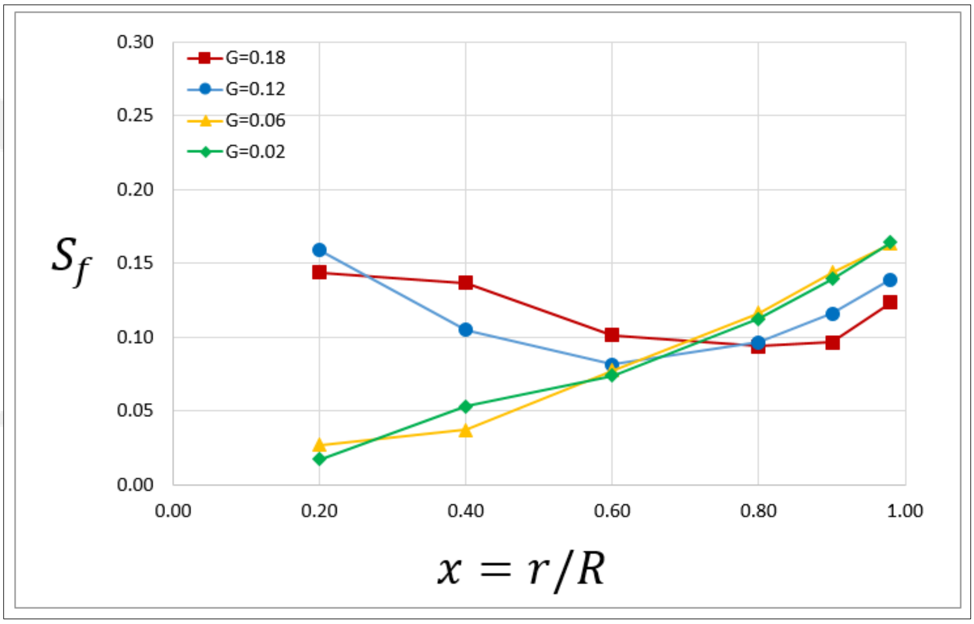

Figure 4.20: Gap ratio effects on radial distribution of swirl factors for $Re_\theta = 2.6 \times 10^6$, $C_w = 3.3 \times 10^4$, $\lambda_t = 0.243$.

For the highest rotational Reynolds number case in **Figure 4.21**, the observed trend is slightly different around $G = 0.12$. For the gap ratio of 0.06, windage power becomes slightly higher than $G = 0.12$, not showing consistent decrease or increase. According to findings of Daily and Nece **[19]**, without throughflow, windage power decreases with increasing gap ratio for merged boundary layers (Regime III); in contrast, increases with raising gap width in case of separated boundary layers (Regime IV) due to braking influence of cavity, approaching to case of a "free disk", which represents the maximum resistance.

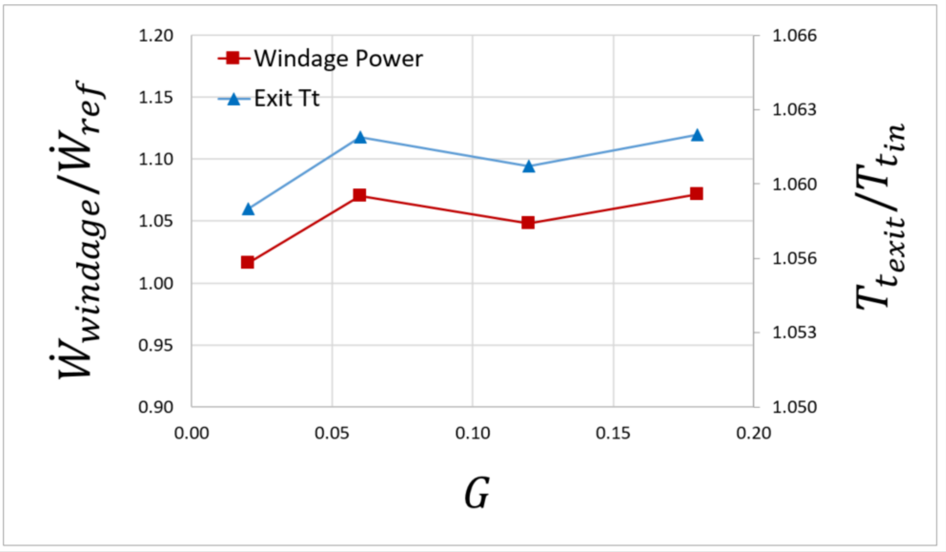

Figure 4.21: Gap ratio effect on windage power and resultant exit total temperature for $Re_\theta = 4 \times 10^6$, $C_w = 3.3 \times 10^4$, $\lambda_t = 0.173$.

However, when superposed flow is introduced into the cavity, this issue becomes more complex. Since additional flow with linear momentum injected into the cavity, and decreasing gap ratio also changing the effect of this throughflow over all cavity flow structure as discussed in previous section. In **Figure 4.22**, radial swirl distribution is given for high windage case. Since torques coming from either walls increase, swirl ratio values are forced to slightly higher values but reaction to gap ratios nearly same as the low windage case and windage power is not even changing 10 percent from the largest width to the smallest. Collapsing of data for medium to high gap ratios implies the independence of flow field to gap ratio.

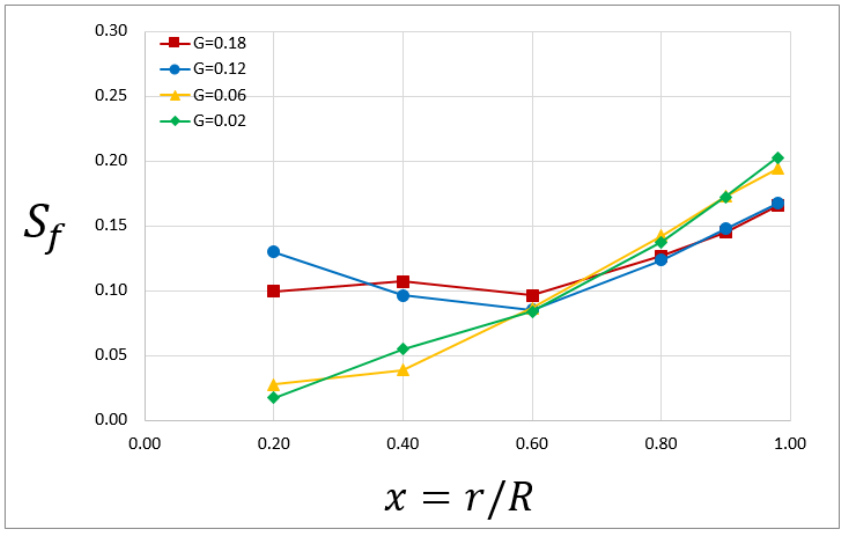

Figure 4.22: Gap ratio effects on radial distribution of swirl factors for $Re_\theta = 4 \times 10^6$, $C_w = 3.3 \times 10^4$, $\lambda_t = 0.173$.

More importantly, examining **Figure 4.23** and **Figure 4.24** in detail; throughflow effect is compared for three different flow rates for the same rotational Reynolds number, and it can be easily deduced that throughflow is much more of a significant parameter on windage generation than gap ratio. Windage losses are increasing as the amount of superposed flow increases; meaning that using more flow budget and getting more power loss. However, when flow rate is reduced, exit temperature is increasing since the amount of exposed to windage power is also reduced. As throughflow increases, suppression of core rotation occurs that results in decreasing overall swirl distribution inside the cavity in a very dominate way compared to gap ratio. At higher radii, swirl factors decrease from around 0.25 to around 0.1 from lowest to the highest flow respectively, which means more tangential velocity gradient, hence more windage generation. Essentially, higher λ_t implies flow character akin to a free vortex behavior, which results in significantly reduced swirl ratio with increasing radius that increases rotor torque and decreases stator torque respectively. However, reduction of swirl ratio is associated with higher flow rate based on angular momentum equation despite rising net torque. Therefore, the optimization of flow rate is essential as it brings not one but two advantages, less performance penalty with less windage loss.

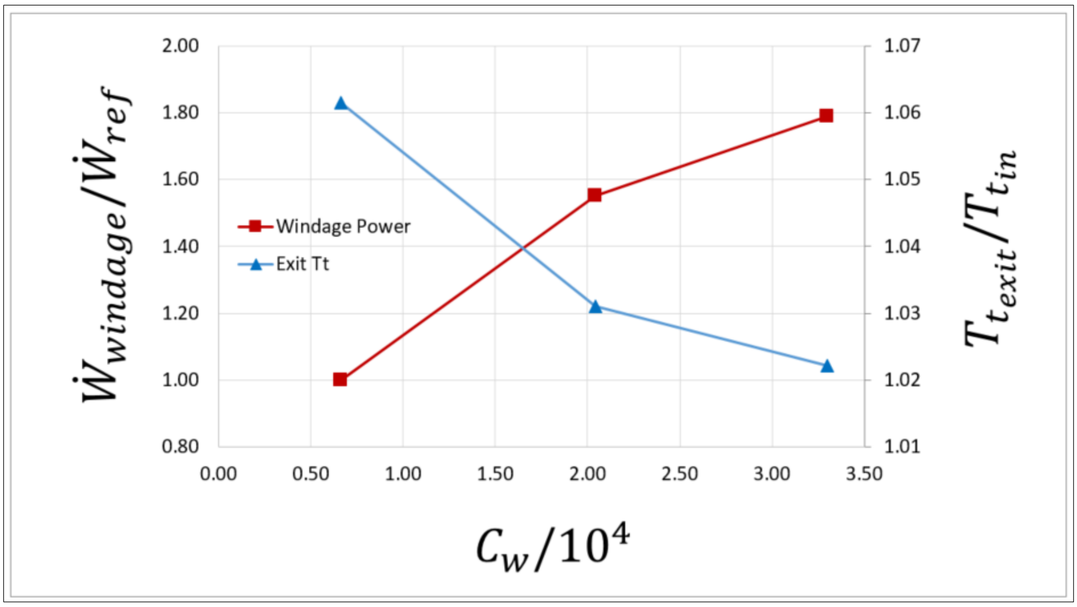

Figure 4.23: Throughflow effect on windage power and resultant exit total temperature for $Re_\theta = 2.6 \times 10^6$ corresponding to $\lambda_t = 0.05, 0.15\ and\ 0.24$

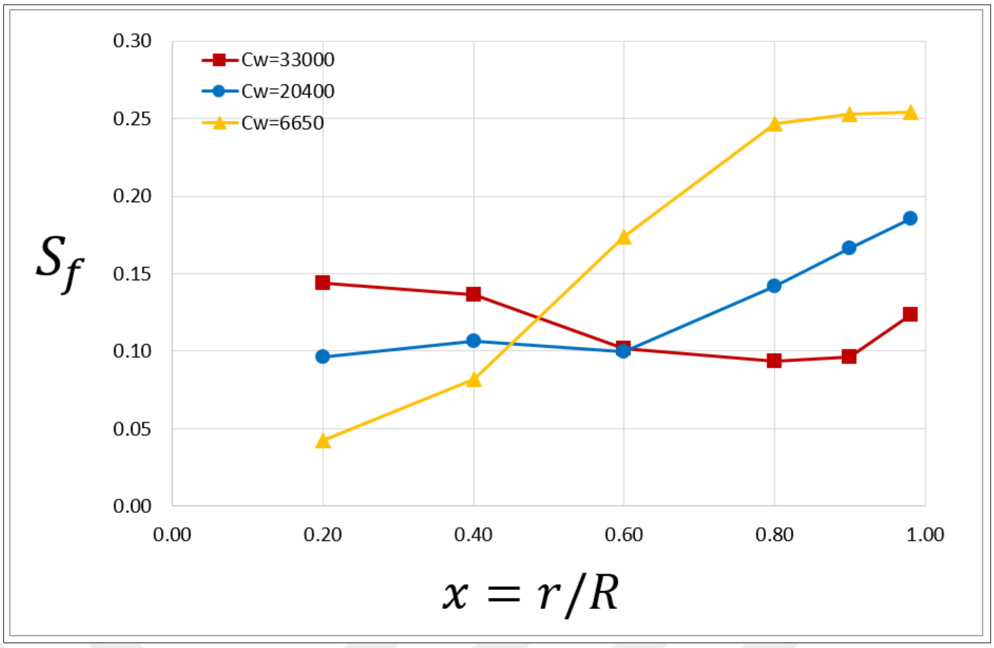

Figure 4.24: Throughflow effects on radial distribution of swirl factors for $Re_\theta = 2.6 \times 10^6$ corresponding to $\lambda_t = 0.05, 0.15\ and\ 0.24$

For the highest rotational Reynolds number case, swirl ratio distributions are given for different throughflow rates in **Figure 4.25**, and it seems that behavior is the same but now the heating is much more significant as expected. Windage power is almost doubling between highest and lowest flow rates but there is of course more significant temperature rise. Since windage power is transferred to superposed flow eventually, it would lead to an increase in the metal temperatures and consequent degradation of the parts, shortening the fatigue and creep life; in real gas turbine applications. Therefore, establishing the minimum cavity flows with acceptable windage temperature rise is essential and critical to the service life of many turbine components that support blades and vanes.

In **Figure 4.26**, same behavior for the radial distribution of swirl factors can be seen throughout the cavity. Overall swirl factors as well as the difference between different throughflow rates are increased due to higher torques exerted at higher rotational Reynolds numbers. When we look at the cavity solver results for same cases, it reveals that although net torques are decreasing, swirl factors are increased with decreasing throughflow rates so that windage power losses are also decreasing.

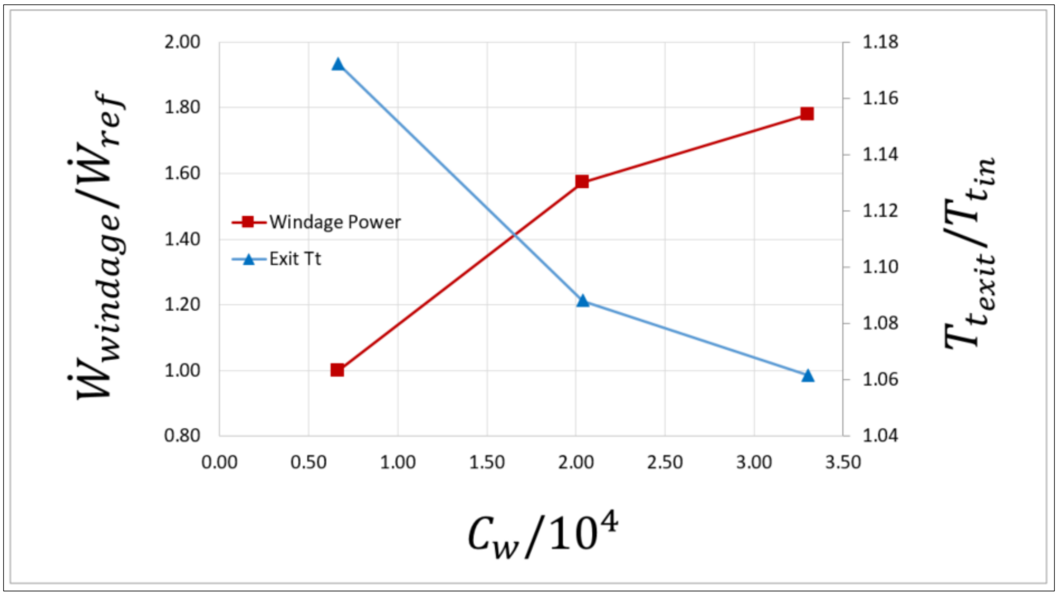

Figure 4.25: Throughflow effect on windage power and resulted exit total temperature for $Re_\theta = 4 \times 10^6$ corresponding to $\lambda_t = 0.035, 0.107\ and\ 0.173$

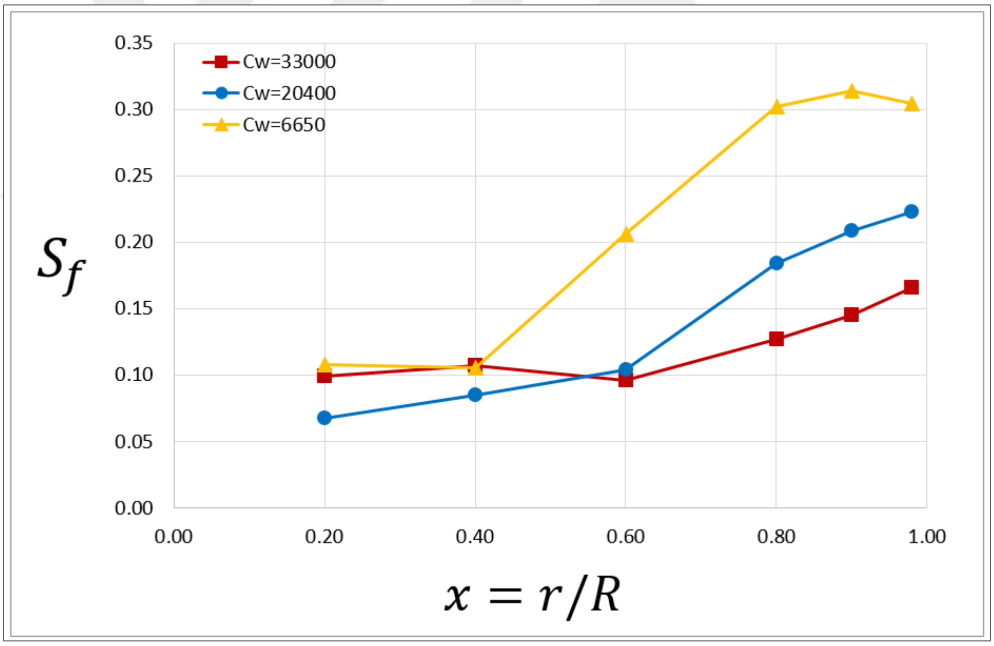

Figure 4.26: Throughflow effects on radial distribution of swirl factors for $Re_\theta = 4 \times 10^6$ corresponding to $\lambda_t = 0.035, 0.107\ and\ 0.173$

In addition, if we compare same throughflow cases for two different rotational Reynolds numbers, swirl ratio values are higher on higher Reynolds number case, windage power loss is not increased exactly as 2.8 times over angular speed, due to reduced λ_t, but to a lower value, owing to increased swirl ratio that is reducing the rotor torque slightly.

As it is known from theory, swirl distributions inside the cavity affect windage generation the most, second to the radius and angular velocity of the disk. Numerical simulations also confirming this outcome and showing the ‘impact of the amount of throughflow on the swirl distributions. Moreover, although gap ratio also has effects on the flow structure inside the cavity, its effect on windage generation is not significant, which is also in line with the experimental findings of Daily and Nece **[19]** (moment coefficient varying with $G^{0.1}$).

4.6.3. Comparison of Results with Theory

All numerical simulation results that corresponding to turbulent flow parameters between $0.034 < \lambda_t < 0.243$ solved with 1D “SOCS design tool” by dividing cavity into 5 sub-cavity and results are compared in terms of swirl factors, windage heating, static pressure distributions and axial load exerted to the disk.

If we start with exit swirl, mass-weighted average of swirl factor at outlet computed from simulation results and compared with cavity solver results in **Figure 4.27**. There is a consistent underestimation for all cases between 7 to 9 percent, which can be considered as acceptable.

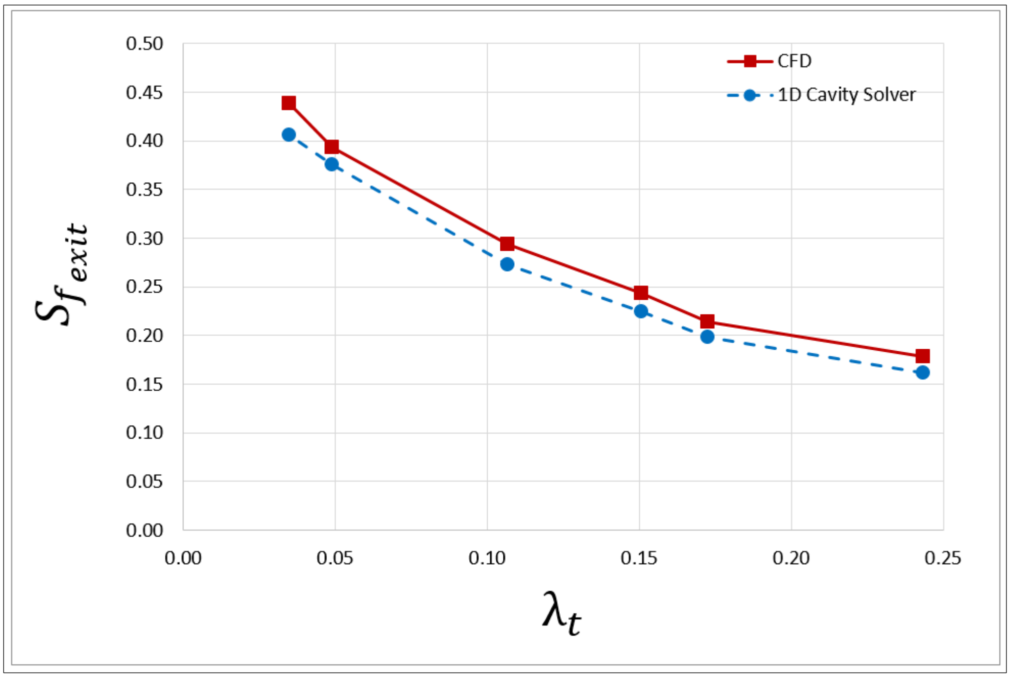

Figure 4.27: Comparison of exit swirl factor by CFD and cavity solver (SOCS Design tool) ($G = 0.18$).

In **Figure 4.28**, mass-weighted average of swirl factors computed at different radii from simulations and compared with Daily's empirical correlation given in equation **(**2.38**)** that derived from experiments. By using $S_{f_0} = 0.5$, Daily's correlation results are in a good agreement with CFD results for high turbulent flow parameters.

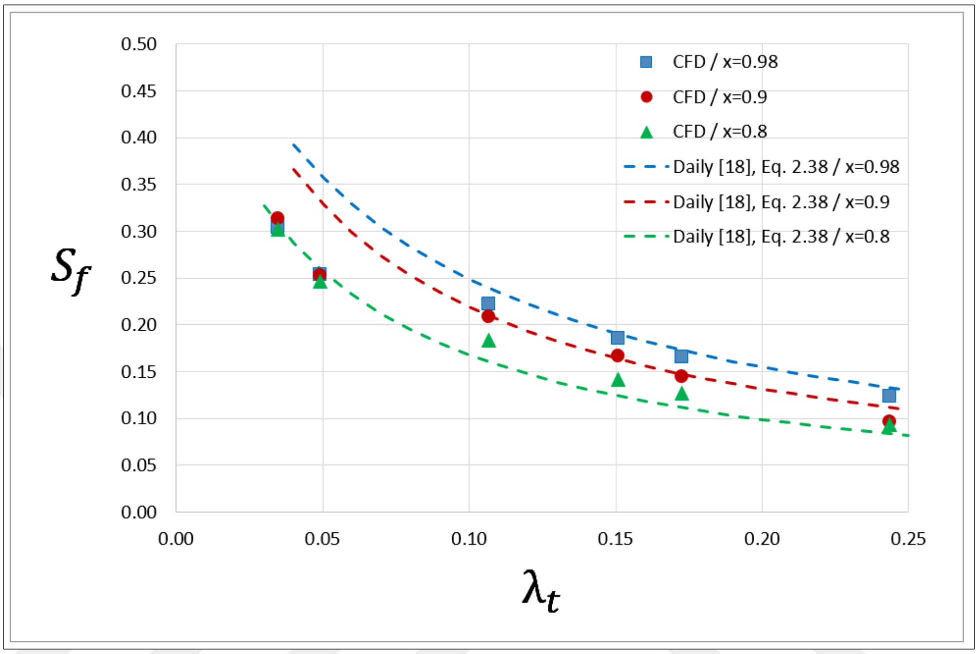

Figure 4.28: Comparison of core rotation swirl factors at different radii by CFD and Daily's empirical correlation ($G = 0.18$).

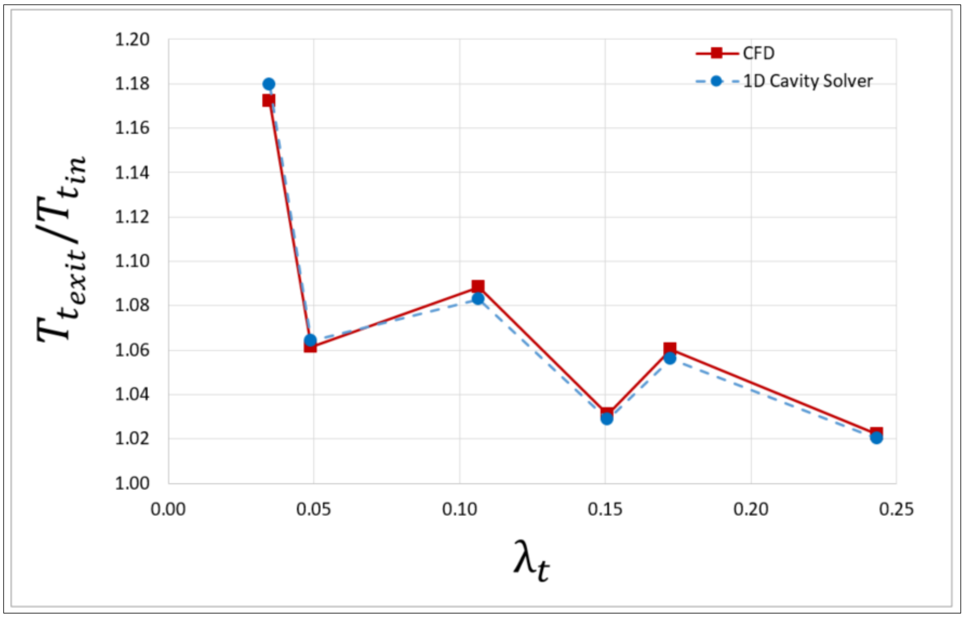

Figure 4.29: Comparison of exit total temperature by CFD and cavity solver (SOCS Design tool) ($G = 0.18$).

If we look at the windage heating results by comparing exit total temperatures, there are not even 1 percent difference between cavity solver and numerical simulations as shown in **Figure 4.29**.

In CFD, cavity outlet pressure given as in Eskisehir condition to obtain comparable inputs to tests so that inlet pressures was always changing in CFD according to throughflow rates. For this reason, the static pressure value at $x = 0.2$ was defined as the inlet pressure to the cavity solver and resulted the static pressures at $x = 0.9$ are compared with CFD results as given in **Figure 4.30**; difference are less than 1 percent.

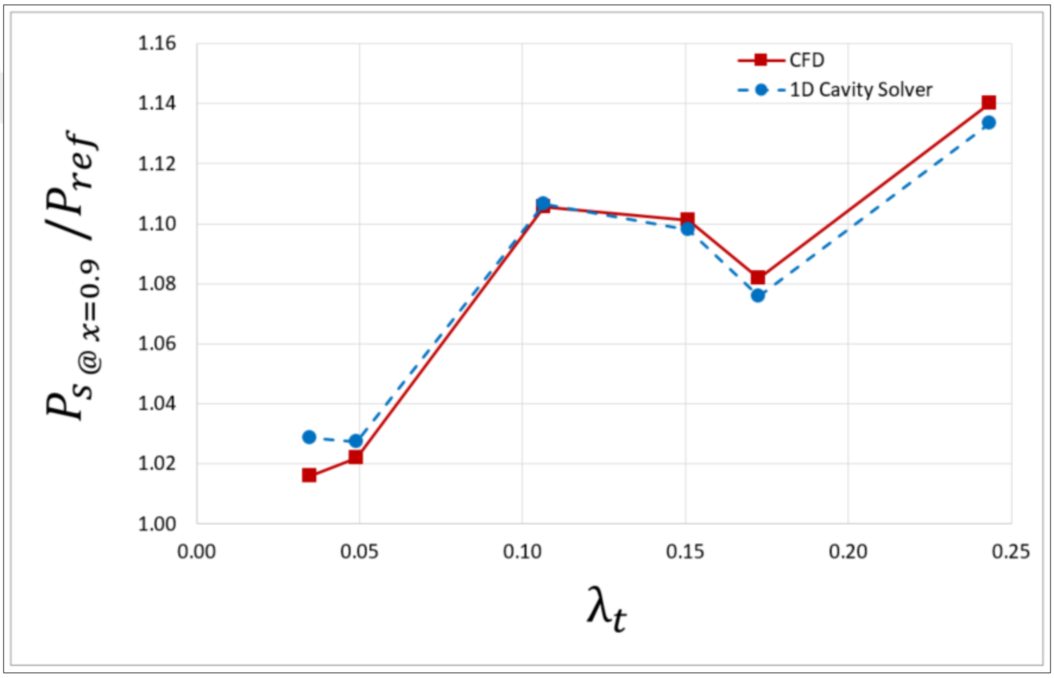

Figure 4.30: Comparison of static pressure at x=0.9 by CFD and cavity solver (SOCS Design tool) ($G = 0.18$).

Moreover, axial loads that exerted to the disks are compared with cavity solver results in **Figure 4.31**. Again, as can be seen from the figure, the differences are less than 1 percent. As a result of this section, it can be concluded that 1D cavity solver tool giving results very close to numerical simulations. In addition, considering the effort spent on numerical setup and mesh, we can say that results are excellent since it takes a few minutes to solve each of these cases with cavity solver, while it takes 15 to 20 minutes for 1 case with CFD.

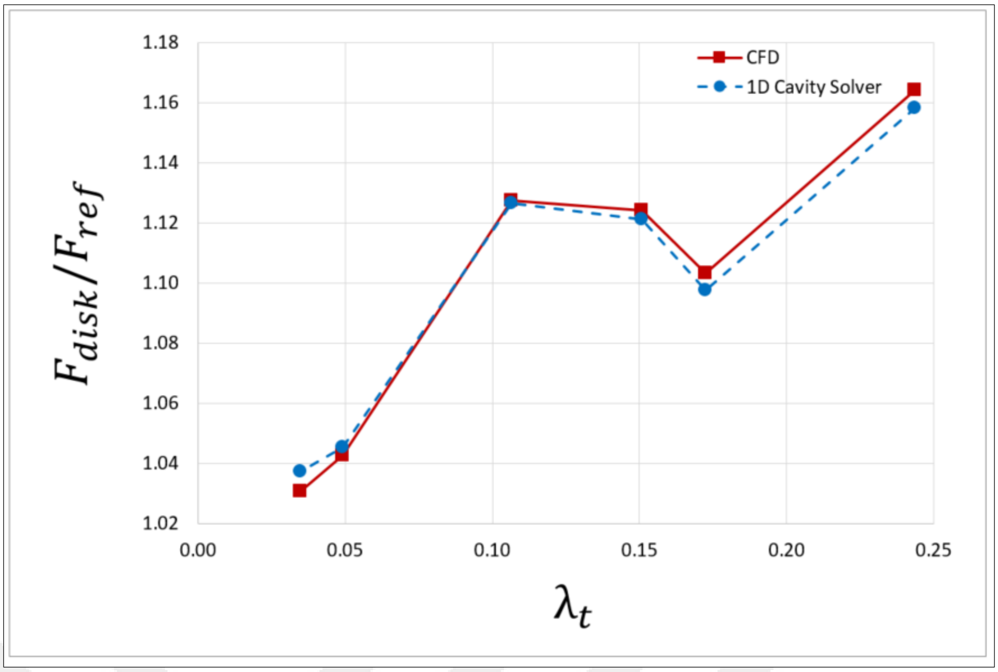

Figure 4.31: Comparison of axial thrust by CFD and cavity solver (SOCS Design tool) ($G = 0.18$).

4.7. Rough Disk - Smooth Casing Results

In this section, results are given for a specific gap ratio where the throughflow rate and rotational Reynolds number are constant but only the rotor disk roughened as a parameter to investigate the roughness effect. Our primary objective here was to observe whether the roughness effect can be included in a simple and practical way in numerical simulations. Therefore, rotor disk roughness values are given under wall roughness option by taking roughness constant as unity and entering the equivalent roughness height directly as 2 times (known from the theoretical background in section 2) the average roughness height, R_a for each case. All values are given in micrometers and not specified further for convenience.

In **Figure 4.32**, core rotation swirl factors at $x = 0.8$ are given for different rough disk values. First thing to notice, with the approach we use, smooth case almost overlapping with Ra 3.2 which meaning that actually smooth cases torques, where no roughness values entered as input, corresponding to disk with Ra 3.2 ($k_s = 6.4\ \mu m$) surface quality. On the other hand, as the roughness of the disk increases, since rotor torques are increased, core rotation swirls becoming higher as we expect; and which are in line with Kurokawa et al. **[36]** test results.

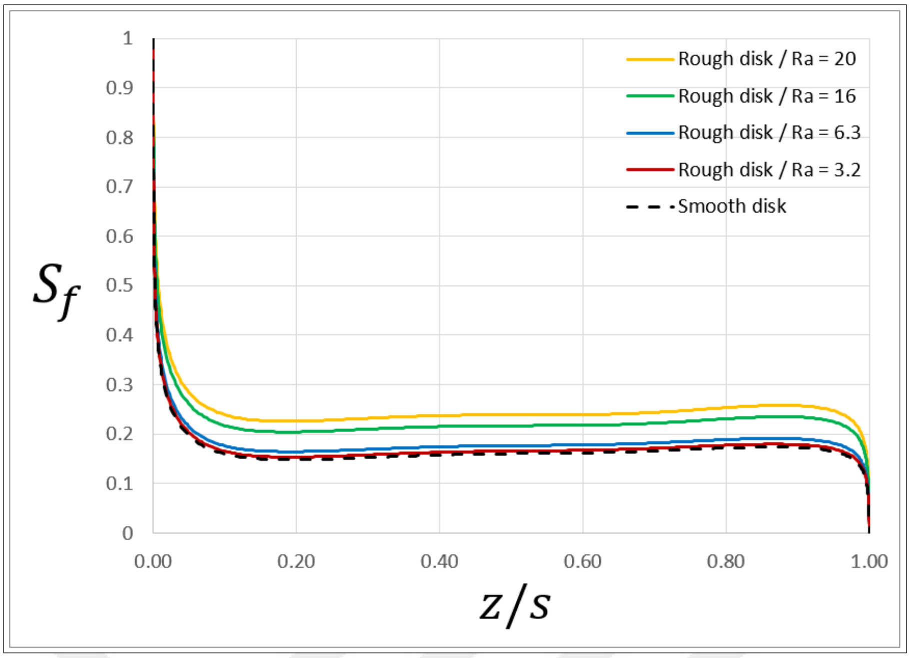

Figure 4.32: Roughness effect on the axial distributions of swirl factors at $x = 0.8$ for $Re_\theta = 4 \times 10^6$, $C_w = 2.04 \times 10^4$, $\lambda_t = 0.107$, $G = 0.12$. $(k_s = 2R_a)$

If we investigate roughness effect on the radial distribution of core swirls given in **Figure 4.33**, roughness effects appearing first at the outer radius of the disk due to the decrease in viscous sublayer thickness towards outer radii as we expect.

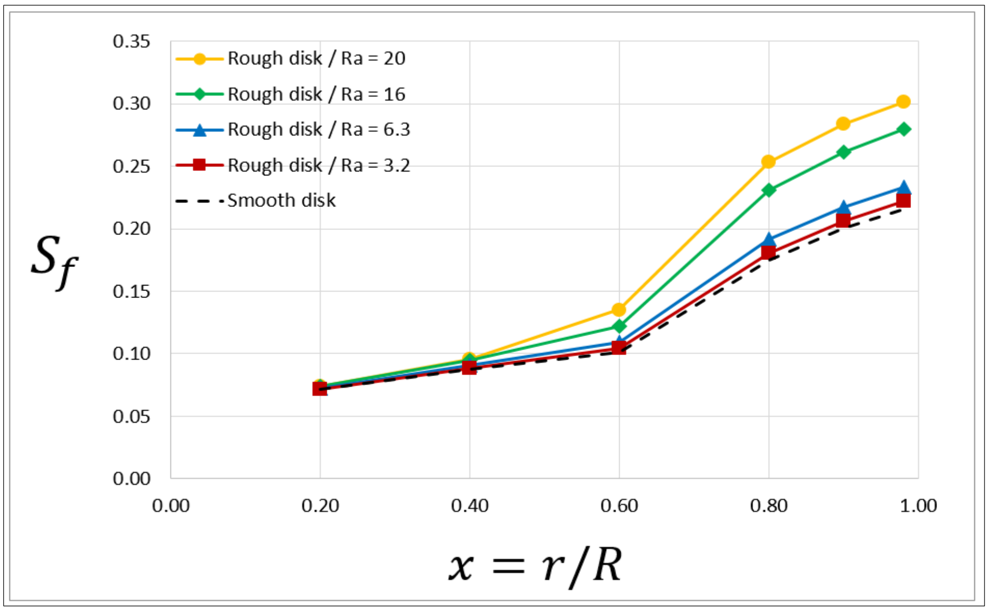

Figure 4.33: Roughness effect on the radial distribution of swirl factors for $Re_\theta = 4 \times 10^6$, $C_w = 2.04 \times 10^4$, $\lambda_t = 0.107$, $G = 0.12$. $(k_s = 2R_a)$

This effect can be recognized from the curves of Ra 3.2 and 6.3; Ra 3.2 almost identical to smooth case as mentioned and swirl factor for Ra 6.3 increasing first at the outer periphery with an increase of the disk roughness but almost same at lower radii, $x < 0.6$. With further increase of roughness Ra 16 and Ra 20, swirl factors beginning to apart from those for the smooth case and the boundary layer flow might be in the transition region ($\delta_s \leq k_s$) at $0.4 < x < 0.6$; but at radii lower than this, $0.2 < x < 0.4$, still almost no roughness effect which can be considered as hydraulically smooth region.

In **Figure 4.34** shows windage powers and resulted exit temperatures for increasing disk roughness values in terms of average height parameter, R_a. As can be seen from the figure, roughness of course affects the windage power and with the increase in roughness, windage generation also increases but not in a significant manner for real case applications. Disks in gas turbines are polished lower than these values and even Ra 6.4 is rough, which causing only a 10 percent increase in windage power compared to smooth case. However, although it is too rough for industrial applications, there is a significant increase of 45 percent in windage power for Ra 20 compared to smooth case.

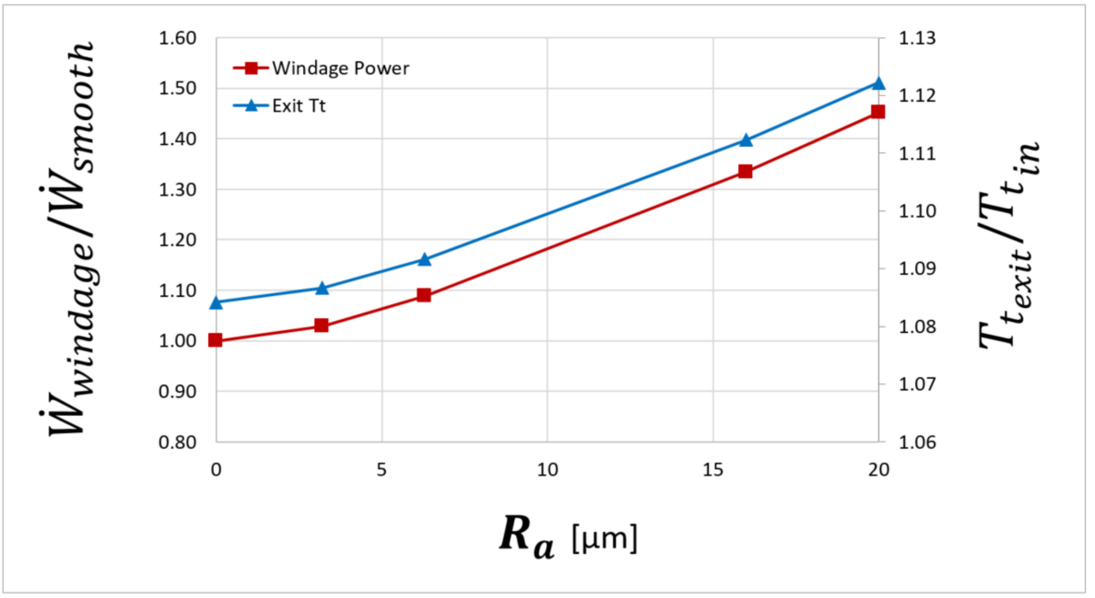

Figure 4.34: Roughness effect on windage power and resulted exit total temperature for $Re_\theta = 4 \times 10^6$, $C_w = 2.04 \times 10^4$, $\lambda_t = 0.107$, $G = 0.12$. ($k_s = 2R_a$)

According to k_s/R range of correlations in the literature, the lowest roughness value corresponding to our case was Ra 32 and for this value there was an increase of 50-55 percent compared to smooth case (see **Figure 2.25** and **Figure 2.40**) as “free disk” at the same rotational Reynolds number (we are not far from “free disk” case with low core rotation swirls between $0.1 < S_f < 0.3$). Therefore, the results seem to be reasonable.

Simulations were also run for higher roughness values to see the results and to compare with correlation results that derived for high k_s/R ranges in the literature mentioned in section 2.6.3.; however, due to the fine mesh we have, y+ values becoming too low against higher k_s^+ values (non-dimensional k_s that used by Fluent) with increasing friction velocity towards the periphery of the disk and causing to singularity points together with inconsistent spike-like temperature increases in adiabatic wall temperature. The reason for this, velocity profile shifting approach that Fluent using for roughness specified walls as stated in Theory Guide **[54]**. Universal velocity profiles are being shifted according to corresponding ΔB values that depends on non-dimensional k_s^+ values for different roughness regimes as shown in **Figure 4.35**.

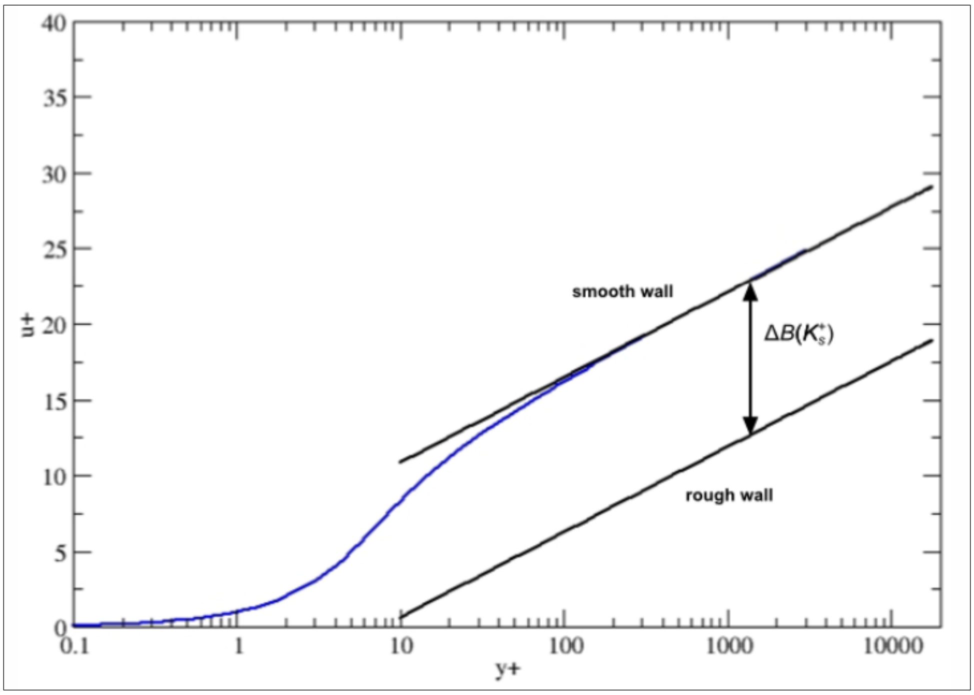

Figure 4.35: Downward shift of the universal velocity profile for rough walls **[54]**.

Although Fluent uses an approach for all two-equation turbulence models called "virtually shifting the wall" **[54]** to avoid this singularity problem, which as it names implies, shifting the wall by some portion of k_s^+ and correcting the y+ value for the first cell center; results could only be obtained up to Ra 20. For higher roughness values (i.e. Ra 32, Ra 42) this singularity occurred. It might have been possible to obtain a solution for higher roughness values with coarser mesh corresponding to very high y+ values, but since such cases would remain very rough compared to our real case examples, no more time was spent.

As a result of this section, it can be said that roughness (up to a certain value) can be easily included into numerical simulations even with fine meshes, and results seem quite reasonable for rough disk-smooth casing cases.

4.8. Rough Disk – Rough Casing Results

The same approach (setting roughness constant as unity and entering the equivalent roughness, k_s values directly as 2 times the average roughness height, R_a to wall roughness) was applied to the stator side in this section together with equally roughened rotor disk at same Reynolds number and throughflow rate for a specific gap ratio.

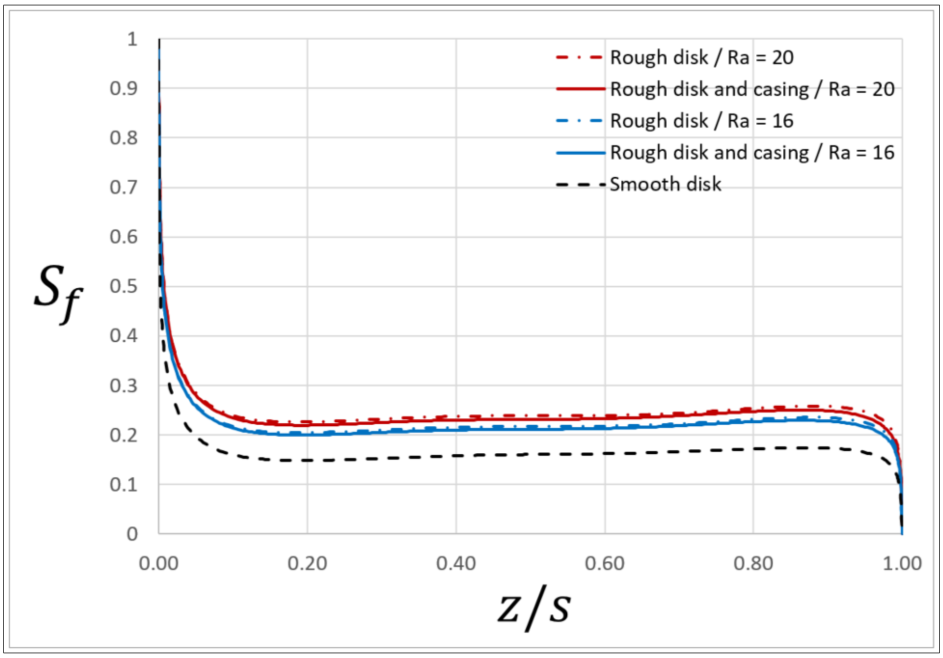

Figure 4.36: Comparison of roughness effect on the axial distributions of swirl factors at $x = 0.8$ with equally roughened disk and casing for $Re_\theta = 4 \times 10^6$, $C_w = 2.04 \times 10^4$, $\lambda_t = 0.107$, $G = 0.12$. ($k_s = 2R_a$)

Figure 4.36 shows the comparison of core rotation swirls at $x = 0.8$ for both cases where only rotor disk roughened and both rotor and stator equally roughened. Since core rotation swirls are low, which in this case around 0.15 for smooth, meaning low gradient between stator and fluid resulting in low torque between. For this reason, there is no significant difference when the stator side roughened in addition to rotor as in Kurokawa's test results in which core rotation swirls was above 0.4 for smooth case meaning almost same gradient between rotor and stationary walls.

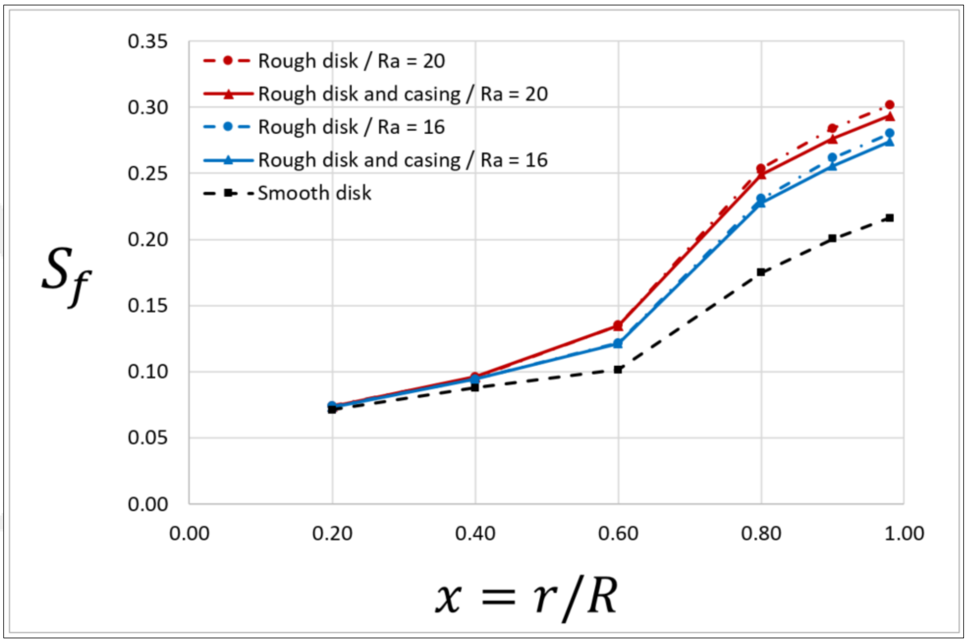

Figure 4.37: Comparison of roughness effect on the radial distribution of swirl factors with equally roughened disk and casing for $Re_\theta = 4 \times 10^6$, $C_w = 2.04 \times 10^4$, $\lambda_t = 0.107$, $G = 0.12$. ($k_s = 2R_a$)

This difference more notable when we look at the comparison between radial distribution of swirl factors in **Figure 4.37**. At the outer radii, where the roughness effect increasing, equally roughened cases begin to differ but the difference still very small. Since there is no difference in these cases compared to the cases where we only roughen the rotor, windage levels are almost the same and for this reason, those figures were not added. It should be noted once again since there is no difference in our cases due to low gradients between, does not mean the roughness values on stator are negligible or have no effect. Specific to our case, there is no torque between, however if we had a flow rotating close to disk speeds, it would be possible where roughness value of stationary walls make more difference than that of the rotor.

5. EXPERIMENTAL APPROACH

Windage is not an easy phenomenon to measure; in fact, it is not even possible to measure it in engine tests since the heat transfer cannot be excluded. Therefore, established test rigs generally aim to measure it from consumed power. However, there are other parts (mechanical losses such as bearings) that make the rig work have an impact on this consumed power, and their losses also depend on different parameters, making it difficult to measure the windage accurately. The strain gage method of Daily and Nece **[19] (**see section 2.3.), therefore, is a well-established solution to this issue and is therefore widely recognized and used in the literature. Within the scope of this study, a test rig was designed similar to Tao et al. **[55]** but to measure windage directly from the enthalpy rise of the air as a difference in a cavity insulated with epoxy woven glass fabric through rotating disk and stationary casing; both because it would be the closest case to real cavity examples and because it will also give us more knowledge in addition to windage.

5.1. Test Rig Design

Figure 5.1 shows the general setup of the test rig. The main components of the assembly includes a shrouded stationary casing and a rotor disk 450 mm in diameter driven by spindle. A 120 kW spindle motor is used as a part of future rig plans, maximum disk speed planned as 15000 rpm corresponding to a rotational Reynolds number about 6 million at highest throughflow case (4 million for “free disk”).

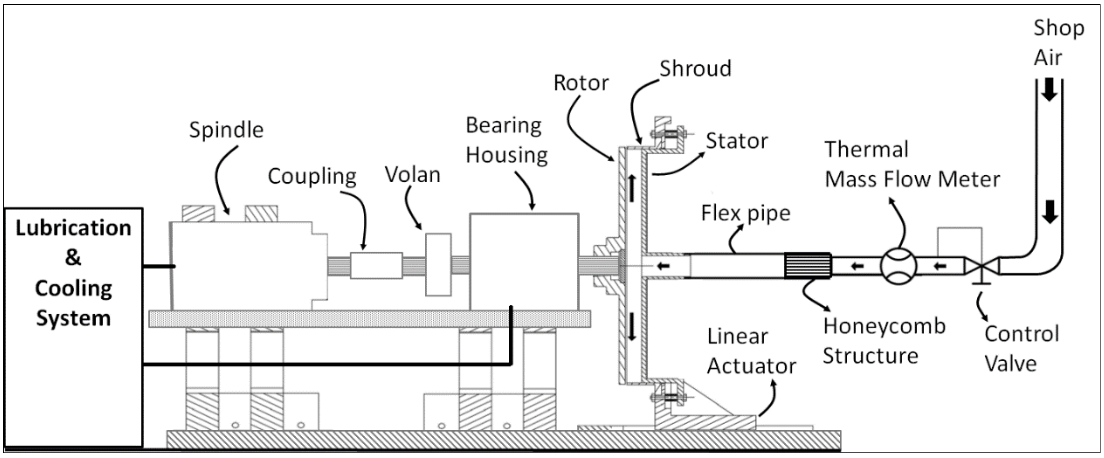

Figure 5.1: The schematic of the test rig.

Air will be supplied at flow rates up to 0.3 kg/s through a 50 mm pipe opening into the center of the stator. A thermal mass flow meter will be used to measure the air mass flow rate. There is also a honeycomb of tube, made by additive manufacturing, in the upstream to ensure the uniformity and stability of the throughflow supplied. 4340 forged steel disk and 6061 aluminum alloy stationary parts being insulated with epoxy woven glass fabric which of the thermal conductivity is about $0.2\ \mathrm{W/mK}$. A cylindrical shroud was attached to the periphery of the stator and the gap ratio could be altered continually with spacer rings, while sealing between ensured with an O-ring as shown in **Figure 5.2**.

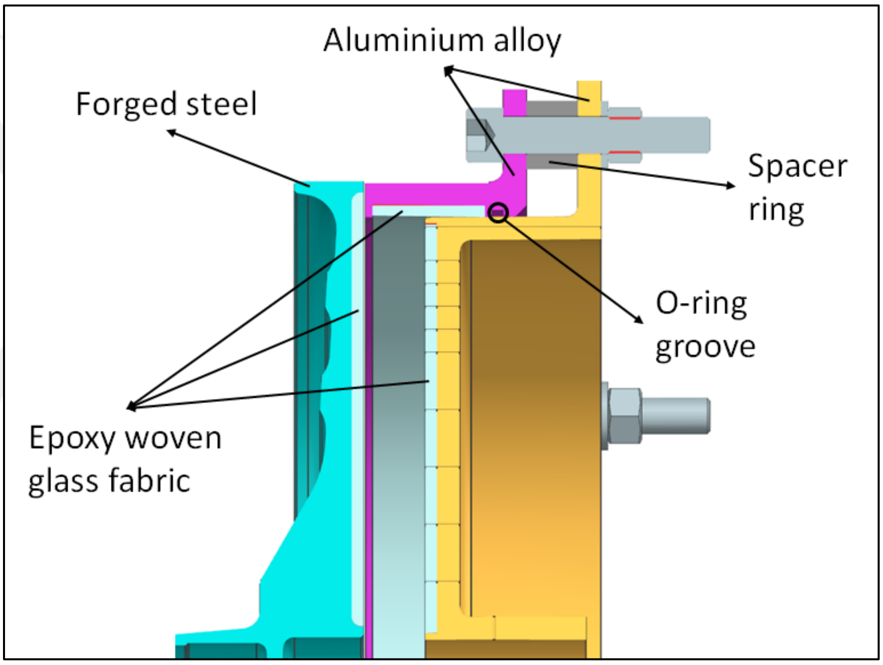

Figure 5.2: 3D assembly of the rotor-stator cavity for $G = 0.12$.

A linear actuator can be moved within 100-μm sensitivity and controlled by laser displacement sensors embedded into the shroud, measuring the axial clearance between shroud and the surface of the disk. Static pressure measurements will be made from stator side at three different locations on one row at 10 radius ratios where the innermost position was located at $x = 0.2$, the outermost at $x = 0.91$. Total temperatures of the air will be measured through K-type thermocouples located at 3 different locations on one row at 4 radius ratios between $0.4 < x < 0.85$, as well as 3 each at the inlet of the stator and at the tip of the shroud as the closest location to rim of the disk.

Tests will be run until measured temperatures at critical locations reach steady state, which considered as temperatures not changing ±1 K for at least 30 seconds; then values will be averaged over 10 second. In general, the automation of the test rig and the diagram of the data to be collected are shown in **Figure 5.3**.

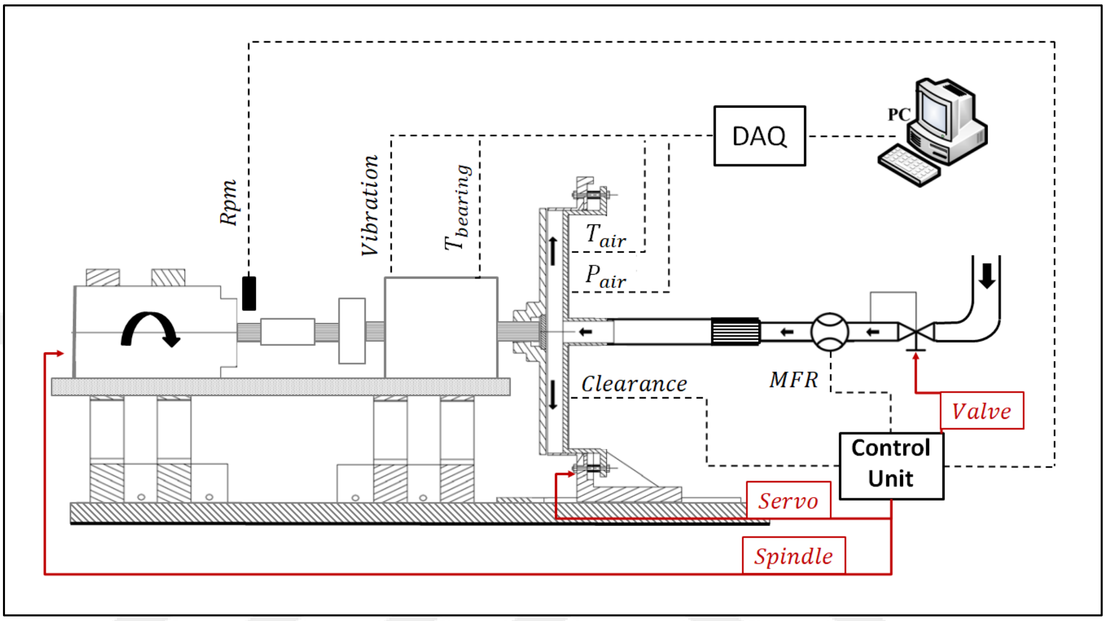

Figure 5.3: Test rig automation and data acquisition chart.

First, the test rig will be increased to the desired rpm and flow rate through spindle and valve control. Afterwards, the stationary side is then brought up to the desired clearance value and the measurements will be taken when steady-state condition is reached. Tests will be repeated at different gap ratio, clearances, throughflow rates and Reynolds numbers.

5.1.1. “Free Disk” Entrainment Tests

For this test configuration, a second shroud was designed to make a chamber that will allow us to directly measure the “free disk” pumping rates using the same rig. The logic behind the test is to first creating an environment as in the “free disk” case and then to surround the purely axial flow that induced by disk at away from disk with a chamber without interfering with the boundary layer flow. For this reason, we first increase the gap ratio to a point where the core rotation concepts disappears and the disk becomes a “free disk” like condition; and then superposed air being smoothed by a baffle at the entry, then passing through perforated metal with 2 mm holes (1.5 mm pitch) and then through 9 mm cell size honeycombs (20 mm pitch) and a wire mesh (0.5 mm mesh gap) at the exit, as shown in **Figure 5.4**, to feed this axial flow uniformly from center to outer periphery of the disk (same technique as that of Case **[14])**.

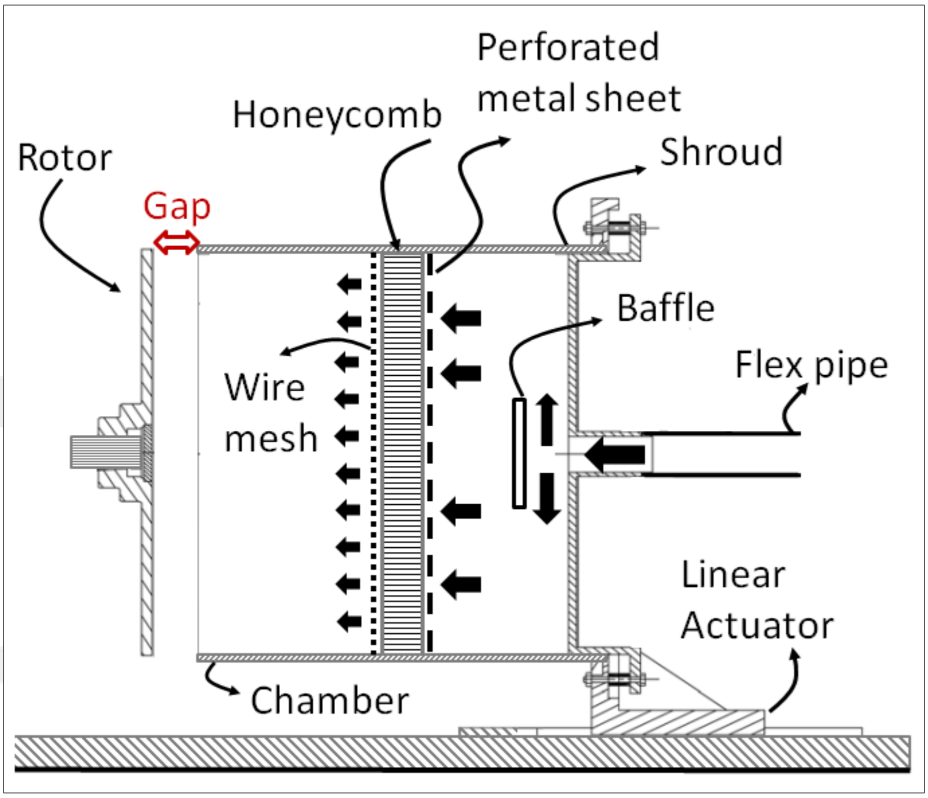

Figure 5.4: The schematic of the "free disk" pumping tests.

When the correct amount of air is supplied there will be no radially outward flow between the edge of the boundary layer and the chamber so that static pressures inside the chamber equals to the atmospheric outside. In addition, the pumping flow rate should be the same whatever the gap between the chamber and the disk surface, as long as the gap remains thicker than the thickness of the boundary layer. If the gap is smaller, the radial outflow will increase the pressures inside the chamber and less air will be needed to produce atmospheric pressure within. Therefore, procedure is to increase the gap between the chamber and the disk until the flow rate for zero pressure difference becomes constant which will be our "free disk" pumping flow rate at that constant Reynolds number. Hence, only static pressures inside and the outside of the chamber will be measured in addition to mass flow rate measurements in this tests.

A second shroud was produced from additive manufacturing as 4 pieces together with its honeycombs from high strength plastic PA 12 (Nylon 12) material in a puzzle-like interfaces bolted from outer flanges with a gaskets between; in addition, a thin layer of silicone was applied to these junctions from the inside of the chamber to ensure complete sealing as shown in **Figure 5.5**.

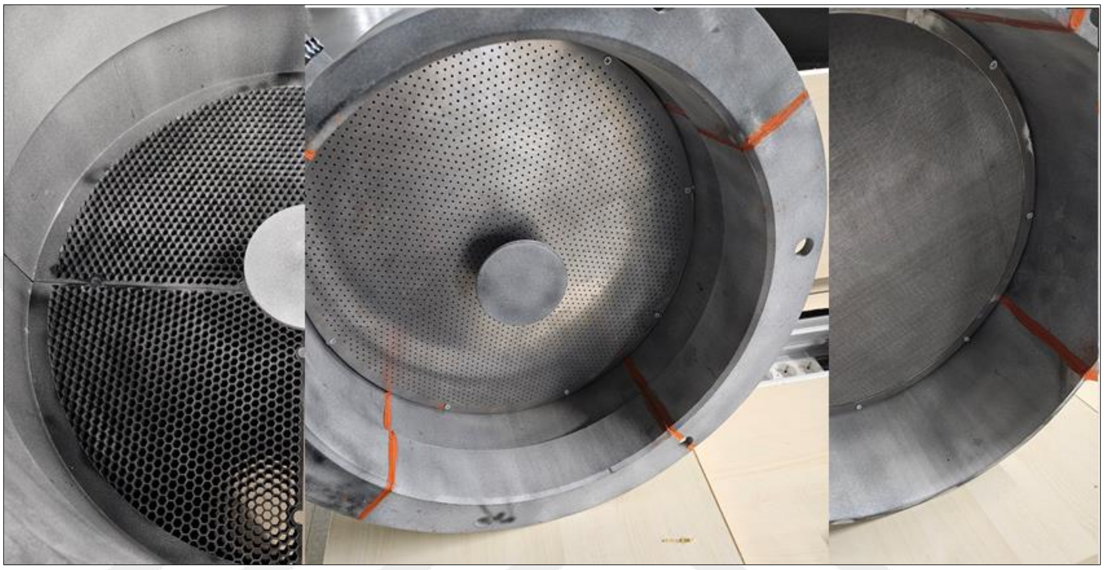

Figure 5.5: Assembly of the second shroud for “free disk” pumping tests.

5.2. Instrumentation and Hardware Selection

Thermal mass flow meter calibrated with additional slot to eliminate the ±0.5% full scale error that occurs in addition to the standard ±0.5% reading accuracy for flows below 50% of full scale; this will allow us high accuracy mass flow measurements of not exceeding 1 g/s between flow rates as high as 0.3 kg/s to as low as 0.03 kg/s.

Scani-valves with 48 channel will be used for pressure measurements which has accuracy ±0.05% of its full-scale range that corresponding to about ±50 Pascal! for our 15 psid slots. Total of 30 tap holes (1 mm diameter) drilled to stator on one pitching at 10 radius ratios as shown in **Figure 5.6**.

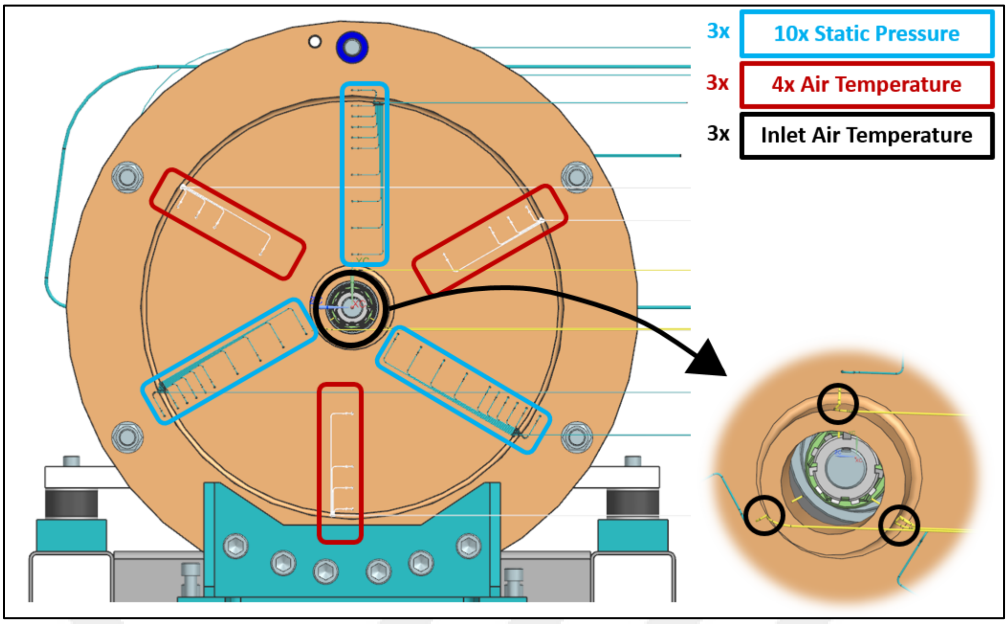

Figure 5.6: Stator instrumentation.

K-type thermocouples with 1 mm probe will be used to measure air temperatures which has accuracy of ±1 °C over full operating range as well as at the inlet of the stator and at the tip of the shroud as shown in **Figure 5.6** and **Figure 5.7**. For air temperatures probes were immersed into the cavity to a distance of 6D (6 mm) from the wall. Laser displacement sensor which has a reading sensitivity of 1 μm also embedded into shroud to measure axial clearance between the disk of the surface. Also, 3 thermocouple will be used to measure the bearing metal temperatures for health and safety purposes.

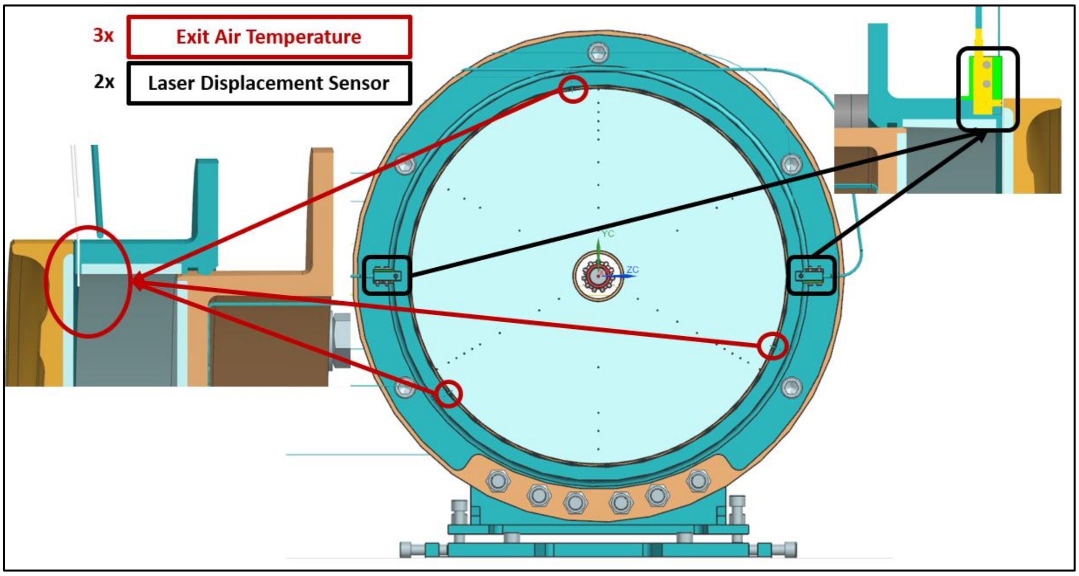

Figure 5.7: Shroud instrumentation.

For second shroud 1 mm tap holes opened inside the chamber towards the tip of the shroud at 4 different point, and for atmospheric pressure measurements also 2 tap drilled to outer flange points.

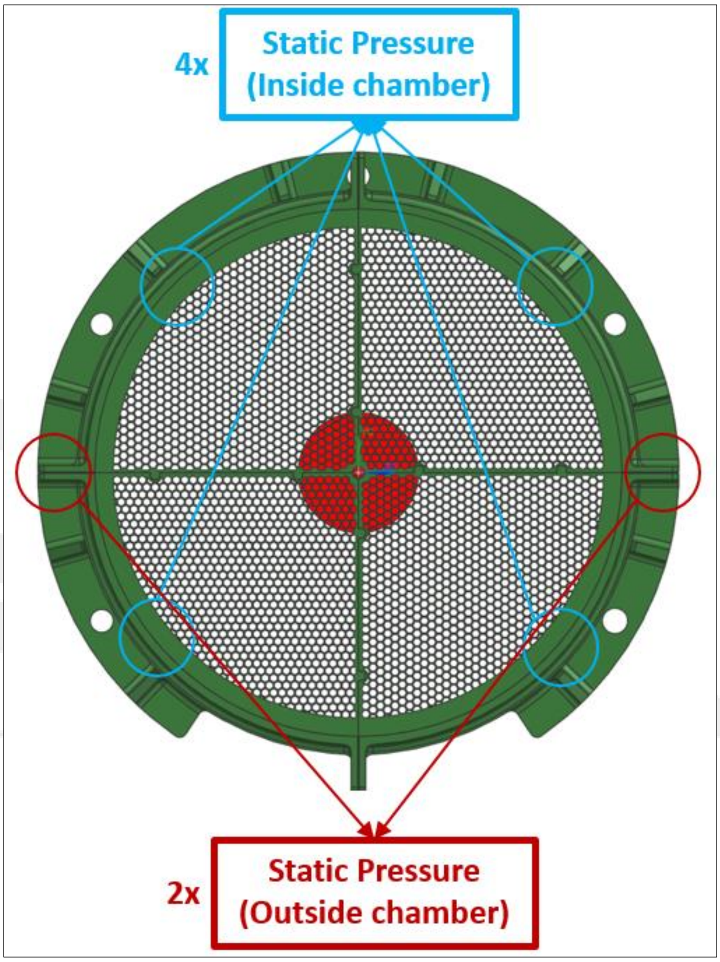

Figure 5.8: Second shroud instrumentation.

In addition to these instruments, ROS-P 25 optical sensor will be used measure shaft rpm, which have a range from zero to 250000 rpm and can be operating up to 0.9 m and 45° from target shaft. Moreover, 3-axis accelerometers placed in to both bearing and main plate locations to measure vibration levels within the system. Test system will have emergency shutdown and will automatically shut down when any of the following situations occur:

- Maximum bearing temperatures exceeded.
- Spindle cooling or lubrication unit does not work.
- Pressed to emergency shutdown.

6. SUMMARY AND DISCUSSION

At the outset, it should be remembered that windage heating is not a desirable yet is an inevitable phenomenon that can be seen in any rotating system as long as there is a velocity gradient between the medium in which it rotates. In addition, windage is a work transfer, although it has a heating effect, this consequential heating is a work done by viscous related friction forces at the direction of rotation; and the generation of heat is in fact a result, not a cause. Hence, this is the reason for the total temperature rise in the fluid, although, all the theoretical and numerical studies that have carried out were adiabatic. From other standpoint it is also a power loss for the one that rotating faster and doing the work, and since this power returns to fluid as a total temperature increase, the amount of mass which will absorbs the heat is also becomes an important point. Therefore, gas turbine designers should always design by considering the windage and should adjust the amount of air that sending for cooling or sealing purposes accordingly to prevent excessive windage heating; and if possible should make designs to reduce the windage, for example by pre-swirling.

In fact, since all these disk-fluid interactions take place over a thin boundary layer at high Reynolds numbers, in this thesis, we investigate the windage starting from its basis “free disk” and boundary layer, to its characteristics in complex rotor-stator structures with superposed radial outflow. We define it with all its depending parameters for both full and partial disk calculations according to moment and skin friction coefficients respectively.

Those empirical correlations gathered from literature, can be used to calculate the windage power required for full disks; and could be useful for example, when power calculation is required for a test rig or other reasons. However, it should be noted once again that all correlations given for one side of the disk only. On the other hand, for partial disk cavity windage calculations, constant skin friction approach given by Sultanian **[1]** together with skin friction coefficients, resulting in very close results to numerical simulations that validated through test data, therefore, seems reasonable to use in windage and swirl distribution calculations for 1D flow modelling.

In chapter 3, cavity solver tool introduced to calculate windage and swirl distributions inside complex cavities with superposed radial outward or inward flow. This tool very powerful in terms of cost, it is solution-robust and always converging in a few seconds. In chapter 4, it is shown that flow structure and windage in rotor-stator cavities can be successfully predicted with numerical simulations using k-ω SST turbulence model. However, comparison studies shows that cavity solver can be concluded as a best tool in terms of accuracy and computational cost.

Moreover, roughness studies through numerical simulations given reasonable results compared to literature and it seems roughness effects can be easily included with our approach into CFD but only up to some extent. Disks in gas turbines are polished to low roughness values and even Ra 6.4 is rough, which causing only a 10 percent increase in windage power compared to smooth case. However, although it is too rough for industrial applications, there is a significant increase of 45 percent in windage power for Ra 20 compared to smooth case. Results shows that the roughness is an important parameter for both windage and swirl distributions inside the cavity, however when compared to our real gas turbine applications, these cases remaining too rough. For roughness to have a significant effect on windage, the surface must be very rough.

Studies were also carried out for pre-swirl cases, but in our case, since the air directly introduced from the center, no matter how high the swirl it enters, there was no change worth mentioning, and for this reason were not added to thesis. Although it could have been possible by increasing the amount of throughflow too much but those studies were not made to stay in the range of gas turbine applications.

Additionally, a full 3D model CFD was also performed for our cavity and the results, although not given in the thesis, were quite close to 2D results. Therefore, considering the effort and computational cost spent, it can be concluded that if there is an axisymmetric case as ours, 2D seems quite advantageous over 3D.

At last but not the least, in chapter 5, test methods are introduced to quantify windage directly from the enthalpy rise of the air and for direct entrainment measurements. Test rig setup was explained along with the instrumentation and hardware selection.

7. AN INTERESTING FACT ABOUT WINDAGE

During my Master studies, I came across a Ted Talk **[57]** about Supermassive Black Holes presented by Dr. Martin Gaskell who is a research lecturer in the Department of Astronomy and Astrophysics at UCSC, spent his career studying what happens around supermassive black holes. He was showing the image of Quasar 3C 273 below which looks like a bright star and as Martin said that is indeed what scientists think first.

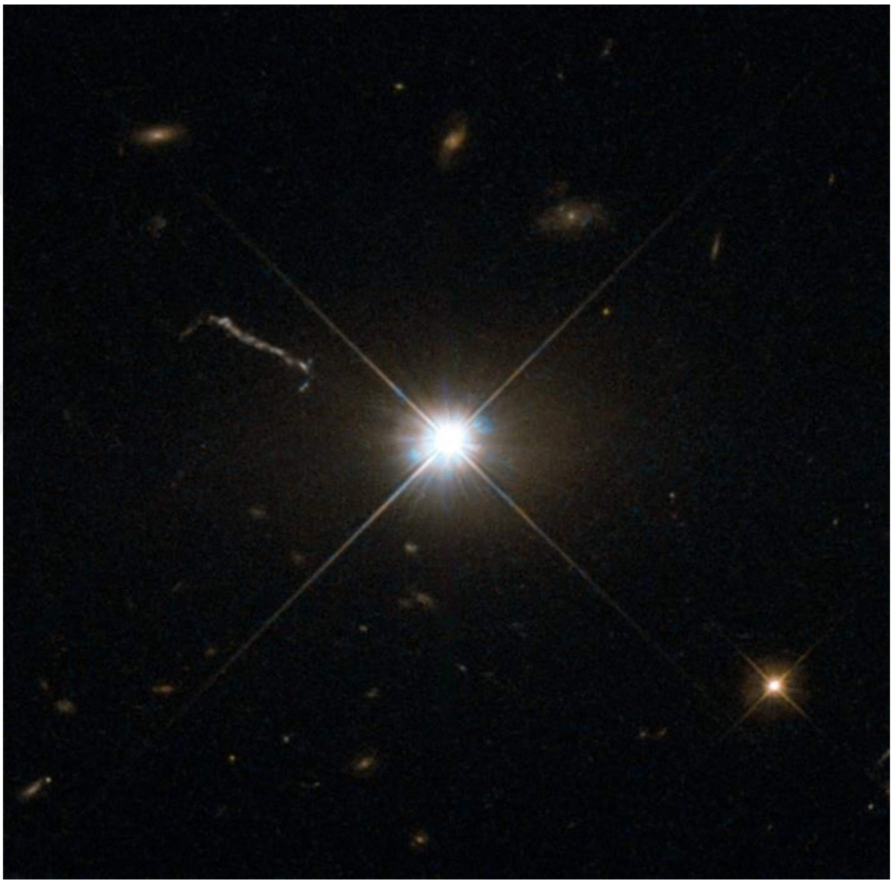

Figure 7.1: Image of Quasar 3C 273 captured by Hubble Space Telescope **[58]**.

Matter going to black hole is mostly gas or is entirely gas. So gas that falling towards a supermassive black hole ending up swirling, spiraling around it and setting down, what scientists call an accretion disk as illustrated in **Figure 7.2**. In the accretion disk, gas that is closer to black hole swirling faster than the gas further out and due to this differential motion, the one going faster heating up the near gas through friction.

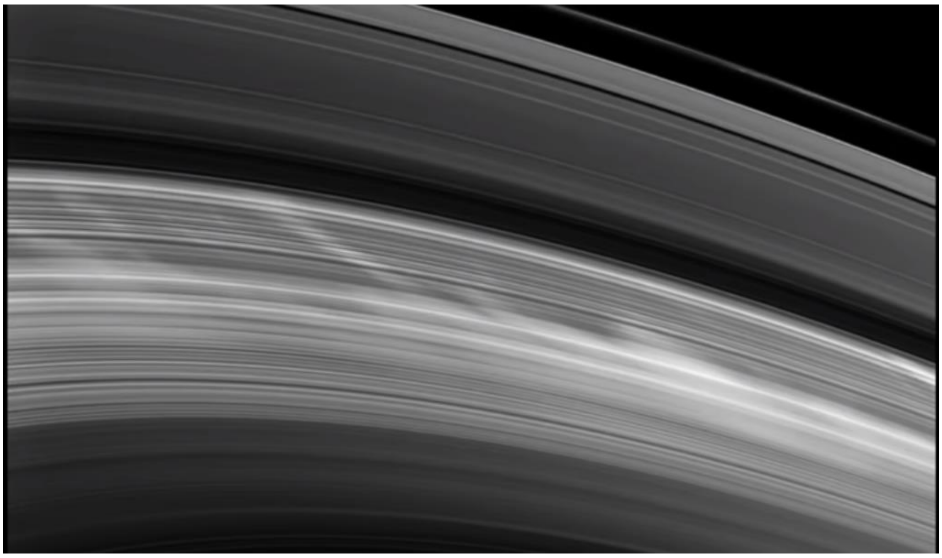

Figure 7.2: Illustration of an accretion disk around supermassive black hole **[57]**.

This viscous related friction heating actually so much that accretion disk becoming white-hot, like a glowing steel ready to be forged, and we receive the light from it like a shining star in **Figure 7.1**. This light have no difference from the light coming from our Sun but 3C 273 actually 4 trillion times brighter than our Sun and about 100 times more luminous than the total amount of light produced by the entire Milky way. It was the first identified Quasar and stayed long time as the most powerful object in the universe. If you look at the **Figure 7.1** again, those little blurry colored dots are actually entire galaxies like our own Milky Way!

More interestingly as the material from the accretion disk falls inwards, some Quasars, including 3C 273 firing of their energy in the form of radiation jets to the surrounding space. In this picture, it appear as cloudy streak on the slightly top left to 3C 273 which is actually 200 000 light-years length. Today, we observed even more powerful objects than 3C 273 in the universe, see blazar 3C 454.3, which is nothing but mind-boggling **[59]**.

As an analogy to this, in gas turbines, air in cavities that is most of the case rotating slower than the disk exposing to same viscous related frictional heating what we call windage heating but as a difference, we are dealing with speed of sound scales in gas turbines while it happens at the scale of the speed of light around black holes. I was so fascinated that viscous friction heating can result in such things in universe, I e-mailed Martin Gaskell. He was kind enough to answer that I am right about the logic but around black holes friction due to simple gas viscosity, as we saw in gas turbines, is weak and viscosity due to magnetic field is the main driver for friction heating.

One can see below an artist's drawing of J0313-1806. It is found recently and identified as the most redshifted, which makes it the oldest (formed just around 670 million years after the Big Bang!) known Quasar ever **[60]**. Today, its existence at such an early time is inconsistent with current theories and confused the scientific world.

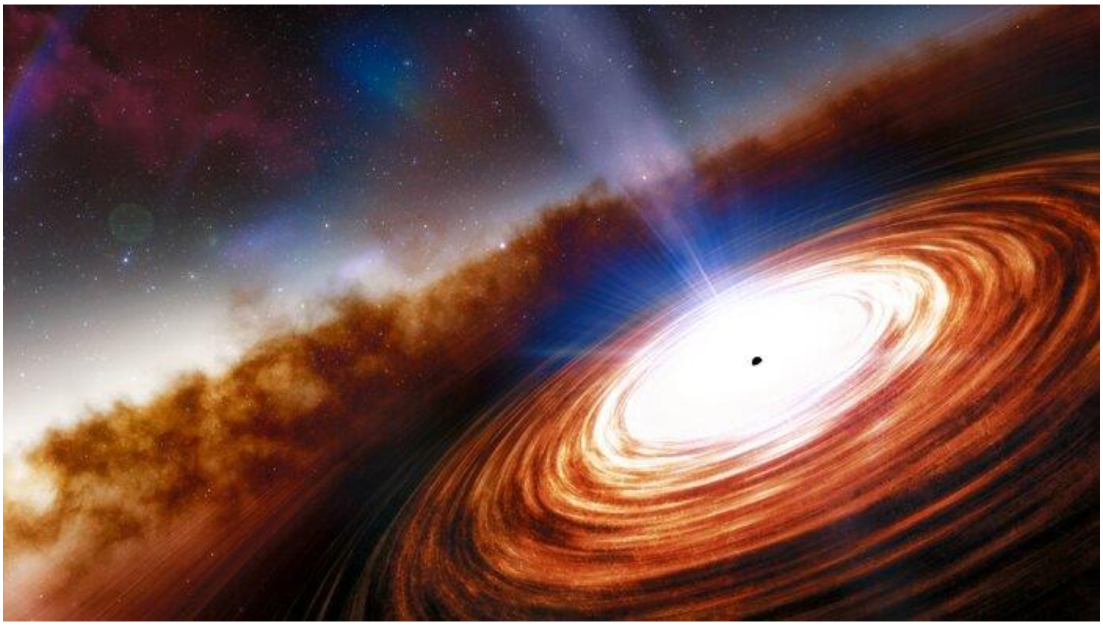

Figure 7.3: Artist's impression of J0313-1806 **[61]**.

REFERENCES

[1] Sultanian B. K., (2018), “Gas Turbines: Internal Flow Systems Modeling”, Cambridge University Press.

[2] Rolls-Royce Plc., (2005), “The Jet Engine”, 5th Edition, Wiley.

[3] Owen J. M., and Rogers R. H., (1989), “Flow and Heat Transfer in Rotating Disc Systems - Vol.1: Rotor-Stator Systems”, W. D., Morris ed., Wiley, New York.

[4] Schlichting H., (1960), “Boundary Layer Theory”, McGraw Hill Publishing Company.

[5] Child P. R. N., (2010), “Rotating Flow”, Elsevier.

[6] Theodorsen T., Regier A., (1944), “Experiments on drag of revolving disks, cylinders and streamline rods at high speeds”, NACA Rep. No. 793.

[7] Gregory N., Stuart J.T., Walker W.S., (1955), “On the Stability of Three-Dimensional Boundary Layers with Application to the Flow Due to a Rotating Disk”, Philosophical transactions of the Royal Society - Series A, Mathematical, physical and engineering sciences, Vol. 248, p. 155-199.

[8] Karman Th. Von., (1921), “on laminar and turbulent friction”, NACA TM No.1092.

[9] Cochran W., (1934), “The flow due to a rotating disc”, Mathematical Proceedings of the Cambridge Philosophical Society, 30(3), 365-375.

[10] Prandtl L., (1927), “Über den Reibungswiderstand strömender Luft” Ergebnisse der Aerodynamischen Versuchsanstalt in Göttingen, III. Lieferung, 1–5, Oldenbourg, München/Berlin.

[11] Nikuradse J., (1966), “Laws of turbulent flow in smooth pipes”, NASA, Washington. Translated from Nikuradse J. “Gesetzmassigkeiten der turbulenten Stromung in glatten Rohren,” VDI-Forschungsheft No. 356, Edition B, Volume 3, 1932, pp. 1-36.

[12] Dorfman L. A., (1963), “Hydrodynamic Resistance and the Heat Loss of Rotating Solids”, Oliver and Boyd.

[13] Bayley F.J., Owen J.M., (1969), “Flow between a rotating and a stationary disc”, Aeronautical Quarterly, Vol. 20, p. 333-354.

[14] Case P., (1966), “Measurements of entrainment by a free rotating disc”, J. Roy. Aero Soc. 71, 124.

[15] Cham T., Head M., (1969), “Turbulent boundary-layer flow on a rotating disk”, Journal of Fluid Mechanics, 37(1), 129-147.

[16] Newman B. G., (1983), “Flow and heat transfer on a disk rotating beneath a forced vortex”, AIAA Journal, 21(8), 1066–1070.

[17] Batchelor G. K., (1951), “Note on a class of solutions of the Navier-stokes equations representing steady rotationally symmetric flow” Quart. J. Mech. App. Math., (4):29–41.

[18] Daily J.W., Ernst W.D., Asbedian V.V., (1964), “Enclosed Rotating Discs with Superposed Through-Flow”, Massachusetts Institute of Technology, Report No. 64.

[19] Daily J.W., Nece R.E., (1960), “Chamber dimension effects on induced flow and frictional resistance of enclosed rotating disks”, Journal of Basic Engineering 82, p. 217-232.

[20] Hu B., (2018), “Numerical and experimental investigation on the flow in rotor-stator cavities”, Doctorate Thesis, University of Duisburg-Essen.

[21] Owen J.M., (2010), “Prediction of ingestion through turbine rim seals-part i: Rotationally induced ingress”, Journal of Turbomachinery, 133, 2010b.

[22] Owen J.M., (1989), “An Approximate Solution for the Flow Between a Rotating and a Stationary Disc”, Journal of Turbomachinery, Vol. 111, No. 3, p. 323-332.

[23] Da Soghe R., Facchini B., Innocenti L., Micio M., (2009), “Analysis of gas turbine rotating cavities by an one-dimensional model: Some improvements in a core-swirl ratio correlation”, ISABE Paper, (ISABE-2009-1135).

[24] Poncet S., Schiestel R., Chauve M. P., (2005), “Centrifugal flow in a rotor-stator cavity”, In Journal of Fluids Engineering, Transactions of the ASME (Vol. 127, pp. 787–794).

[25] Micio M., Massini D., Facchini B., Bavassano F., Mantero M., (2015), “Experimental investigation of flow within a rotor stator cavity”, In 11th European Conference on Turbomachinery Fluid Dynamics and Thermodynamics, European Conference on Turbomachinery (ETC).

[26] Lyman F. A., (1993), “On the conservation of rothalpy in turbomachines” Journal of Turbomachinery, 115(3), 520–525.

[27] Liepmann H. W., Roshko A., (1957), “Elements of gas dynamics”, John Wiley & Sons, New York.

[28] Haaser F., Jack J., McGreehan W., (1988), “Windage rise and flow-path gas ingestion in turbine rim cavities”, Journal of Engineering for Gas Turbines and Power, 110(1), 78–85.

[29] Hart K.J., Turner A.B., (1995), "Simple Design Methods for the Prediction of Radial Static Pressure Distributions in a Rotor-Stator Cavity with Radial Inflow", Proceedings of the ASME International Gas Turbine and Aeroengine Congress and Exposition Volume 1: Turbomachinery, Houston, Texas, USA.

[30] Erdem E., Sertcakan M.C., Sal S., Dogu Y., Yalcinkaya A., (2022), “Investigation of Impeller Backface Cavity Flowfield Using Cfd and a One-Dimensional Flow Solver”, GT2022-84036.

[31] Yazan A., Karasu Z.T., Yilmaz S., Erdem E., Sal S., (2023), “Investigation of Rotor Stator Cavity Flowfield at Downstream of a High Pressure Turbine Disk”, GT2023-103713.

[32] Gadelmawla E. S., Koura M. M., Maksoud T. M. A., Elewa I. M., Soliman H. H., (2002), “Roughness parameters”, Journal of Materials Processing Technology, 123(1), 133–145.

[33] Nikuradse J., (1933), “Laws of flow in rough pipes”, VDI-Forchungsheft 361, Series B, Vol. 4 (English translation NACA TM 1292, 1950).

[34] Coleman H. W., Hodge B. K., Taylor R. P., (1984), “A re-evaluation of Schlichting’s surface roughness experiment”, Journal of Fluids Engineering, Transactions of the ASME, 106(1), 60–65.

[35] Nece R. E., Daily J. W., (1960), “Roughness effects on frictional resistance of enclosed rotating disks”, Journal of Fluids Engineering, Transactions of the ASME, 82(3), 553–560.

[36] Kurokawa J., Toyokura T., Shinjo M., Matsuo K., (1978), “Roughness Effects on the Flow along an Enclosed Rotating Disc”, Bulletin of the JSME, Vol. 21, pp. 1725-1732.

[37] Bons J. P., (2010), “A review of surface roughness effects in gas turbines”, Journal of Turbomachinery, 132(2).

[38] Chew J. W., (1984), “Prediction of flow in rotating disc systems using the k-ε model”, ASME paper (84-GT-229).

[39] Chew J. W., Vaughan C. M., (1988), “Numerical predictions of flow induced by an enclosed rotating disk”, ASME paper (88-GT-127).

[40] Iacovides H., Theofanopoulos L.P., (1991), “Turbulence modeling of axisymmetric flow inside rotating cavities”, Int. J. Heat Fluid Flow 12:1, 2-11.

[41] Menter F. R., (1994), “Two-equation eddy viscosity turbulence models for engineering applications”, AIAA J., 32, pp. 1598–1605.

[42] Elena L., Schiestel R., (1996), “Turbulence modeling of rotating confined flows”, Int. J. Heat Fluid Flow, 17, pp. 283–289.

[43] Riccardo da Soghe, Luca Innocenti, Antonio Andreini, Sébastien Poncet, (2010), “Numerical Benchmark of Turbulence modelling in Gas Turbine Rotor-Stator System”, ASME TURBO EXPO 2010: Power for Land, Sea & Air (GT2010), Jun 2010, Glasgow, United Kingdom.

[44] Severac E., Poncet S., Serre E., Chauve M.P., (2007), “Large eddy simulation and measurements of turbulent enclosed rotor-stator flows”, Phys. Fluids 19, 085–113.

[45] Makino S., Inagaki M., Nakagawa M., (2015), “Laminar-turbulence transition over the rotor disk in an enclosed rotor-stator cavity”, Flow Turbulence Combust 95: 399–413.

[46] Itoh M., Yamada Y., Imao S., Gonda M., (1992), “Experiments on turbulent flow due to an enclosed rotating disk”, Exp. Therm. Fluid Sci. 5, 359–368.

[47] Cheah S., Iacovides H., Jackson D., Ji H., Launder B., (1994), “Experimental investigation of enclosed rotor-stator disk flows”, Exp. Therm. Fluid Sci. 9, 445–455.
[48] Fernando D., Gao S., Garrett S. J. (2018), “The effect of surface roughness on rotor-stator cavity flows”, Physics of Fluids, 30(6).

[49] Busse A., Sandham N. D., (2012), “Parametric forcing approach to rough-wall turbulent channel flow,” J. Fluid Mech. 712, 169–202.

[50] Gan X., Kilic M., Owen J. M., (1995), “Flow between Contra-Rotating Discs”, ASME J. Turbomach., 117, pp. 298–305.

[51] Kilic M., Owen J. M., (2003), “Computation of Flow between Two Disks Rotating at Different Speeds”, ASME. J. Turbomach. April 2003; 125(2): 394–400.

[52] Lygren M., Andersson H. I., (2001), “Turbulent flow between a rotating and a stationary disk”, Journal of Fluid Mechanics, 426, 297–326.

[53] Andersson H. I., Lygren M., (2006), “LES of open rotor stator flow”, International Journal of Heat and Fluid Flow, 27(4), 551–557.

[54] ANSYS Inc., (2023), Ansys Fluent Theory Guide

[55] Tao Z., Zhang D., Luo X., Xu G., Han J., (2014), “Windage heating in a shrouded rotor-stator system”, Journal of Engineering for Gas Turbines and Power, 136(6).

[56] Bayley F. J., Owen J. M., (1970), “The fluid dynamics of a shrouded disk system with a radial outflow of coolant”, Journal of Engineering for Gas Turbines and Power, 92(3), 335–341.

[57] Martin Gaskell, “Supermassive black holes: most powerful objects in the universe”, *YouTube*, Feb. 16, 2018, [video]. Available: https://www.youtube.com/watch?v=Zo4gRhG90S4, [Accessed: Jan. 28,2022].

[58] NASA Science, “NASA’s Hubble gets the best image of bright quasar 3C 273”, Nov. 21, 2013, [online]. Available: https://science.nasa.gov/missions/hubble/nasas-hubble-gets-the-best-image-of-bright-quasar-3c-273, [Accessed: Jan. 28,2022].

[59] Calar Alto Observatory, “The most luminous quasar state ever observed”, July 2006, [online]. Available:

https://web.archive.org/web/20150407050257/http://www.caha.es/the-most-luminous-quasar-state-ever-observed.html, [Accessed: Dec. 13,2023].

[60] Wang F., Yang J., Fan X., Hennawi J. F., Barth A. J., Banados E., Yue M., (2021), “A Luminous Quasar at Redshift 7.642”, The Astrophysical Journal Letters, 907(1), L1.

[61] NSF’s NOIRLab (National Optical-Infrared Astronomy Research Laboratory, “Artist’s impression of quasar J0313-1806”, Jan. 12, 2021, [online]. Available: https://noirlab.edu/public/images/noirlab2102a/, [Accessed: Nov. 20,2023].

BIOGRAPHY

The author, Onur GARIP, graduated from Middle East Technical University (METU), Department of Aerospace Engineering in 2018. He has started his career in the gas turbine industry as a Thermal System Design Engineer and is still working in this field.